Uniwersytet Mikołaja Kopernika
Szkoła Doktorska Nauk Ścisłych i Przyrodniczych
Instytut Astronomii

Michał Tomasz Durjasz
nr albumu: 503132

Praca doktorska
astronomia

Poszukiwanie masywnych protogwiazd o zmiennej akrecji identyfikowanej przez wybuchy maserów metanolu

Opiekun pracy doktorskiej
prof. dr hab. Marian Szymczak
Instytut Astronomii

Opiekun pracy doktorskiej
dr hab. Anna Bartkiewicz, prof. UMK
Instytut Astronomii

Toruń 2023

Pracę przyjmuję i akceptuję

.....
data i podpis opiekuna pracy

Pracę przyjmuję i akceptuję

.....
data i podpis opiekuna pracy

Szczególne podziękowania należą się:

- *Mojej żonie Oliwii - za najlepszy ramen w tej części Bieszczad*
- *Dawidowi - za najlepsze partie w Supreme Commandera*
- *Annie Bartkiewicz - za rewelacyjne uwagi dot. interferometrii*
- *Marianowi Szymczakowi - za doskonałe prowadzenie mnie przez wszystkie etapy kariery naukowej, aż do teraz*
- *Mateuszowi Olechowi - za wartościową współpracę*

Uniwersytet Mikołaja Kopernika zastrzega sobie prawo do licencji niewyłącznej niniejszej pracy doktorskiej w celu udostępniania dla potrzeb działalności naukowo-badawczej lub dydaktyczne

Spis treści

Spis rysunków 4

Streszczenie 5

Abstract 6

1 Wstęp **7**

1.1 Tło naukowe 7

1.1.1 Formowanie się masywnych gwiazd 7

1.1.2 Emisja maserowa 10

1.1.3 Molekuła CH_3OH 13

1.2 Projekt naukowy 15

1.2.1 Cele 15

1.2.2 Metody 15

1.2.3 Obserwacje spektralne maserów metanolu 16

1.2.4 Obserwacje w ramach europejskiej sieci interferometrii wielkobazowej (EVN) 18

2 Omówienie wyników pracy **20**

2.1 Przegląd nieba północnego w linii 12.2 GHz masera CH_3OH 20

2.2 Odkrycie powtarzających się flar 6.7 GHz masera metanolu w Cep A HW2 . 23

2.2.1 Oddziaływanie promieniste między obłokami maserującymi (Cesaroni, 1990) 26

2.3 Odkrycie periodycznych pojaśnień 6.7 GHz masera metanolu w źródłach G45.804−0.356 i G49.043−1.079 28

3 Podsumowanie **30**

Spis rysunków

1.1 S255 - pojaśnienie 11
1.2 Schemat emisji maserowej 11
1.3 Przykładowy rozkład emisji 13
1.4 Schemat molekuły CH_3OH 14
1.5 Poziomy energetyczne metanolu 14

2.1 Periodyczna zmienność G107.298+5.639 21
2.2 Nowo odkryte źródła 12.2 GHz 22
2.3 Procentowa zmiana strumienia zintegrowanego 6.7 vs 12.2 GHz 22
2.4 Rozkład przestrzenny emisji maserowej 6.7 GHz w Cep A HW2 + ruchy własne 25
2.5 Wizualizacja modelu Cesaroni (1990). 27
2.6 Krzywe blasku antyskorelowanych cech widmowych 27
2.7 Widmo dynamiczne G45.804−0.356 29
2.8 Widmo dynamiczne G49.043−1.079 29

Streszczenie

Wyjaśnienie mechanizmu powstawania masywnych gwiazd jest jednym z podstawowych zagadnień współczesnej astrofizyki. Ostatnie obserwacyjne i teoretyczne prace na tym polu sugerują, że podobnie jak protogwiazdy małomasywne, masywne, młode gwiazdy gromadzą większość materii w krótkich okresach wzmożonej aktywności (w ramach *epizodycznej akrecji*). Badania markerów aktywności młodych, masywnych gwiazd, w szczególności linii 6.7 i 12.2 GHz masera metanolu (CH_3OH) dostarczają nowych danych, pomagających testować tę teorię i odkrywać nowe przypadki pojaśnień.

Praca ta podsumowuje wykonane przeze mnie badania zmienności młodych obiektów gwiazdowych z wykorzystaniem emisji maserowej metanolu w liniach 6.7 i 12.2 GHz. Szczególnie dużo uwagi poświęciłem poszukiwaniu i bliższemu badaniu przypadków pojaśnień. W tym celu wykorzystałem trwające ponad dekadę (od 2009 r.) obserwacje maserów CH_3OH w linii 6.7 GHz, wykonane z użyciem 32 m radioteleskopu Instytutu Astronomii UMK oraz wykonałem nim przegląd nieba północnego w linii 12.2 GHz. Uzyskałem też czas obserwacyjny w Europejskiej Sieci Interferometrii Wielkobazowej (EVN).

Wynikiem mojej pracy jest odkrycie czterech nowych źródeł, charakteryzujących się emisją w linii 12.2 GHz, z czego jedno: G107.298+5.639, znane z periodyczności w liniach metanolu 6.7 GHz oraz wody (H_2O) 22 GHz okazało się periodyczne również w linii metanolu 12.2 GHz. Odkryłem periodyczne z okresem 5 lat pojaśnienia cech widmowych -0.5 i $-1.3\,\mathrm{km\,s^{-1}}$ w linii 6.7 GHz masera metanolu w Cefeuszu A (Cep A) w składniku HW2. Są one najprawdopodobniej wywołane oddziaływaniem masywnej protogwiazdy z mniej masywnym towarzyszem oraz dwa nowe źródła periodyczne w linii 6.7 GHz o długim (>400 dni) okresie: G45.804−0.356 i G49.043−1.079. Dokonane odkrycia sugerują, że poziom aktywności młodych, masywnych gwiazd ulega silnej fluktuacji nawet w krótkich skalach czasowych (<1 rok), nierzadko mają one charakter periodyczny lub quasi–periodyczny, a przyczyną są przede wszystkim interakcje z gwiazdowymi towarzyszami w układach wielokrotnych.

Abstract

The explanation of how massive stars form is one of the fundamental problems of modern astrophysics. Recent observational and theoretical works in this field suggest that massive young stars, similary to low-mass protostars, accumulate most of their material during short bursts of activity (*episodic accretion*). The study of activity markers for young, massive stars, in particular the 6.7 and 12.2 GHz lines of the methanol (CH_3OH) maser, provides new data to test this theory and discover new outbursts.

This work summarizes my research of the young massive stellar objects using methanol maser emission in 6.7 and 12.2 GHz transitions. I paid particular attention to searching and examining cases of brightening of the maser emission. I utilized observations of the 6.7 GHz transition, performed for over a decade (since 2009) by the 32-m radio telescope of the Institute of Astronomy NCU and I also made the survey of the northern sky in 12.2 GHz line with it. I obtained the observational time at the European VLBI Network (EVN).

My research resulted in discovering of four new sources with 12.2 GHz CH_3OH maser emission of which one: G107.298+5.639, known for its periodicity at the methanol 6.7 and water (H_2O) 22 GHz transitions turned out to by periodic also in the 12.2 GHz methanol line. I discovered periodic, with a period of 5 years, flares of the -0.5 and $-1.3\,\mathrm{km\,s^{-1}}$ spectral features of the 6.7 GHz methanol maser line in Cepheus A (Cep A) component HW2. They are most likely caused by the interactions of the central protostar with its low-mass companion. I also discovered two new periodic sources at the 6.7 GHz transition with long (>400 days) periods: G45.804−0.356 and G49.043−1.079. These findings suggest that the activity level of young, massive stars fluctuates strongly even in short time scales (<1 year), they are often periodic or quasi-periodic, and the reason is primarily interactions with stellar companions in multiple systems.

Rozdział 1

Wstęp

1.1 Tło naukowe

Masywne gwiazdy ($> 8\,M_\odot$) wpływają w znacznym stopniu na kinematykę i skład chemiczny materii międzygwiazdowej – to one właśnie, jako supernowe wprowadzają do ośrodka międzygwiazdowego fale uderzeniowe oraz materię z cięższymi pierwiastkami. Badanie powstawania masywnych gwiazd jest jednym z podstawowych zagadnień współczesnej astrofizyki (np. Zinnecker & Yorke 2007). Jednak nadal mechanizm ich powstawania jest obiektem dyskusji społeczności naukowej, ponieważ nie istnieje jeden powszechnie akceptowany scenariusz.

1.1.1 Formowanie się masywnych gwiazd

Wielkie obłoki molekularne (*Giant Molecular Clouds*, GMC) są miejscem powstawania gwiazd. Składają się głównie z wodoru molekularnego o typowej temperaturze ok. 10 K i osiągają masy przekraczające $10^6\,M_\odot$. Jeśli obłok przekroczy tzw. masę Jeansa, jego wewnętrzne ciśnienie nie będzie w stanie przeciwdziałać kolapsowi grawitacyjnemu i zacznie się zapadać. W trakcie kolapsu, energia grawitacyjna jest uwalniana głównie jako promieniowanie podczerwone, jednak w miarę wzrostu gęstości obłoku rośnie też jego nieprzezroczystość – co skutecznie przeciwdziała emitowaniu energii kolapsu, efektem czego jest wzrost temperatury. W trakcie zapadania się obłok ulega fragmentacji na wiele ośrodków o podwyższonej gęstości, w których centrach powstają gwiazdy - po osiągnięciu odpowiednich warunków, w ich centrach rozpoczynają się reakcje przemiany wodoru w hel, co zatrzymuje dalsze gromadzenie materii, a nowo powstała gwiazda osiąga ciąg główny. Naturalnym sposobem na oddzielenie populacji gwiazd masywnych od pozostałych jest

właśnie moment wejścia na ciąg główny - w przypadku gwiazd masywnych, przemiana wodoru rozpoczyna się jeszcze w momencie, w którym jest ona otoczona nieprzezroczystą materią obłoku, z którego powstała.

Teoretyczne modele powstawania gwiazd i koncepcja epizodycznej akrecji

Pierwsze modele jednowymiarowe, opisywane jako sferycznie symetryczna akrecja pozwalały na uzyskanie gwiazdy o masie maksymalnie ok. $8\,M_\odot$. Po osiągnięciu tej wartości, ciśnienie promieniowania gwiazdy stawało się zbyt duże i powstrzymywało dalsze ściąganie materii (Kahn, 1974). Obserwacje reprezentatywnej próbki 23 powstających, małomasywnych gwiazd (Kenyon et al., 1990, 1994) ukazały znacznie ciemniejsze obiekty, niż wynikało z modeli – była to ich negatywna weryfikacja. Niezgodność teoretycznej i modelowanej jasności protogwiazd zaczęto opisywać jako *luminosity problem*. W Kenyon & Hartmann (1995) zaproponowano rozwiązanie: epizodyczną akrecję. Wg tej teorii powstające gwiazdy znaczną część materii gromadzą w okresach krótkotrwałych wzrostów tempa akrecji – z uwagi na to, większość protogwiazd jest obserwowana w trakcie „cichego" okresu, w którym tempo akrecji jest niewielkie. Teoria ta została oparta na obserwacjach – znaczne pojaśnienia gwiazd typu FU Ori obserwowane były już od lat 30 XX wieku. Implementacja epizodycznej akrecji w modelach powstawania gwiazd (Offner & McKee, 2011) pokazała, że jest to możliwe rozwiązanie *luminosity problem*.

Modele 2D wskazały na istnienie struktur, towarzyszących powstającym gwiazdom: dysku akrecyjnego i wypływów. Obecność dysku okazała się kluczowa w procesach gwiazdotwórczych: ciśnienie promieniowania znacznie spada w jego płaszczyźnie, co pozwala materii na przedostanie się w pobliże samej gwiazdy. Tego typu podejście pozwalało uzyskać gwiazdy o masie do $20\,M_\odot$ (Nakano et al., 1995; Jijina & Adams, 1996).

Pierwsze symulacje 3D (Krumholz et al., 2009) pozwoliły uzyskać system o łącznej masie gwiazdowej, przekraczającej $70\,M_\odot$ – uzyskane tempo akrecji zmieniało się jednak w zakresie dużo mniejszym, niż w przypadku małomasywnych gwiazd - dodatkowo brak dowodów obserwacyjnych na epizodyczną akrecję sugerował, że te powstają w odmienny sposób od swoich mniej masywnych odpowiedników. Dopiero w ostatniej dekadzie udało się uzyskać efekt epizodycznej akrecji w modelach teoretycznych (Meyer et al., 2017, 2019, 2022) oraz potwierdzić go obserwacyjnie (np. Moscadelli et al. 2017).

Obserwacje skoków tempa akrecji w przypadku masywnych protogwiazd

Z powodu znacznej odległości i wysokiej ekstynkcji międzygwiazdowej w widzialnym zakresie widma elektromagnetycznego, nie udało się zaobserwować żadnego gwałtownego wzrostu tempa akrecji wokół powstających, masywnych gwiazd aż do roku 2015 – wtedy to zaobserwowane zostało gwałtowne pojaśnienie w źródle S255−NIRS3 ($M_{star} = \sim 20\,M_\odot$) (Fujisawa et al., 2015). Wydarzenie to wzbudziło ogromne zainteresowanie środowiska naukowego, efektem czego było dużo projektów obserwacyjnych w różnych zakresach widma elektromagnetycznego (sub-mm, IR, radio: Caratti o Garatti et al. 2017; Moscadelli et al. 2017; Szymczak et al. 2018a). Obserwacje linii widmowych, charakterystycznych dla gwiazd FU Ori potwierdziły hipotezę o wzroście tempa akrecji, a z analizy SED (spectral energy distribution) oszacowano, że w czasie 9 miesięcy centralny obiekt zgromadził materię o masie kilku mas Jowisza ($\sim 3.4 \times 10^{-3}\,M_\odot$). Emisja 6.7 GHz maserów metanolu w okresie pojaśnienia wzrosła o ponad dwa rzędy wielkości, dodatkowo po flarze profil widmowy przejścia 6.7 GHz był inny niż przed (Rys. 1.1).

W połowie 2015 roku zaobserwowano 4-krotny wzrost emisji continuum w paśmie sub-mm (1.3 mm) w źródle NGC6334I−MM1 oraz 10-krotny wzrost jasności emisji maserowej w linii CH_3OH (6.7 GHz) oraz H_2O (22 GHz) (Hunter et al., 2017). Obserwacyjne cechy zdarzenia były bardzo podobne do przypadku S255−NIRS3: krzywa blasku, charakteryzująca się szybkim wzrostem i powolnym spadkiem oraz podobna co do rzędu wielkości łączna ilość wyświeconej energii (0.8×10^{39} J).

Obserwacje zjawisk w S255−NIRS3 i NGC6334I−MM1 wskazały na konieczność ustanowienia międzynarodowej współpracy w celu monitorowania możliwie dużej próbki źródeł. Z tego powodu powstał zespół monitorujący Maser Monitoring Organization (M2O[1]) oparty na dobrowolnej współpracy między ośrodkami dysponującymi średniej wielkości radioteleskopami. Obecnie duża część źródeł, znanych z emisji w linii 6.7 GHz masera metanolu jest regularnie obserwowana głównie przez anteny w Toruniu, Hitachi (Japonia) i Hartebeesthoek (RPA).

W 2019 roku zaobserwowano gwałtowny wzrost jasności maserów metanolu wokół masywnej protogwiazdy ($10\,M_\odot$) G358−MM1 (Burns et al., 2020). Obserwacje w zakresie podczerwonym na długości fali $160\,\mu$m wykazały 3-krotne pojaśnienie, potwierdzając kolejne zdarzenie gwałtownego wzrostu tempa akrecji. Zjawisko różniło się jednak od dwóch

[1] https://www.masermonitoring.com/

poprzednich wydarzeń poprzez brak pojaśnienia kontinuum w paśmie milimetrowym oraz w dalszej podczerwieni, samo pojaśnienie trwało też krócej (<1 rok) od wcześniej zaobserwowanych. Szeroko zakrojona kampania obserwacyjna pozwoliła odkryć osiem nowych przejść masera metanolu (Miao et al., 2022) oraz zmapować emisję w linii 6.7 GHz w trakcie wybuchu za pomocą obserwacji VLBI o dużej rozdzielczości. Emisja 6.7 GHz okazała pojawiać się w coraz dalszych odległościach od centrum układu, co zaowocowało rozwinięciem teorii fali cieplnej (ang. *heatwave*) - jest to ciąg absorpcji i reemisji, przemierzający płaszczyznę dysku z prędkościami ok. 4 % prędkości światła i pobudzający do emisji maserowej molekuły metanolu. Dokładniejsza analiza danych o dużej rozdzielczości pozwoliła na dopasowanie czterech ramion spiralnych, co sugeruje, że dysk wokół G358−MM1 jest niestabilny grawitacyjnie (Burns et al., 2023). Odkrycie to jest o tyle ważne, że fragmentacja niestabilnych grawitacyjnie dysków jest postulowana jako główny mechanizm, prowadzący do gwałtownych wzrostów tempa akrecji (Meyer et al., 2017) – odkrycie ramion spiralnych jest zatem dowodem na słuszność modeli.

Powyższe przypadki różnią się między sobą przebiegiem oraz charakterystykami czasowymi, co sugeruje różnorodność zdarzeń epizodycznej akrecji oraz ich wpływu na otoczenie protogwiazdy. Poszukiwanie nowych przypadków tego typu pojaśnień może dostarczyć nowe dane, pogłębiając nasze poznanie przyczyn ich powstawania, pozwoli również na weryfikację tezy, że proces powstawania masywnych gwiazd jest podobny do procesu powstawania gwiazd o mniejszej masie. W tym celu często jako marker tego typu zjawisk wykorzystuje się emisję maserową molekuł metanolu, w szczególności linię 6.7 GHz – emisja maserowa w tej linii powstaje w bezpośrednim otoczeniu gwiazdy i jest wrażliwa na warunki fizyczne (Sobolev et al., 1997; Cragg et al., 2005).

1.1.2 Emisja maserowa

Maser - *Microwave Amplification by Stimulated Emission of Radiation* - nietermiczna emisja w mikrofalowym zakresie widma elektromagnetycznego, będąca analogią prostego, jednoprzejściowego lasera. Ten typ emisji jest obserwowany w dużej obfitości w materii międzygwiazdowej, przede wszystkim w otoczeniu materii molekularnej. Obiekty, w sąsiedztwie których udało się zaobserwować emisję maserową to m.in.: komety, gwiazdy post-AGB (tzw. "fontanny wodne"), gwiazdy typu Mira-Ceti czy młode obiekty gwiazdowe (Young Stellar Objects - YSO) (Elitzur, 1992). Charakteryzuje się wysokimi tem-

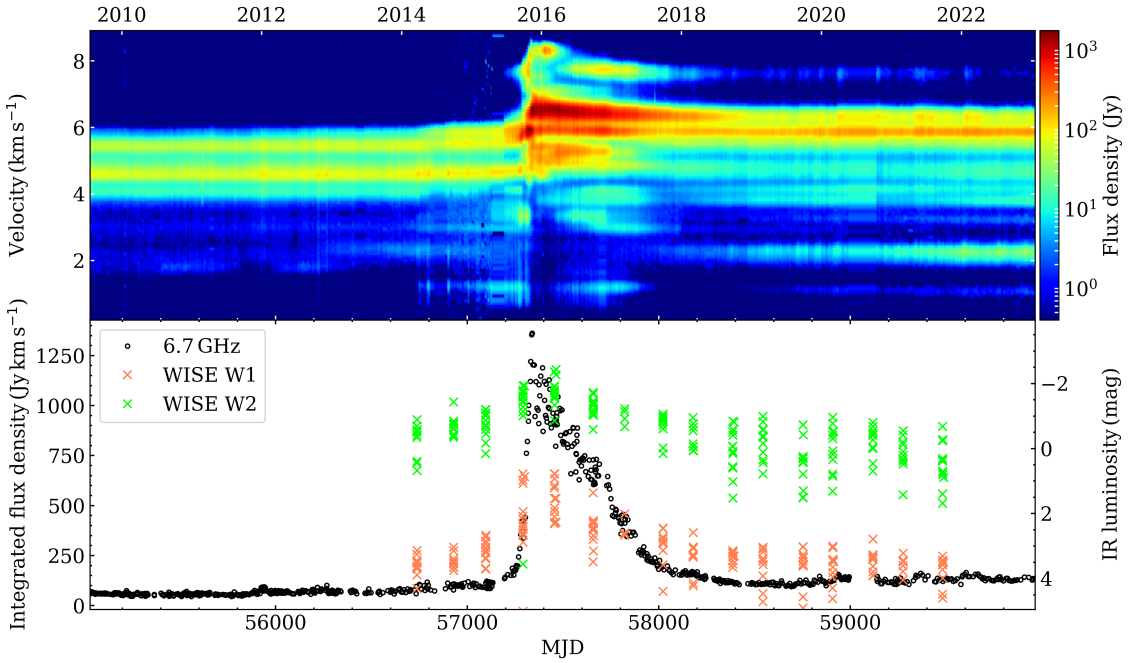

Rys. 1.1: *Górny panel*: widmo dynamiczne 6.7 GHz maserów metanolu w S255−NIRS3, *dolny panel*: krzywa blasku strumienia zintegrowanego z nałożonymi danymi IR z satelity WISE (pasma W1 i W2, odpowiednio 3.4 i 4.6 μm).

peraturami jasnościowymi ($>10^{10}$ K), wąskimi (w porównaniu do termicznych) profilami linii widmowych, wysoką zmiennością i kierunkowością emisji. Schemat prostego, trójpoziomowego modelu emisji przedstawiony jest na Rys. 1.2.

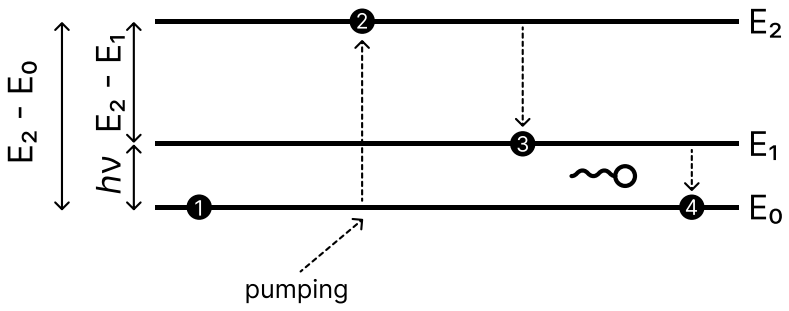

Rys. 1.2: Schematyczna wizualizacja mechanizmu emisji maserowej.

Poszczególne etapy na Rys. 1.2 przedstawiają:

1. Molekułę w stanie podstawowym E_0.
2. Pompowanie molekuły do poziomu niestabilnego E_2.
3. Spontaniczny spadek do metastabilnego poziomu E_1.
4. Przejście wymuszone z poziomu E_1 do E_0 w wyniku interakcji molekuły z fotonem o energii równej energii przejścia.

Silny, obserwowalny z astrofizycznych odległości maser powstaje, gdy zachodzi zjawisko zwane *wzmocnieniem maserowym* - generowane przez mechanizm emisji wymuszonej fotony wymuszają emisję kolejnych, co powoduje wzrost eksponencjalne zależny od drogi wzmocnienia. Wystąpienie takiej emisji jest uzależnione od występowania konkretnych warunków:

- *Seed photons* - pierwotne fotony, wymuszające emisję. Mogą to być fotony promieniowania tła lub z emisji spontanicznej molekuł wewnątrz obłoku.
- Inwersja obsadzeń - nadwyżka obsadzenia poziomów E_2 oraz E_1 względem obsadzenia opisanego rozkładem Boltzmanna. Następuje ona w wyniku występowania czynnika pompującego - promieniowania EM lub fal uderzeniowych.
- Odpowiednia gęstość - zbyt mała sprawi, że szansa by wymuszony foton napotkał molekułę w stanie metastabilnym będzie bardzo mała, zbyt duża spowoduje, że inwersja obsadzeń zostanie wygaszona zderzeniowo.
- Koherencja prędkości wzdłuż drogi wzmocnienia - przy zbyt dużym rozrzucie prędkości wzdłuż drogi wzmocnienia, foton w układzie spoczynkowym napotkanych molekuł często będzie miał energię zbyt różniącą się od energii przejścia $E_1 - E_0$ by wymusić emisję kolejnego fotonu.

Obszary, w których powyższe warunki są spełnione nazywa się *obłokami maserującymi*.

Zależność temperatury jasnościowej od drogi wzmocnienia w niesaturowanym obłoku maserującym jest dane równaniem 1.1 (Reid & Moran, 1981).

$$T_B(l) = [T_B(0) - T_x]e^{-\kappa l} + T_x \tag{1.1}$$

W warunkach inwersji obsadzeń, opisujący absorpcję czynnik κ jest ujemny, przez co $e^{-\kappa l}$ efektywnie działa jako czynnik wzmacniający - temperatura jasnościowa jest zależna eksponencjalne od drogi wzmocnienia l. T_x to temperatura wzbudzenia zdefiniowana wzorem 1.2.

$$e^{-h\nu/kT_x} = \frac{n_1}{n_0}, \tag{1.2}$$

Współczynniki n_1 i n_0 opisują poziomy koncentracji molekuł CH_3OH w stanie odpowiednio E_1 i E_0. W warunkach inwersji obsadzeń ($n_1 > n_0$), T_x przyjmuje wartości ujemne.

Przykładowy rozkład przestrzenny obłoków maserujących wokół masywnej protogwiazdy (Cep A HW2, $\sim$10 $M_\odot$) jest przedstawiony na Rys. 1.3.

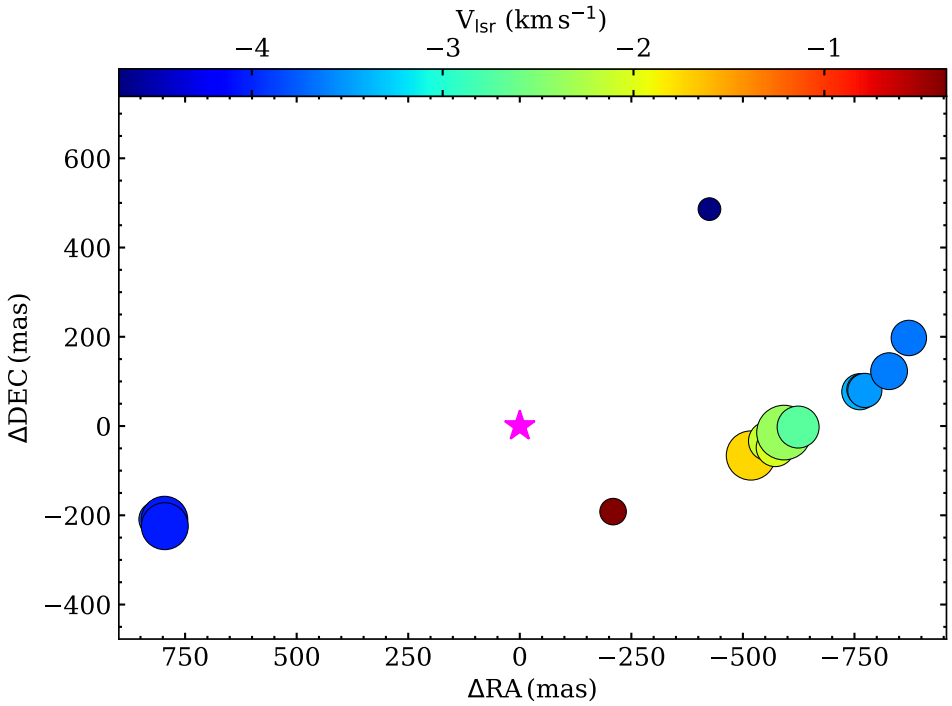

Rys. 1.3: Przykładowy rozkład przestrzenny emisji maserowej molekuły CH_3OH w linii 6.7 GHz wokół źródła Cep A HW2, zaobserwowany przez sieć EVN w ramach projektu o kodzie ED048B (Durjasz et al., 2022). Różowa gwiazda wskazuje pozycję źródła continuum (Curiel et al., 2006).

1.1.3 Molekuła CH_3OH

Molekuła metanolu (Rys. 1.4) dzięki dużej liczbie przejść w zakresie mikrofalowym i milimetrowym jest bardzo użytecznym narzędziem badań materii międzygwiazdowej. Wynika to ze skomplikowanej budowy cząstki CH_3OH. Dodatkowo liczbę dostępnych przejść

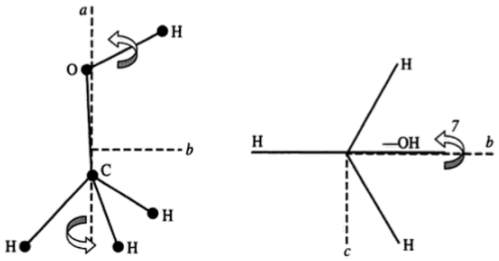

Rys. 1.4: Schemat molekuły metanolu z zaznaczeniem ruchu torsyjnego grupy metylowej (lewa strona) oraz w rzucie z pokazanym kątem torsyjnym 7 (prawa strona) wg. Xu (2001).

zwiększa występowanie dwóch typów molekuły: ustawienia spinów jąder atomów wodoru w grupie metylowej (CH_3) determinują symetrie typu A (-ortho) i E (-para) o spinie całkowitym odpowiednio 3/2 i 1/2. Występują zatem dwa różne typy widm rotacyjno-wibracyjnych, między którymi przejścia nie są możliwe. Sama cząsteczka nie jest sztywnym rotorem - grupa CH_3 rotuje w sposób krępowany (*hindered rotation*), zwany też rotacją wewnętrzną lub ruchami torsyjnymi w układzie odniesienia związanym z C-OH. Do opisu poziomów energetycznych potrzebne są dwie liczby kwantowe: **J** - całkowity moment pędu oraz **K** - rzut momentu pędu na oś rotacji grupy CH_3 (przyjmuje wartości od -**J** do **J**). W przypadku molekuły o symetrii A poziomy energetyczne przyjmują postać dubletów $\pm\mathbf{K}$, które nieznacznie różnią się energiami (oznacza się je jako $A^{\pm}$). W cząsteczce E różnice między energiami $\pm\mathbf{K}$ są duże (Gray 2012).

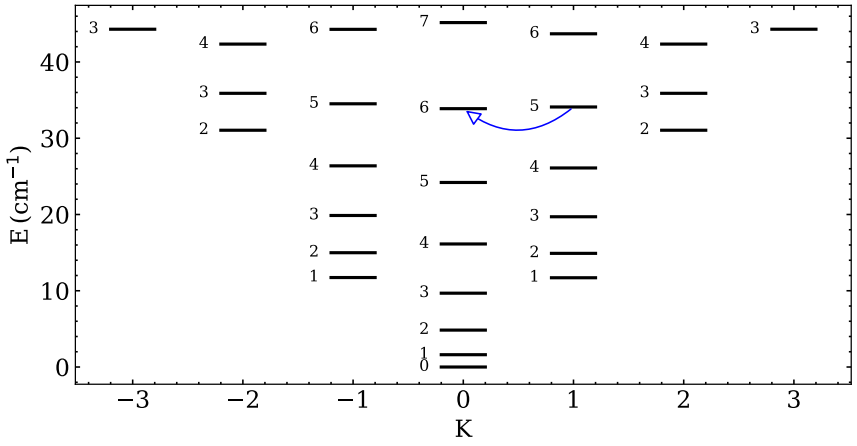

Rys. 1.5: Poziomy energetyczne molekuły CH_3OH (w wersji A) w podstawowym stanie wibracyjnym. Wartości, wstawione obok belek, symbolizujących poziomy opisują odpowiadającą im wartość **J**. Przejście 5_1 - 6_0 A^+ (6.7 GHz) zostało zaznaczone niebieską strzałką. Wykres sporządzono na podstawie Leiden Atomic and Molecular Database (https://home.strw.leidenuniv.nl/~moldata/).

1.2 Projekt naukowy

1.2.1 Cele

Głównymi celami mojego projektu doktorskiego były:

1. Monitorowanie emisji maserowej metanolu dużej próbki masywnych gwiazd, aby zidentyfikować nadzwyczajne wybuchy.

2. Zbadanie, czy obserwowane w projektach monitoringu pojaśnienia promieniowania maserowego są sygnaturami przejściowego wzrostu tempa akrecji.

3. Szczegółowsze badanie wybranych obiektów technikami interferometrycznymi. Zebranie nowych danych, które pozwoliłyby lepiej opisać charakterystyki zdarzeń akrecyjnych, dając podstawy do weryfikacji ich modeli teoretycznych, a przez to poprawę modeli powstawania masywnych gwiazd oraz emisji maserowej.

1.2.2 Metody

W ramach projektu (w latach 2019-2023) kontynuowałem prowadzony od 2009 roku monitoring emisji maserowej metanolu w linii 6.7 GHz za pomocą 32 m radioteleskopu. W przypadku wykrycia pojaśnienia w jednym ze źródeł aplikowałem na czas obserwacyjny w ramach Europejskiej Sieci Interferometrii wielkobazowej (EVN[2]) by uzyskać dane w wysokiej rozdzielczości. Biorąc pod uwagę rzadkość takich zjawisk, przygotowałem również dwa projekty, mające badać zmienność długoterminową na możliwie największej próbce źródeł:

- Przegląd nieba północnego w linii 12.2 GHz masera CH_3OH.

- Przegląd nieba północnego w linii 6.7 GHz masera CH_3OH, będący kontynuacją i rozszerzeniem przeglądu opublikowanego wcześniej w Szymczak et al. (2012).

Pozwoliło to na uniknięcie ryzyka braku detekcji pojaśnień w okresie od października 2019 do września 2023 (w okresie trwania projektu doktorskiego).

[2]European VLBI Network, https://www.evlbi.org/

1.2.3 Obserwacje spektralne maserów metanolu

Obserwacje spektralne maserów metanolu zostały wykonane z wykorzystaniem 32 m radioteleskopu Instytutu Astronomii UMK znajdującego się w Piwnicach koło Torunia (Kus & Borkowski, 2011).

Linia 6.7 GHz

Obserwacje spektralne przejścia 6.7 GHz prowadzone były z wykorzystaniem odbiornika na pasmo C, noszącego oznaczenie C2. Całkowita temperatura szumowa systemu T_{sys} mieściła się w zakresie od 25 do 40 K. Szerokość połówkowa wiązki radioteleskopu na częstotliwości 6.7 GHz wynosiła 5.8' a niepewność pozycjonowania anteny 25′ do 2016, 10′ po 2016 (Lew, 2018). By skompensować wpływ tła oraz charakterystyki odbiornika, wykorzystaliśmy technikę przełączania częstotliwości na wstędze o szerokości 4 MHz - taka konfiguracja przy wykorzystaniu spektrometru autokorelacyjnego z 4 pasmami po 4096 kanałów oraz wygładzania Hanninga pozwalała na uzyskanie widm o rozdzielczości 0.09 km s^{-1}. Typowy poziom szumów 1σ przy czasie integracji 10 minut wynosił $\sim$0.3 Jy.

Linia 12.2 GHz

Odbiornik na pasmo X charakteryzuje się typową temperaturą szumową na poziomie 5 K, przy całkowitej temperaturze szumowej systemu (T_{sys}) równej 30 K przy idealnej pogodzie. Na podstawie obserwacji kalibratorów DR21 oraz 3C123 (Ott et al., 1994), oszacowaliśmy efektywność anteny na ok. 0.06 K Jy^{-1}. Podstawowe parametry wykonanych obserwacji zaprezentowane są w tabeli 1.1.

Tablica 1.1: Parametry obserwacji spektralnych w linii 12.2 GHz.

Parametr	przed 12.2019	po 12.2019
Rozdzielczość widma ($\mathrm{km\,s^{-1}}$)	0.048	0.024
Szerokość pasma (MHz)	4	2
Poziom szumów 3σ (Jy)	1.5	
Szerokość wiązki na 12.2 GHz ($'$)	3	
Całkowita niepewność kalibracji strumienia (%)	15	
Metoda obserwacyjna	Przełączanie częstotliwości	
Długość jednego skanu (min)	0.5	
Długość integracji (min)	60	

Rewizja procesu redukcji danych

Praca nad danymi spektralnymi skupiała się na trzech kluczowych aspektach:

- akwizycja danych
- redukcja danych
- archiwizacja danych

W przypadku redukcji i archiwizacji konieczne były znaczne zmiany dotąd używanego fortranowskiego oprogramowania. Dotychczasowy sposób przechowywania danych (pliki tekstowe) nie gwarantował wysokiej wydajności oraz był podatny na błędy odczytu. Ponadto w procesie redukcji danych do obliczania ruchu Ziemi w kierunku źródła stosowano metodę, opisaną w Stumpff (1980), której dokładność po roku 2020 jest wątpliwa. Koniecznością zatem stała się rewizja zestawu oprogramowania do redukcji, analizy oraz archiwizacji danych. W tym celu stworzyłem pakiet złożony z:

- SimpleSingleDishDataReductor (SSDDR) - program do redukcji danych spektralnych z radioteleskopu RT4. Między innymi rotuje on widmo, kompensując ruch Ziemi (wykorzystuje w tym celu pakiet BARYCORRPY). Napisany w języku Python. Interfejs graficzny został oparty o framework Qt (PyQt5). Wynikowe widma zapisuje do plików .fits. Kod źródłowy dostępny jest w serwisie github: https://github.com/dachshund-ncu/simpleSingleDishDataReductor.

- RT4SV++ - następca programu do wizualizacji danych, napisany w C++. Pozwala na odczytywanie starych plików tekstowych z widmami oraz plików .fits, pochodzących z SSDDR. Podobnie jak SSDDR, jego interfejs graficzny został oparty o framework QT. Kod źródłowy dostępny jest w serwisie github: https://github.com/dachshund-ncu/rt4svpp.

- maser-achive-dashboard - dostępny w sieci wewnętrznej Obserwatorium serwis, pozwalający na pobieranie i wizualizację widm metanolu w linii 6.7 GHz. Oparty o framework STREAMLIT, kod źródłowy dostępny jest w serwisie github: https://github.com/dachshund-ncu/maser-archive-dashboard.

Podmiana wcześniejszych danych z plików tekstowych na .fits pozwoliła zmniejszyć rozmiar archiwum ok. 4-krotnie (z 5 GB do 1.3 GB) oraz umożliwiła sprawne wczytywanie dużych partii danych.

1.2.4 Obserwacje w ramach europejskiej sieci interferometrii wielkobazowej (EVN)

Wnioski o czas obserwacyjny wysyłałem po odkryciu pojaśnienia za pomocą monitoringu radioteleskopem RT4. Typowo we wniosku uwzględniane były 3 źródła:

- Fringe-finder - jasne, zwarte źródło, gwarantujące dobry stosunek sygnału do szumu na wszystkich bazach w czasie kalibracji.

- Kalibrator fazy - zwarte źródło o dobrze wyznaczonej pozycji, znajdujące się w podobnym kierunku co źródło programowe – cel obserwacji (w promieniu $\sim 3^{o}$ od niego). Kalibrator wybierany jest zazwyczaj z listy kalibratorów VLBA: http://www.vlba.nrao.edu/astro/calib/vlbacalib_allfreq_full2023a.txt.

- Docelowe źródło - cel obserwacji.

Wszystkie projekty wykorzystywały technikę phase-referencingu: źródło programowe obserwowane było naprzemiennie z kalibratorem fazy w 5-minutowych cyklach (odpowiednio 3 m 15 s oraz 1 m 45 s). Takie podejście do obserwacji umożliwia ciągłą kalibrację, uwzględniającą zmienne warunki atmosferyczne na kalibratorze fazy i transfer tych rozwiązań do celu naukowego. Zebrane dane były procesowane za pomocą korelatora w instytucie JIVE

(Keimpema et al., 2015). We wnioskach zawierałem prośbę o dwukrotną procedurę korelacji: pierwszą na szerokim paśmie z minimalną ilością kanałów, drugą na węższym paśmie i z odpowiednią ilością kanałów do badania linii widmowych o szerokości połówkowej poniżej $1\,\mathrm{km\,s^{-1}}$. Szerokopasmowy zestaw danych pozwalał na zwiększenie stosunku sygnału do szumu podczas obserwacji kalibratora fazy i uzyskanie lepszej kalibracji (Sanna et al., 2015). Redukcję danych wykonywałem w ogólnodostępnym pakiecie AIPS[3] (Astronomical Image Processing System). Poprawki do fazy, policzone na szerokopasmowym zestawie danych za pomocą tasku FRING przenosiłem na docelowy, wąskopasmowy zestaw danych. Tak skalibrowane dane pozwalały na wyprodukowanie map jasności (parametr Stokesa I) za pomocą procedury IMAGR. Jasność emisji maserowej była szacowana za pomocą dopasowania dwuwymiarowej funkcji Gaussa (procedura JMFIT).

[3] http://www.aips.nrao.edu/index.shtml

Rozdział 2

Omówienie wyników pracy

2.1 Przegląd nieba północnego w linii 12.2 GHz masera CH_3OH

W publikacji *Observations of 12.2 GHz methanol masers towards northern high-mass protostellar objects* przedstawiliśmy rezultaty przeglądu źródeł nieba północnego, znanych z emisji 6.7 GHz, w linii 12.2 GHz. Tego typu przeglądy były już realizowane wielokrotnie (Norris et al., 1987; Kemball et al., 1988; Koo et al., 1988; Caswell et al., 1993, 1995; Błaszkiewicz & Kus, 2004; Breen et al., 2010, 2012, 2016), żaden jednak nie objął w całości północnej półkuli - nasza praca zapełniała tę lukę w danych.

Obserwacje były wykonywane w okresie od lipca 2019 do lutego 2020 z wykorzystaniem odbiornika na pasmo X, zbudowanego w laboratorium Instytutu Astronomii UMK (Pazderski, 2018). Parametry obserwacji zostały zaprezentowane w sekcji 1.2.3.

Od początku wykonywania obserwacji napotkaliśmy poważne problemy w obserwacjach źródeł o deklinacji $\delta < 10\,^\circ$. Wynikało to z obecności satelitów geostacjonarnych, nadających na paśmie Ku – saturowały one odbiornik, uniemożliwiając obserwacje emisji maserowej. Problem ten został rozwiązany przez zwiększenie czasu obserwacji jednego źródła ($t = 1\,h$) i usuwanie skanów z silnymi zakłóceniami.

Obserwacje 153 źródeł, znanych z emisji 6.7 GHz przyniosły detekcję w 36 z nich. Cztery zaobserwowane źródła były zupełnie nowe: G50.035+0.582, G85.410+0.003, G107.298+6.639 i G183.348−0.575 - przedstawione nazwy źródeł odnoszą się do ich współrzędnych galaktycznych. Porównanie ze znanymi profilami emisji 6.7 GHz ujawniło bardzo wysoki poziom zgodności między profilami emisji w obydwu przejściach. Wynik ten jest

spójny z poprzednimi badaniami tego typu i wynika on z faktu że emisja 6.7 i 12 GHz powstaje w bardzo zbliżonych warunkach. Analiza zmienności G107.298+5.639 ujawniła periodyczny charakter emisji masera metanolu 12.2 GHz. Obserwowana wcześniej linia 6.7 GHz zmienia się w taki sam sposób (okres: 34.4 dnia) i pozostaje w antykorelacji z emisją masera wody 22 GHz (Szymczak et al., 2016). Analiza profili (Rys. 2.1) sugeruje, że emisja 12.2 GHz osiąga maksimum 0.8 - 1 dzień przed emisją 6.7 GHz. Ta zależność jest wytłumaczalna na gruncie modelu, przedstawionego w Cragg et al. (2002) przy założeniu, że przyczyną tak silnej zmienności jest zwiększenie efektywności pompowania w wyniku wzrostu temperatury pyłu od ∼130 do ∼170 K.

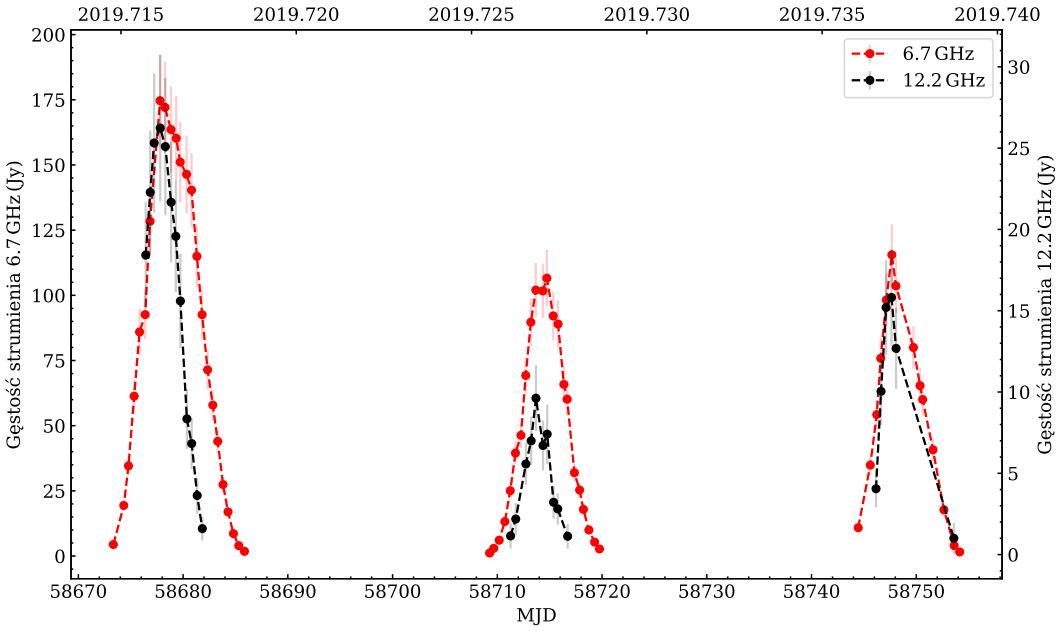

Rys. 2.1: Periodyczna zmienność cechy widmowej o $V_{lsr} = -7.4\,km\,s^{-1}$ w G107.298+5.639 w liniach 6.7 (czerwony) i 12.2 GHz (czarny).

24 spośród 36 naszych detekcji zostało również zaobserwowane 10 lat wcześniej w ramach przeglądu, wykonywanego przez 64 m radioteleskop w Parkes w Australii w przejściach 12.2 oraz 6.7 GHz (Breen et al., 2016, 2015), co pozwoliło na zbadanie poziomu zmienności obu przejść w skali czasowej ∼10 lat (ostatecznie do tego porównania wybrane zostało 17 źródeł, gdyż dla pozostałych siedmiu emisja nakłada się na profil widmowy innego, pobliskiego obiektu). Porównanie wykazało, że linia 12.2 GHz jest w ogólności bardziej zmienna w długich skalach czasowych, niż linia 6.7 GHz (Rys. 2.3), co jest zgodne z modelami teoretycznymi (Cragg et al., 2002, 2005). Porównanie gęstości strumienia odizolowanych cech widmowych w widmach 6.7 i 12.2 GHz ukazuje dużą rozpiętość stosunków

gęstości strumienia ($\frac{F_{6.7}}{F_{12.2}}$): od 1.5 do 51 z medianą na poziomie 5.1, co jest wartością podobną do uzyskanych w poprzednich pracach tego typu.

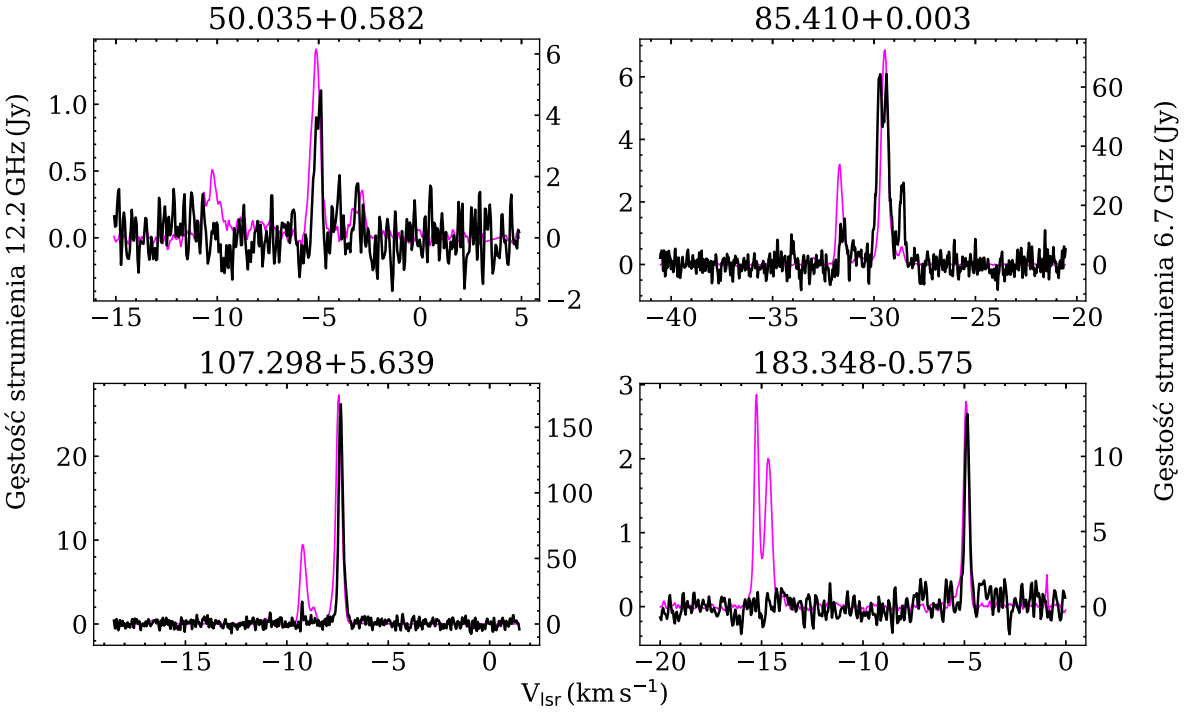

Rys. 2.2: Cztery nowo odkryte masery metanolu 12.2 GHz (czarne) i porównanie ich profili widmowych do emisji 6.7 GHz (magenta) .

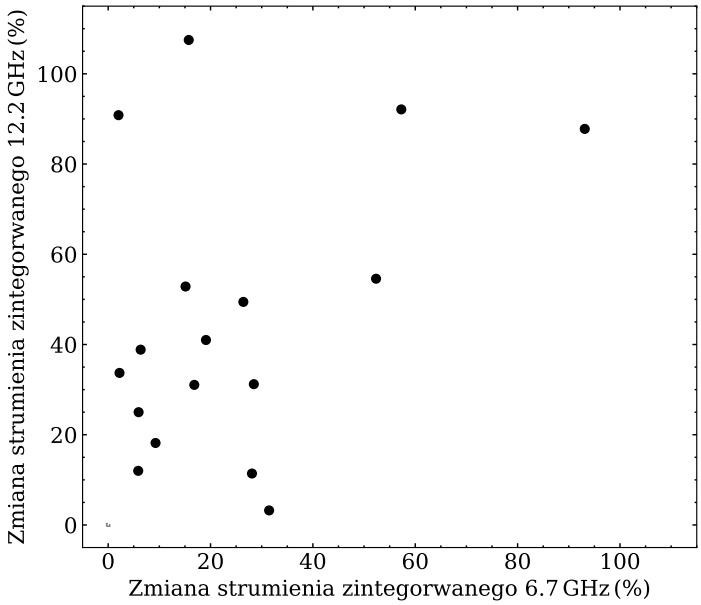

Rys. 2.3: Względne zmiany gęstości strumienia między 2008 a 2019 rokiem w liniach 6.7 GHz (Breen et al. 2015, archiwalne obserwacje RT32) oraz 12.2 GHz (Breen et al., 2016; Durjasz et al., 2021).

2.2 Odkrycie powtarzających się flar 6.7 GHz masera metanolu w Cep A HW2

W publikacji *Discovery of recurrent flares of 6.7 GHz methanol maser emission in Cepheus A HW2* (Durjasz et al., 2022) przedstawiliśmy rezultaty ponad 10-letniego monitoringu źródła Cep A HW2 w linii 6.7 GHz oraz rezultaty dwóch projektów obserwacyjnych, realizowanych przez sieć EVN o kodach RD002 (02.06.2020) oraz ED048B (18.10.2022). Dane spektroskopowe zostały zebrane w ramach kontynuacji projektu systematycznego monitorowania wielu maserów metanolu (Szymczak et al., 2018b) i były one gromadzone przez 32 m radioteleskop w Piwncach (własności obserwacji spektroskopowych zostały opisane w sekcji 1.2.3, sposoby redukcji danych VLBI - w 1.2.4).

Celem obserwacji interferometrycznych VLBI (Very Long Baseline Interferometry) było zbadanie poczerwienionych (względem pozostałej emisji 6.7 GHz, $V_{lsr} > -1.4\,km\,s^{-1}$) cech widmowych o niskiej amplitudzie, pojawiających się regularnie co ∼5 lat. Detekcja tej emisji była raportowana wcześniej (Szymczak et al., 2014), nowy zestaw danych dał możliwość przeprowadzenia obserwacji VLBI w momencie, kiedy opisywana poczerwieniona flara została wykryta w danych spektroskopowych z 32 m radioteleskopu (tzw. *single-dish guided VLBI*). Wyniki naszych projektów EVN porównaliśmy do archiwalnych danych VLBI.

Na podstawie danych z 32 m radioteleskopu oszacowaliśmy okres występowania flarującej emisji na ∼1800 dni, udało się również zlokalizować ją w bezpośrednim sąsiedztwie dysku pyłowego, wykrytego przez Patel et al. (2005). Poczerwieniona emisja została zaobserwowana również w dwóch archiwalnych projektach VLBI: JVN z 09.09.2006 (Sugiyama et al., 2014) oraz EVN z 13.03.2015 (Sanna et al. 2017, kod: ES071C) - potwierdza to zgodność z wyznaczoną przez nas 5-letnią okresowością. Dodatkowo na podstawie archiwalnych obserwacji udało się nam stwierdzić, że obserwowana w tym samym regionie poniebieszczona emisja ($V_{lsr} < -1.4\,km\,s^{-1}$) również zwiększa swoją amplitudę w okresie aktywności emisji poczerwienionej, nie jest jednak ona widoczna na widmach z 32 m radioteleskopu gdyż pokrywa się ze znacznie jaśniejszymi cechami widmowymi, pochodzącymi z innych regionów Cep A HW2. W widmach 32m zaobserwowaliśmy dryf prędkości radialnej flarujących cech widmowych, co sugerowało występowanie ruchów własnych i udało się takie zaobserwować w danych wysokiej rozdzielczości - oszacowałem prędkość ruchów

własnych na -2.06 ± 0.12 km s^{-1} w rektascensji i -2.91 ± 0.17 km s^{-1} w deklinacji, co przy znanej geometrii (Sanna et al., 2017) pozwoliło oszacować prędkość spadku w stronę centrum układu na ok. 4 km s^{-1}.

Na podstawie danych obserwacyjnych podjęliśmy próbę wyjaśnienia przyczyn występowania tego typu quasi-periodycznej emisji. Tego typu krzywe blasku (szybki wzrost i powolny spadek) był wielokrotnie uzyskiwane w teoretycznych modelach, tłumaczących emisję periodyczną maserów CH_3OH.

Mechanizm κ może prowadzić do niestabilności pulsacyjnej masywnej, młodej gwiazdy (Inayoshi et al., 2013a). W takim modelu zmiany w jasności centralnej gwiazdy układu wpływają pośrednio na emisję maserową, zwiększając pompowanie poprzez absorpcję strumienia UV przez pył i jego reemisję w zakresie IR. Mechanizm κ wiąże ścisłą relacją okres pulsacji i masę gwiazdy (Inayoshi et al. 2013b, równanie 2) - w przypadku Cep A HW2, 5 - letni cykl sugeruje masę ok. 40 $M_\odot$. Jest to wartość dużo wyższa, niż raportowana w oszacowaniach opartych o przesłanki obserwacyjne (np. Sanna et al. 2017), zatem nie jest to prawdopodobne wytłumaczenie obserwowanej zmienności. Scenariusz *Colliding Wind Binary*, zaproponowany przez van der Walt (2011) opisuje interakcje z wiatrem gwiazdowym w układzie podwójnym. Skutkują one generowaniem dodatkowej emisji free-free - wytworzone w ten sposób fotony kontrybuują do strumienia seed photons (pierwotnych fotonów, wymuszających emisję w obłoku maserowym), czego obserwowanym skutkiem jest pojaśnienie masera. Zwiększenie strumienia seed photons nie poskutkuje pojaśnieniem, jeśli poziom saturacji obłoku jest wysoki, co jest w stanie wytłumaczyć periodyczną zmienność tylko niektórych obłoków wokół Cep A HW2. Mechanizm ten nie jest jednak w stanie wytłumaczyć obserwowanych zapóźnień między emisją obłoków o prędkościach $V_{lsr} = -1.3$ i -0.5 km s^{-1}. Parfenov & Sobolev (2014) postulują istnienie spiralnych szoków w centralnej przerwie dysku akrecyjnego w układzie OB. Generowane przez ruch orbitalny w układzie podwójnym, szoki wchodzą w interakcje z gęstszą materią dysku, co skutkuje wzrostem promieniowania podczerwonego. Fotony z dalekiej podczerwieni zwiększają pompowanie maserów CH_3OH, co skutkuje wzrostem emisji. Ponieważ efektywność pompowania jest powiązana z temperaturą jasnościową masera w relacji eksponencjalnej, niewielki wzrost pompowania może prowadzić do znacznego względnego wzrostu obserwowanej jasności masera - jest to zgodne z naszymi obserwacjami, które wykazały względny wzrost emisji w czasie trwania pojaśnienia o dwa rzędy wielkości. Model ten jednak jest silnie ograniczony

przez geometrię układu - charakterystyczny profil z gwałtownym wzrostem i powolnym spadkiem został uzyskany przez autorów dla wymodelowanego układu, znajdującego się w orientacji edge-on, co nie jest prawdą w przypadku Cep A HW2. Najbardziej prawdopodobnym wytłumaczeniem tego fenomenu są niezbyt duże, periodyczne zmiany w jasności samego źródła kontinuum Cep A HW2, wywołane obecnością towarzysza - nie wpływają one w znacznym stopniu na jasne, silnie saturowane obłoki maserujące, jednak powodują znaczny względny przyrost jasności w przypadku obłoków niesaturowanych.

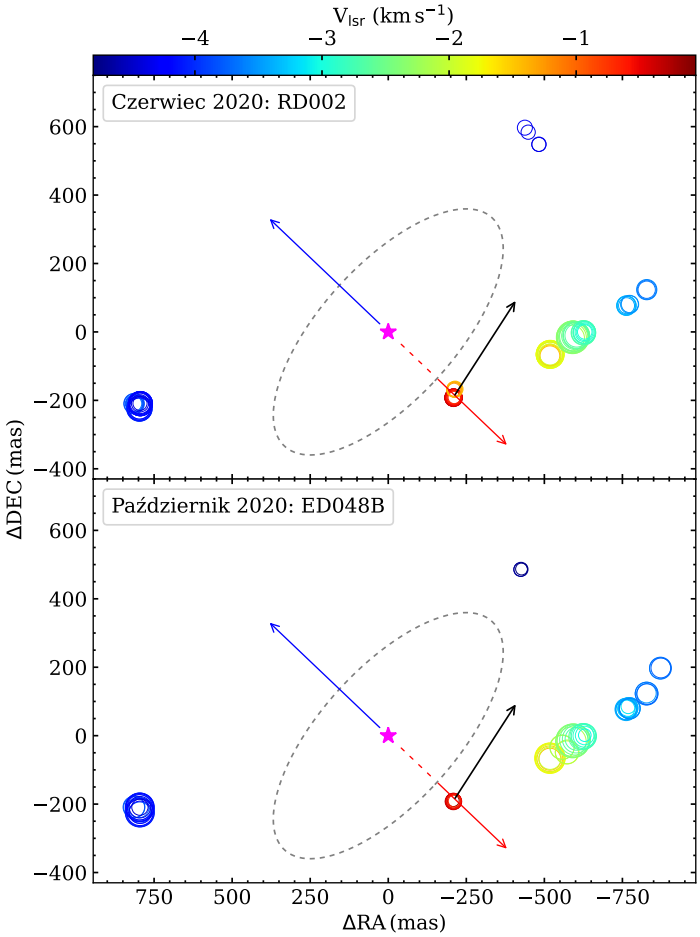

Rys. 2.4: Rozkład przestrzenny emisji maserów metanolu na częstotliwości 6.7 GHz wokół Cep A HW2 w czerwcu (góra) i październiku 2020 (dół). Rozmiar symboli skalowany jest z logarytmem szczytowej jasności, jego kolor odpowiada prędkości wzdłuż linii widzenia wg. skali pokazanej na górze wykresu. Purpurowy symbol oznacza pozycję Cep A HW2 (Curiel et al., 2006): α(J2000)=$22^{\mathrm{h}}56^{\mathrm{m}}17.9816^{\mathrm{s}}$, δ(J2000)=62°01′49.572″. Elipsą zaznaczona została pozycja dysku pyłowego obserwowanego w podczerwieni ($\lambda = 0.9$ mm, Patel et al. 2005). Strzałki czerwona i niebieska wskazują kierunki wydłużonej emisji, zaobserwowanej u podstawy dżetów w Carrasco-González et al. (2021), czarna - kierunek ruchów własnych poczerwienionej, periodycznej emisji. .

Dodatkowymi efektami tej pracy są:

- Potwierdzenie wcześniej raportowanego, sub-Keplerowskiego modelu dysku wokół Cep A HW2 (Sanna et al., 2017; Sugiyama et al., 2014).
- Obserwacja synchronicznej i antyskorelowanej zmienności między cechami -2.6 i $-4.7\,\mathrm{km\,s^{-1}}$, sugerująca występowanie oddziaływań promienistych między różnymi obłokami maserującymi wokół Cep A HW2 (Cesaroni, 1990).

2.2.1 Oddziaływanie promieniste między obłokami maserującymi (Cesaroni, 1990)

Rysunek 2.5 przedstawia wizualizację mechanizmu promienistego oddziaływania między obłokami maserującymi, opisanego w Cesaroni (1990). W tym modelu potrzebujemy (I) dwóch obłoków maserujących (1 i 2). W układzie spoczynkowym obłoku 1, emisja z 2 nie jest przesunięta dopplerowsko. Z punktu widzenia ziemskiego obserwatora obłoki te mogą mieć różne prędkości radialne. (II) zwiększenie jasności obłoku 2 poprzez wzrost efektywności pompowania powoduje wzrost emisji we wszystkich kierunkach - również w stronę obłoku 1. (III) gwałtowny wzrost ilości fotonów wymuszających emisję przy podobnej prędkości pompowania powoduje spadek ilości dostępnych molekuł, gotowych wyemitować foton na drodze emisji wymuszonej. W efekcie obserwator ziemski dostrzega najpierw przyrost emisji z obłoku 2, a w późniejszym etapie spadek emisji z obłoku 1. Rysunek 2.6 przedstawia rzeczywiste krzywe blasku cech widmowych o prędkościach $\mathrm{V_{lsr}} = -4.7$ i $-2.6\,\mathrm{km\,s^{-1}}$ w okresie maj-grudzień 2022. Dla lepszego wyglądu, zostały one wygładzone za pomocą średniej kroczącej ($\Delta\mathrm{t} = 30$ dni). Widoczny jest znaczny spadek emisji cechy $-2.6\,\mathrm{km\,s^{-1}}$ przy wzroście emisji na $-4.7\,\mathrm{km\,s^{-1}}$. Maksimum emisji $-4.7\,\mathrm{km\,s^{-1}}$ poprzedza minimum emisji $-2.6\,\mathrm{km\,s^{-1}}$ o ok. 4.5 dnia, co przy założeniu rozchodzenia się oddziaływania z prędkością światła $\mathrm{c} = 299792458\,\mathrm{m\,s^{-1}}$ przekłada się na odległość $\sim$790 AU. Odległość między tymi obłokami oszacowana z użyciem kąta inklinacji, przedstawionego w Sanna et al. (2017) to ok. 750 AU.

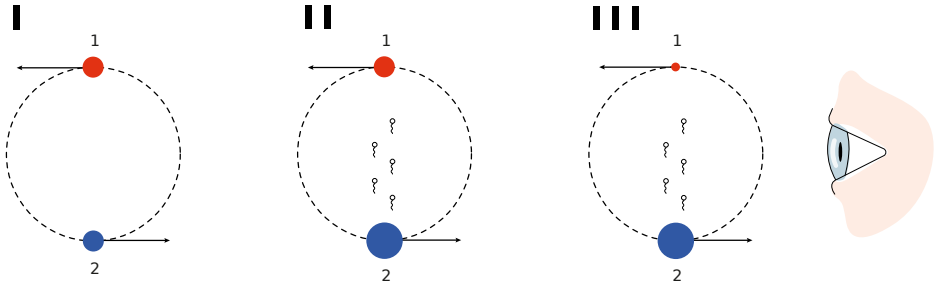

Rys. 2.5: Wizualizacja modelu Cesaroni (1990).

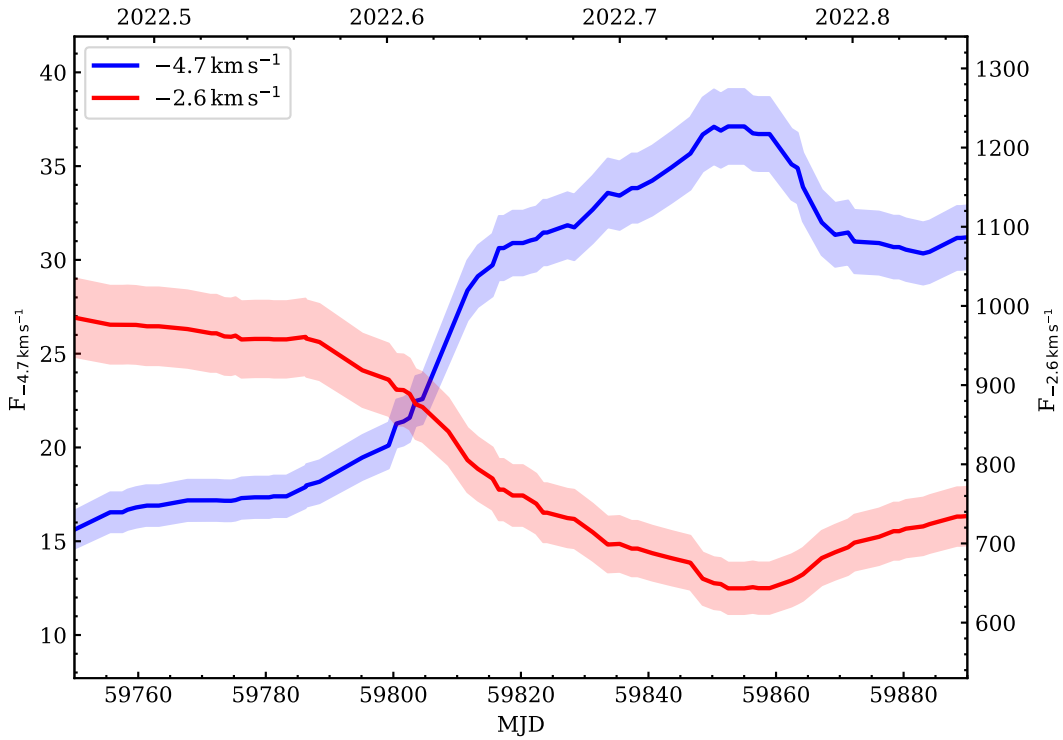

Rys. 2.6: Krzywe blasku cech widmowych o prędkościach $V_{lsr} = -4.7$ i $-2.6\,km\,s^{-1}$.

2.3 Odkrycie periodycznych pojaśnień 6.7 GHz masera metanolu w źródłach G45.804−0.356 i G49.043−1.079

W publikacji *Detection of periodic flares in 6.7 GHz methanol masers G45.804−0.356 and G49.043−1.079* (Olech et al., 2022) przedstawiliśmy wyniki analizy z ponad dziesięciu lat (06.2009 - 10.2021) obserwacji 6.7 GHz masera metanolu w źródłach G45.804−0.356 i G49.043−1.079 (Rys. odpowiednio 2.7 i 2.8). Parametry obserwacji były takie same, jak w przypadku publikacji Durjasz et al. (2022) i można je znaleźć w sekcji 1.2.3. Krzywe blasku poszczególnych cech widmowych analizowaliśmy za pomocą periodogramu Lomb-Scargle (Scargle, 1982) używając pakietu Astropy (Astropy Collaboration et al., 2013, 2018, 2022) oraz własnej implementacji algorytmu AoV (analysis of variance, Schwarzenberg-Czerny 1989). Wyznaczone okresy zmienności to 416.9 i 469.3 dni dla źródeł odpowiednio G45.804−0.356 i G49.043−1.079. Na podstawie danych NEOWISE (pasma 3.4 oraz 4.6 μm) zaobserwowaliśmy, że w G49.043−1.079 równocześnie z pojaśnieniami w linii 6.7 GHz rośnie obserwowana gęstość strumienia w zakresie IR. Zmierzone zapóźnienia między różnymi cechami widmowymi w linii 6.7 GHz wynoszą aż 68 dni, co oznacza, że prawdopodobnie nie są one wynikiem geometrii układu wzdłuż linii widzenia. W przypadku tego źródła ustaliliśmy, że periodyczna zmienność jest najprawdopodobniej spowodowana przez zmienne tempo akrecji, modulujące efektywność pompowania masera. Nie udało się jednoznacznie wskazać scenariusza zmienności w przypadku G45.804−0.356. Większość z 26 wcześniej odkrytych źródeł periodycznych charakteryzuje się okresami między 100 a 300 dni i tylko 4 obiekty zmieniają się z okresem dłuższym, niż 400 dni; nasze odkrycia poszerzyły grupę znanych źródeł tego typu do 28.

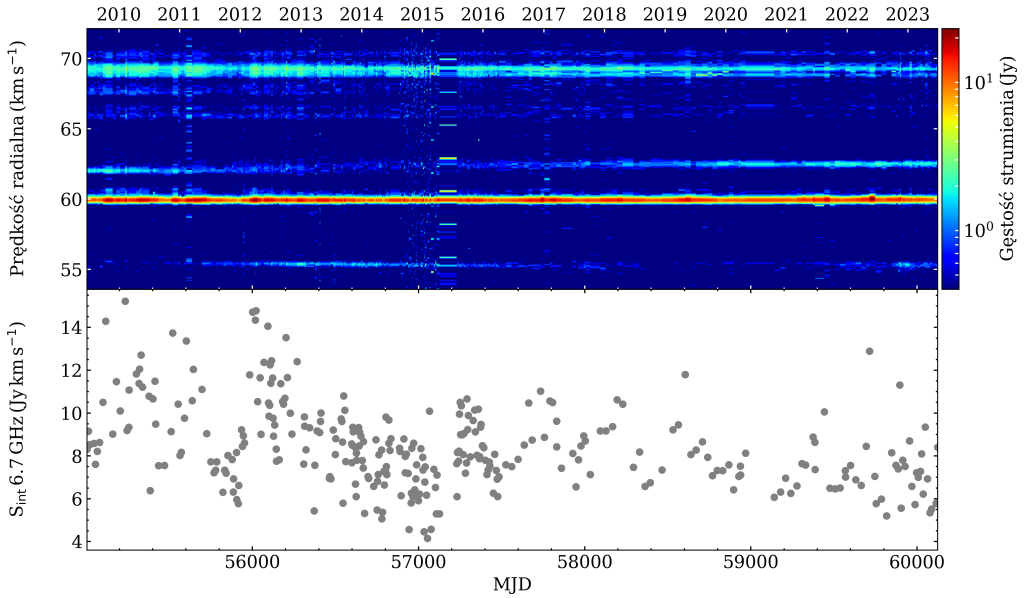

Rys. 2.7: *Góra*: widmo dynamiczne emisji maserów metanolu w linii 6.7 GHz w G45.804−0.356 - gęstość strumienia jest przedstawiona w postaci koloru, opisywanego przez skalę widoczną po prawej stronie, *dół*: krzywa blasku strumienia zintegrowanego 6.7 GHz.

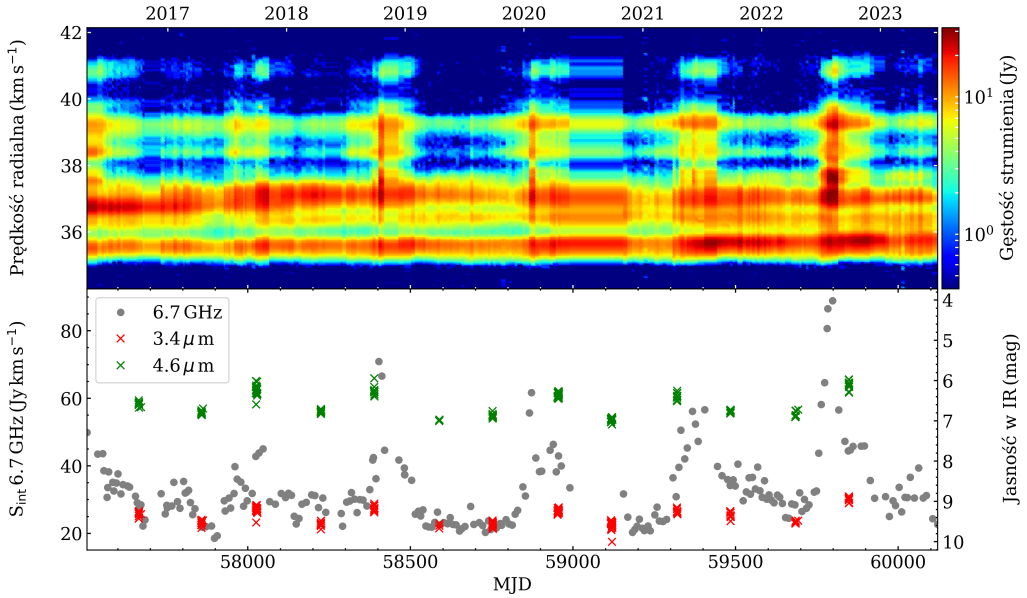

Rys. 2.8: *Góra*: widmo dynamiczne emisji maserów metanolu w linii 6.7 GHz w G49.043−1.079. *dół*: krzywa blasku strumienia zintegrowanego 6.7 GHz oraz zmienność w bliskiej podczerwieni. Obserwacje fotometryczne w zakresie IR wykonane zostały przez satelitę NEOWISE i zarchiwizowane w NASA/IPAC Infrared Science Archive[2].

[2] https://irsa.ipac.caltech.edu/frontpage/

Rozdział 3

Podsumowanie

Głównym wynikiem mojej pracy jest dostarczenie nowych danych dotyczących zmienności maserów. Linia masera CH_3OH 12.2 GHz wykazuje się większą zmiennością w porównaniu z linią 6.7 GHz, co sugeruje wyższą podatność na zmianę warunków fizycznych w otoczeniu obłoku maserującego. W konsekwencji obserwacje linii 12.2 GHz mogą być bardziej skuteczną metodą poszukiwania aktywności młodych, masywnych gwiazd. Udało mi się również zwiększyć liczbę znanych źródeł periodycznych. Badania nad Cep A HW2 pozwoliły na obserwacyjne potwierdzenie występowania efektu *radiative connection*, przewidzianego w Cesaroni (1990). Źródło to charakteryzuje się również występowaniem periodycznej emisji, której własności nie są odwzorowywane przez obecnie dostępne modele teoretyczne – wskazuje to na konieczność dalszej pracy nad ich rozwijaniem w celu uwzględnienia m.in. efektu *nadpromienistości Dickego* (Rajabi et al., 2019). Moja analiza ruchów własnych obłoków maserujących w otoczeniu Cep A HW2 potwierdza poprzednie prace sugerujące ruch w stronę centrum układu połączony z bardzo powolną, sub-Keplerowską rotacją. Przyszłe prace obserwacyjne na tym polu powinny skupiać się na próbie zbadania kinematyki dysków wokół masywnych, młodych gwiazd dla bardziej reprezentatywnej próbki obiektów.

Bibliografia

Astropy Collaboration et al., 2013, A&A , 558, A33

Astropy Collaboration et al., 2018, AJ , 156, 123

Astropy Collaboration et al., 2022, apj, 935, 167

Błaszkiewicz L., Kus A. J., 2004, A&A , 413, 233

Breen S. L., Ellingsen S. P., Caswell J. L., Lewis B. E., 2010, MNRAS , 401, 2219

Breen S. L., Ellingsen S. P., Caswell J. L., Green J. A., Voronkov M. A., Fuller G. A., Quinn L. J., Avison A., 2012, MNRAS , 426, 2189

Breen S. L., et al., 2015, MNRAS , 450, 4109

Breen S. L., Ellingsen S. P., Caswell J. L., Green J. A., Voronkov M. A., Avison A., Fuller G. A., Quinn L. J., 2016, MNRAS , 459, 4066

Burns R. A., et al., 2020, Nature Astronomy, 4, 506

Burns R. A., et al., 2023, Nature Astronomy,

Caratti o Garatti A., et al., 2017, Nature Physics, 13, 276

Carrasco-González C., Sanna A., Rodríguez-Kamenetzky A., Moscadelli L., Hoare M., Torrelles J. M., Galván-Madrid R., Izquierdo A. F., 2021, ApJ , 914, L1

Caswell J. L., Gardner F. F., Norris R. P., Wellington K. J., McCutcheon W. H., Peng R. S., 1993, MNRAS , 260, 425

Caswell J. L., Vaile R. A., Ellingsen S. P., Norris R. P., 1995, MNRAS , 274, 1126

Cesaroni R., 1990, A&A , 233, 513

Cragg D. M., Sobolev A. M., Godfrey P. D., 2002, MNRAS , 331, 521

Cragg D. M., Sobolev A. M., Godfrey P. D., 2005, MNRAS, 360, 533

Curiel S., et al., 2006, ApJ , 638, 878

Durjasz M., Szymczak M., Wolak P., Bartkiewicz A., 2021, A&A , 648, A118

Durjasz M., Szymczak M., Olech M., Bartkiewicz A., 2022, A&A , 663, A123

Elitzur M., 1992, Astronomical masers. Vol. 170, doi:10.1007/978-94-011-2394-5,

Fujisawa K., Yonekura Y., Sugiyama K., Horiuchi H., Hayashi T., Hachisuka K., Matsumoto N., Niinuma K., 2015, The Astronomer's Telegram, 8286, 1

Gray M., 2012, Maser Sources in Astrophysics. Cambridge University Press

Hunter T. R., et al., 2017, ApJ , 837, L29

Inayoshi K., Hosokawa T., Omukai K., 2013a, MNRAS , 431, 3036

Inayoshi K., Sugiyama K., Hosokawa T., Motogi K., Tanaka K. E. I., 2013b, ApJ , 769, L20

Jijina J., Adams F. C., 1996, ApJ , 462, 874

Kahn F. D., 1974, A&A , 37, 149

Keimpema A., et al., 2015, Experimental Astronomy, 39, 259

Kemball A. J., Gaylard M. J., Nicolson G. D., 1988, ApJ , 331, L37

Kenyon S. J., Hartmann L., 1995, ApJS , 101, 117

Kenyon S. J., Hartmann L. W., Strom K. M., Strom S. E., 1990, AJ , 99, 869

Kenyon S. J., Gomez M., Marzke R. O., Hartmann L., 1994, AJ , 108, 251

Koo B.-C., Williams D. R. D., Heiles C., Backer D. C., 1988, ApJ , 326, 931

Krumholz M. R., Klein R. I., McKee C. F., Offner S. S. R., Cunningham A. J., 2009, Science, 323, 754

Kus A., Borkowski K., 2011, 32m radioteleskop: Opis techniczny i podręcznik obserwatora. Centrum Astronomii UMK, Katedra Radioastronomii

Lew B., 2018, Experimental Astronomy, 45, 81

Meyer D. M. A., Vorobyov E. I., Kuiper R., Kley W., 2017, MNRAS , 464, L90

Meyer D. M. A., Vorobyov E. I., Elbakyan V. G., Stecklum B., Eislöffel J., Sobolev A. M., 2019, MNRAS , 482, 5459

Meyer D. M. A., Vorobyov E. I., Elbakyan V. G., Kraus S., Liu S. Y., Nayakshin S., Sobolev A. M., 2022, MNRAS , 517, 4795

Miao D., et al., 2022, ApJS , 263, 9

Moscadelli L., et al., 2017, A&A, 600, L8

Nakano T., Hasegawa T., Norman C., 1995, Ap&SS , 224, 523

Norris R. P., Caswell J. L., Gardner F. F., Wellington K. J., 1987, ApJ , 321, L159

Offner S. S. R., McKee C. F., 2011, ApJ , 736, 53

Olech M., Durjasz M., Szymczak M., Bartkiewicz A., 2022, A&A , 661, A114

Ott M., Witzel A., Quirrenbach A., Krichbaum T. P., Standke K. J., Schalinski C. J., Hummel C. A., 1994, A&A , 284, 331

Parfenov S. Y., Sobolev A. M., 2014, MNRAS , 444, 620

Patel N. A., et al., 2005, Nature , 437, 109

Pazderski E., 2018, in 2018 Baltic URSI Symposium (URSI). pp 33–37, doi:10.23919/URSI.2018.8406773

Rajabi F., Houde M., Bartkiewicz A., Olech M., Szymczak M., Wolak P., 2019, MNRAS , 484, 1590

Reid M. J., Moran J. M., 1981, ARA&A , 19, 231

Sanna A., et al., 2015, ApJ , 804, L2

Sanna A., Moscadelli L., Surcis G., van Langevelde H. J., Torstensson K. J. E., Sobolev A. M., 2017, A&A , 603, A94

Scargle J. D., 1982, ApJ , 263, 835

Schwarzenberg-Czerny A., 1989, MNRAS , 241, 153

Sobolev A. M., Cragg D. M., Godfrey P. D., 1997, A&A, 324, 211

Stumpff P., 1980, A&AS , 41, 1

Sugiyama K., et al., 2014, A&A , 562, A82

Szymczak M., Wolak P., Bartkiewicz A., Borkowski K. M., 2012, Astronomische Nachrichten, 333, 634

Szymczak M., Wolak P., Bartkiewicz A., 2014, MNRAS , 439, 407

Szymczak M., Olech M., Wolak P., Bartkiewicz A., Gawroński M., 2016, MNRAS, 459, L56

Szymczak M., Olech M., Sarniak R., Wolak P., Bartkiewicz A., 2018a, MNRAS, 474, 219

Szymczak M., Olech M., Sarniak R., Wolak P., Bartkiewicz A., 2018b, MNRAS , 474, 219

Xu L.-H., 2001, in Demaison J., Sarka K., Cohen E. A., eds, Spectroscopy from Space. p. 131

Zinnecker H., Yorke H. W., 2007, ARA&A, 45, 481

van der Walt D. J., 2011, AJ , 141, 152

Lista prac naukowych

Mam udział w 12 publikacjach naukowych: w tym 9 recenzowanych i 3 konferencyjnych. Lista publikacji jest zaprezentowana poniżej (pogrubione tytuły oznaczają publikacje wchodzące w skład niniejszej pracy doktorskiej, których streszczenia zostały zaprezentowane w rozdziale 2):

Publikacje recenzowane

1. Durjasz, M., Szymczak, M., Olech, M., *A highly variable methanol maser in G111.256-0.770*, 2019, Monthly Notices of the Royal Astronomical Society, Volume 485, Issue 1, p.777-783, DOI: 10.1093/mnras/stz472

2. Szymczak, M., Wolak, P., Bartkiewicz, A., Aramowicz, M., Durjasz, M., *A search for the OH 6035 MHz line in high-mass star-forming regions*, 2020, Astronomy & Astrophysics, Volume 642, id.A145, 14 pp., DOI: 10.1051/0004-6361/202039009

3. Durjasz, M., Szymczak, M., Wolak, P., Bartkiewicz, A., ***Observations of 12.2 GHz methanol masers towards northern high-mass protostellar objects***, 2021, Astronomy & Astrophysics, Volume 648, id.A118, 13 pp., DOI: 10.1051/0004-6361/202140385

4. Olech, M. and Durjasz, M. and Szymczak, M. and Bartkiewicz, A., ***Detection of periodic flares in 6.7 GHz methanol masers G45.804−0.356 and G49.043−1.079***, 2022, Astronomy & Astrophysics, Volume 661, id.A114, 7 pp., DOI: 10.1051/0004-6361/202243108

5. Durjasz, M. and Szymczak, M. and Olech, M. and Bartkiewicz, A., ***Discovery of recurrent flares of 6.7 GHz methanol maser emission in Cepheus A HW2***, 2022, Astronomy & Astrophysics, Volume 663, id.A123, 16 pp., DOI: 10.1051/0004-6361/202243552

6. Hirota et al., *Millimeter methanol emission in the high-mass young stellar object G24.33+0.14*, 2022, Publications of the Astronomical Society of Japan, Volume 74, Issue 5, pp.1234-1262, DOI: 10.1093/pasj/psac067

7. Burns et al., *A Keplerian disk with a four-arm spiral birthing an episodically accreting high-mass protostar*, 2023, Nature Astronomy, Volume 7, p. 557-568, DOI: 10.1038/s41550-023-01899-w

8. Kobak et al., *Multi-frequency VLBI observations of maser lines during the 6.7 GHz maser flare in the high-mass young stellar object G24.33+0.14*, 2023, Astronomy & Astrophysics, Volume 671, id.A135, 26 pp., DOI: 10.1051/0004-6361/202244772

9. Aberfelds et al., *Milliarcsecond structure and variability of methanol maser emission in three high-mass protostars*, 2023, Monthly Notices of the Royal Astronomical Society, Volume 524, Issue 1, pp.599-618, DOI: 10.1093/mnras/stad1752

Publikacje konferencyjne

1. Bartkiewicz et al., *Toruń Maser Group Highlights*, 2020, Proceedings of the Polish Astronomical Society, Vol. 10. pp.166-168, ISBN: 978-83-950430-8-6, dostępny w internecie: https://www.pta.edu.pl/pliki/proc/vol10/v10p166.pdf

2. Burns et al., *Recent updates on the Maser Monitoring Organisation*, 2021, European VLBI Network Mini-Symposium and Users' Meeting 2021, 12-14 July, 2021, DOI: 10.22323/1.399.0019

3. Durjasz, M. and Szymczak, M., *New 6.7 GHz imaging of the high-mass star-forming region Cep A HW2*, 2022, 15th EVN Mini-Symposium and User's Meeting, University College Cork, Ireland, July 11, 2022, id. 1, DOI: 10.22323/1.428.0030

A&A 648, A118 (2021)
https://doi.org/10.1051/0004-6361/202140385
© ESO 2021

Astronomy & Astrophysics

Observations of 12.2 GHz methanol masers towards northern high-mass protostellar objects

M. Durjasz, M. Szymczak, P. Wolak, and A. Bartkiewicz

Institute of Astronomy, Faculty of Physics, Astronomy and Informatics, Nicolaus Copernicus University, Grudziadzka 5, 87-100 Torun, Poland
e-mail: md@astro.umk.pl

Received 20 January 2021 / Accepted 12 March 2021

ABSTRACT

Context. Class II methanol masers at 6.7 and 12.2 GHz occur close to high-mass young stellar objects (HMYSOs). When they are observed simultaneously, such studies may contribute to refining the characterisation of local physical conditions.
Aims. We aim to search for the 12.2 GHz methanol emission in 6.7 GHz methanol masers that might have gone undetected in previous surveys of northern sky HMYSOs, mainly due to their variability. Contemporaneous observations of both transitions are used to refine the flux density ratio and examine the physical parameters.
Methods. We observed a sample of 153 sites of 6.7 GHz methanol maser emission in the 12.2 GHz methanol line with the Torun 32 m radio telescope, using the newly built *X*-band receiver.
Results. The 12.2 GHz methanol maser emission was detected in 36 HMYSOs, with 4 of them detected for the first time. The 6.7–12.2 GHz flux density ratio for spectral features of the contemporaneously observed sources has a median value of 5.1, which is in agreement with earlier reports. The ratio differs significantly among the sources and for the periodic source G107.298+5.639 specifically, the ratio is weakly recurrent from cycle to cycle, but it generally reaches a minimum around the flare peak. This is consistent with the stochastic maser process, where small variations in the physical parameters along the maser path can significantly affect the ratio. A comparison of our data with historical results (from about ten years ago) implies significant (>50%) variability for about 47 and 14% at 12.2 and 6.7 GHz, respectively. This difference can be explained via the standard model of methanol masers.

Key words. masers – stars: massive – stars: formation – ISM: molecules – radio lines: ISM

1. Introduction

Masers play a significant role in the study of the interstellar medium. The methanol molecule has attracted much attention, from its first detection half a century ago (Barrett et al. 1971) to the present, given the multitude of observed transitions. One of the breakthroughs in the field came with the detection of the strongest, and most pervasive, lines at 12.2 (Batrla et al. 1987) and 6.7 GHz (Menten 1991), which provided powerful tools for identifying high-mass young stellar objects (HMYSOs) and exploring the physical conditions and gas kinematics of their surroundings. A number of new methanol transitions in the centimetre (Breen et al. 2019; MacLeod et al. 2019) and millimetre (Brogan et al. 2019) ranges have been discovered very recently in objects that have undergone major accretion events.

The 6.7 and 12.2 GHz lines are referred to as class II methanol maser transitions (Batrla et al. 1987; Menten 1991) that are characterised by radiative pumping (Cragg et al. 2005) and a close association with sources of strong radiation. They are usually found in the vicinity of HYMSOs, as revealed by several surveys at 6.7 GHz (e.g. Caswell et al. 1995b; Ellingsen et al. 1996; Pandian et al. 2007; Szymczak et al. 2012; Green et al. 2010; Breen et al. 2015). Several searches for the 12.2 GHz methanol maser emission were carried out prior to the discovery of the 6.7 GHz line, mainly towards OH maser sites (Norris et al. 1987; Koo et al. 1988; Kemball et al. 1988; Caswell et al. 1993; MacLeod et al. 1993). Thereafter, all the 12.2 GHz surveys were done towards the 6.7 GHz sources (Gaylard et al. 1994; Caswell et al. 1995a; Błaszkiewicz & Kus 2004; Breen et al. 2010, 2012a,b, 2014, 2015), as the 12.2 GHz line excitation conditions closely follow those at 6.7 GHz (Cragg et al. 2002). Almost all of these surveys did not cover the entire northern sky, thus, in this study, we attempt to supplement the observations with objects of the northern hemisphere.

No conclusive data is available on the variability patterns of the 12.2 GHz methanol masers. Little or no variability was noticed on a timescale of seven months in eight bright (>100 Jy) 12.2 GHz maser sources (McCutcheon et al. 1988), whereas in the other five bright sources, the emission varied internally by less than 15–20% over a four-year period with the exception of single weak features in two sources (MacLeod et al. 1993). In turn, Caswell et al. (1993) reported the 12.2 GHz flux density variations on a timescale of weeks and later found that at least a quarter of the features exhibit intensity variations larger than 10% on a timescale of 4 yr (Caswell et al. 1995a) suggesting that most quiescent 12.2 GHz masers are saturated. In this paper, we present the results of multi-epoch 12.2 GHz observations, along with a comparison to historical observations, for 153 sources. We include several contemporaneously monitored 6.7 GHz methanol maser counterparts.

2. Observations

Observations were carried out in the period from 2019 August to 2020 February using the Torun 32 m radio telescope. The telescope has a half-power beam width of about 3′ at 12.2 GHz and

rms pointing errors of about 10″. The adopted rest frequency was 12.178597 GHz (Müller et al. 2004). We used the newly built *X*-band receiver (Pazderski 2018), which is a dual-polarisation cooled receiver with amplifiers of typical noise temperature of 5 K. Here, the system temperature was about 30 K. The antenna gain was estimated to be about 0.06 K Jy^{-1} from observations of calibrators DR21 and 3C123 adopting flux densities of 20.0 and 6.3 Jy, respectively (Ott et al. 1994). No gain elevation correction was applied; this can contribute less than 4% to the error budget of the flux density. The uncertainty in the flux density scale is about 15%.

The observations were made in frequency-switching mode. An autocorrelation spectrometer was configured to record 4096 channels either with 4 MHz or 8 MHz bandwidth for each circularly polarised signal yielding the channel spacing of 0.024 or 0.048 km s^{-1}, respectively. The velocity extent of each observation is ±45 or ±90 km s^{-1} with respect to the local standard of rest. A typical 3σ noise level in the final spectra with the higher spectral resolution was 1.5 Jy. The stability of the system was regularly checked with observations of G188.946+0.886 that show no variability to a limit of 15% during our observing interval, while its 12.2 GHz spectrum shape remained almost unchanged after $\gtrsim$10 yr when observed by Breen et al. (2012a). Observations of G188.946+0.886 during the 2000–2008 revealed periodic (395±8 d) variability with relative amplitudes of 0.5 and 0.7 at 6.7 and 12.2 GHz, respectively, but periodic changes at 12.2 GHz were barely visible prior to 2005 (Goedhart et al. 2014, their Figs. 9 and 10). In the period from 2009 to 2013, the relative amplitude of periodic variations at 6.7 GHz decreased to about 0.2 (Szymczak et al. 2018), whereas our unpublished 6.7 GHz observations, carried out contemporaneously with the present 12.2 GHz survey, show a variability that is lower than 10% We argue that the variability of this object at 12 GHz does not exceed the uncertainty of our measurements. For selected sources, contemporaneous (≤±7 d) observations were carried out in the 6.7 GHz methanol transition following the procedure described in Szymczak et al. (2018).

We selected bright 6.7 GHz sources (Breen et al. 2015; Szymczak et al. 2012; Hu et al. 2016; Green et al. 2010) that are observable from the northern hemisphere and mostly with a declination of >0° to avoid a degradation of the telescope sensitivity due to radio frequency interference from commercial satellites. The final sample consists of 153 sources.

3. Results

The 12.2 GHz maser emission was detected in 36 objects (Table 1), including four new sources. Figures 1 and A.1 present the spectra of newly detected and previously known sources, respectively. The list of non-detections is also given in Table A.1.

3.1. Newly detected 12.2 GHz sources

G50.035+0.582. This source has a single 12.2 GHz feature at −5.1 km s^{-1}, with $S_{12.2}$ = 1.1 Jy, which coincides with the strongest feature of the 6.7 GHz methanol maser (Szymczak et al. 2012; Breen et al. 2015). There was no 12.2 GHz maser emission detected in 2010 March with the 5σ sensitivity of 0.84 Jy (Breen et al. 2016). This implies a variability of ≥30% on a timescale of 9.5 yr.

G85.410+0.003. The 12.2 GHz spectrum is comprised of three features at −31.5, −29.5, and −28.6 km s^{-1}. These are coincident with their 6.7 GHz maser counterparts, within 0.1 km s^{-1}, observed in the same epoch. In instances where a single bright feature at $V_{12.2}$ = −29.5 km s^{-1} was originally detected, we now report two features separated by 0.3 km s^{-1}. A comparison with the Effelsberg 100 m spectrum taken on May 19, 2020 (Yen & Menten, priv. comm. at M2O[1]) implies significant changes in the profile shape and flux density of individual features by a factor of 2–3 over four months.

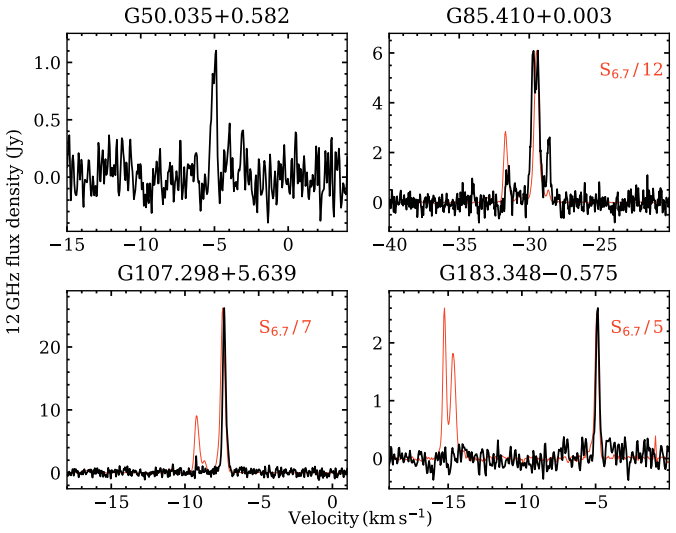

Fig. 1. Spectra of the newly detected 12.2 GHz methanol maser sources. Spectra of 6.7 GHz methanol masers (red) are also shown when taken on the same day, with exception of G183.348−0.575, where the interval between observations was 41 d. For comparison purposes, the scale of 6.7 GHz flux density was reduced by the factor given in the upper right corner.

G107.298+5.639. The single velocity feature is matched in velocity to the strongest 6.7 GHz feature at −7.35 km s^{-1} (Olech et al. 2020) during all three observed cycles, which are discussed in detail in Sect. 3.2. Hereafter, G107.298+5.639 is referred to as G107.

G183.348−0.575. The 12.2 GHz maser emission consists of a single feature at −4.9 km s^{-1} with a peak flux density of 2.5 Jy, which coincides in velocity with the 6.7 GHz maser feature. There was no 12.2 GHz maser emission seen for the blueshifted component of the 6.7 GHz emission near −15 km s^{-1}.

3.2. Case of G107

The 12.2 GHz maser emission follows periodic variations observed in the methanol 6.7 GHz and hydroxyl (1.665/1.667 GHz) maser lines (Szymczak et al. 2016; Olech et al. 2020). The upper panel in Fig. 2 presents the light curves of both methanol transitions. In order to estimate the parameters of flare profiles, we fitted an asymmetric power function (David et al. 1996; Szymczak et al. 2011), Gaussian function, and second-order polynomial to the 6.7 and 12.2 GHz data. The flare maximum and timescale of variability FWHM of the flare are listed in Table 2 for each transition and three cycles. For the asymmetric function fitting we get, in addition, the ratio of rise to decay time of the flare, which ranges from 0.8 to 1.1 and 0.7 to 0.9 for the 12.2 and 6.7 GHz lines, respectively. This suggests that the flare profile at 12.2 GHz is slightly more symmetric than the one at 6.7 GHz. The full width at half maximum (FWHM)

[1] https://www.masermonitoring.com

Table 1. Detected 12.2 GHz methanol maser sources.

Name (l b) (° °)	α (J2000) (h m s)	δ (J2000) (° ′ ″)	$V_{\rm peak}$ (km s^{-1})	$S_{\rm peak}$ (Jy)	ΔV (km s^{-1})	$S_{\rm int}$ (Jy km s^{-1})	Epoch (MJD)	References
G30.225−0.180	18 47 08.30	−02 29 28.90	113.35	6.7	107;116	8.76	58 723	9,11
G32.744−0.075	18 51 21.87	−00 12 05.00	30.55	3.7	29;40	5.81	58 769	6,9,11,14
G33.641−0.228	18 53 32.56	00 31 39.18	60.26	37.8	58;62	13.13	58 868	11,14
G35.132−0.744	18 58 06.14	01 37 07.50	29.72	11.8	27;32	10.83	58 872	14
G35.197−0.743	18 58 13.05	01 40 35.70	28.26	39.1	27;32	31.7	58 873	6,7,9,11,14
G35.200−1.736	19 01 45.54	01 13 32.60	45.16	11.9	43;47	4.23	58 873	2,4,5,6,9,10,11,14
G36.115+0.552	18 55 16.79	03 05 05.41	75.08	2.4	73;78	1.32	58 720	14
G37.043−0.035	18 59 04.41	03 38 32.80	83.88	3.0	83;85	0.85	58 880	14
G37.430+1.518	18 54 14.23	04 41 41.10	41.32	73.8	40;43	31.79	58 862	8,11,14
G37.546−0.112	19 00 16.05	04 03 16.09	50.03	1.1	49;51	0.58	58 866	14
G40.282−0.219	19 05 41.21	06 26 12.69	74.35	1.7	72;81	2.61	58 716	14
G40.425+0.700	19 02 39.62	06 59 10.50	6.62	7.9	5;16	5.60	58 827	14
G42.034+0.190	19 07 28.18	08 10 53.47	11.50	4.6	10;15	6.09	58 872	14
G43.149+0.013	19 10 11.05	09 05 20.40	13.64	2.4	13;15	0.94	58 766	1,9,11,14
G43.890−0.784	19 14 26.39	09 22 36.50	51.66	2.4	45;53	1.71	58 805	11,14
G45.804−0.356	19 16 31.08	11 16 12.01	60.01	1.3	59;61	0.18	58 762	14
G49.043−1.079	19 25 22.25	13 47 19.50	36.31	0.9	35;37	0.49	58 721	14
G49.265+0.311	19 20 44.85	14 38 26.91	−4.55	1.4	−7;−3	1.83	58 827	14
G49.349+0.413	19 20 32.44	14 45 45.44	68.14	2.0	66;70	1.24	58 860	14
G49.416+0.326	19 20 59.21	14 46 49.60	−10.18	0.8	−10.8;−9.5	0.45	58 726	11,14
G49.489−0.369	19 23 39.82	14 31 04.90	59.01	2.3	57;60	1.37	58 855	14
G49.490−0.388	19 23 43.95	14 30 34.20	56.13	10.1	55;57	5.30	58 855	1,5,6,9,11,12,14
G49.599−0.249	19 23 26.61	14 40 16.99	64.05	4.3	61;67	9.97	58 706	11,14
G50.035+0.582 [(a)]	19 21 15.45	15 26 49.20	−5.02	1.1	−6;−3	0.41	58 717	
G52.199+0.723	19 24 59.84	17 25 17.90	3.31	2.8	2;5	1.01	58 760	14
G52.663−1.092	19 32 36.07	16 57 38.40	65.22	2.6	64;67	1.24	58 870	11,14
G59.783+0.065	19 43 11.25	23 44 03.30	26.96	4.3	26;29	1.97	58 870	9,11
G79.736+0.991	20 30 50.67	41 02 27.60	−5.59	4.7	−7;−4	3.04	58 713	11
G85.410+0.003 [(a)]	20 54 13.68	44 54 07.60	−29.74	5.7	−33;−27	5.63	58 870	
G107.298+5.639 [(a)]	22 21 22.50	63 51 13.00	−7.34	25.1	−9;−6	8.44	58 677	
G109.871+2.114	22 56 17.90	62 01 49.65	−4.07	44.5	−5;−1	10.99	58 902	4,5,11
G111.542+0.777	23 13 45.36	61 28 10.55	−61.30	36.7	−55;−62	49.46	58 702	1,4,5,11
G133.947+1.064	02 27 03.82	61 52 25.40	−44.54	601.3	−47;−41	1334.22	58 770	1,4,5,11
G183.348−0.575 [(a)]	05 51 10.94	25 46 17.24	−4.87	2.6	−6;−4	1.15	58 703	
G188.946+0.886	06 08 53.34	21 38 29.16	10.84	268.0	8;12	196.28	58 892	3,4,5,6,9,11,13
G192.600−0.048	06 12 54.02	17 59 23.32	5.84	25.9	3;7	17.40	58 723	12,13

Notes. Column 1 presents the methanol maser galactic coordinates, Cols. 2–3 give equatorial coordinates of the 6.7 GHz methanol masers (Breen et al. 2016; Szymczak et al. 2012; Hu et al. 2016). Columns 4–8 present characteristics of the obtained spectra; the velocity of the strongest peak relative to the local standard of rest ($V_{\rm peak}$), peak flux density ($S_{\rm peak}$), velocity range of the maser emission (ΔV), integrated flux density ($S_{\rm int}$), and epoch of observation, respectively. For G107.298+5.639 the epoch of the strongest flare was selected. The last column list the references to previous detections. [(a)]Newly detected 12.2 GHz maser.

References. (1) Batrla et al. (1987); (2) Norris et al. (1987); (3) Kemball et al. (1988); (4) Koo et al. (1988); (5) Catarzi et al. (1993); (6) Caswell et al. (1993); (7) MacLeod et al. (1993); (8) Gaylard et al. (1994); (9) Caswell et al. (1995a); (10) Moscadelli & Catarzi (1996); (11) Błaszkiewicz & Kus (2004); (12) Breen et al. (2010); (13) Breen et al. (2012a); (14) Breen et al. (2016).

values of 12.2 GHz flares (1.8−4.5 d) vary from cycle to cycle much more than those of 6.7 GHz flares (4.4−5.8 d), suggesting a greater variability of the 12.2 GHz emission.

There is a systematic delay between 6.7 and 12.2 GHz flare peaks (Table 2) for each of the three cycles (lower panel in Fig. 2). The average delay obtained from the results of the three fits is 0.9±0.3 d. The VLBI maps indicate that the 6.7 GHz emission near −7.35 km s^{-1} comes from clouds located ∼150 au from the putative position of the central star (Olech et al. 2020). Thus, if the 6.7 and 12.2 GHz maser coexist, then the observed delay cannot be explained by a simple geometrical effect. We may speculate that the actual size of the region conducive for 6.7 GHz maser emission is more extended than it would be for 12.2 GHz maser emission and both maser regions may not coincide precisely. Further interferometric studies are needed to verify this possibility.

The lower part of Fig. 2 shows variations in the 6.7 to 12.2 GHz flux density ratio ($R_{6/12}$) over the cycles. There are significant differences in the temporal behaviour of $R_{6/12}$ over the flare profile from cycle to cycle. For the best sampled observations of the second cycle, with a peak around MJD 58 714, $R_{6/12}$ falls from 22 at flare onset to 10.4 at flare maximum and then increases to 32 as the flare decays. The average value of $R_{6/12}$ for the three cycles around the flare peaks is 8.1 which is very close to the median ratio reported in Caswell et al. (1995b) and Breen et al. (2014).

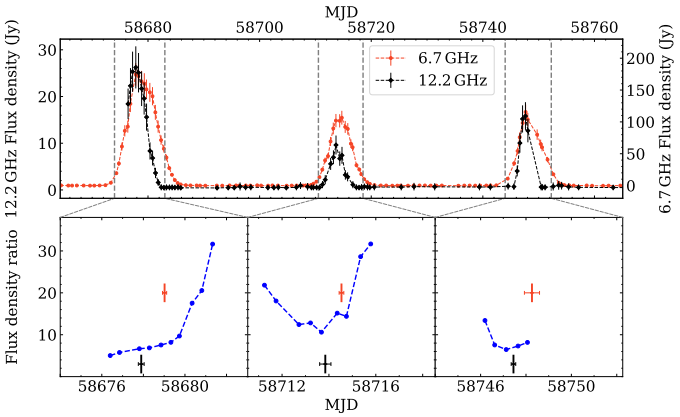

Fig. 2. Light curves of the −7.4 km s^{-1} methanol maser feature at 12.2 (black) and 6.7 GHz (red) for G107.298+5.639 (*upper panel*). Temporal changes in the 6.7–12.2 GHz flux density ratio are plotted (blue) (*lower panel*). The thick vertical error bars denote the flare maxima at 12.2 (black) and 6.7 GHz (red) calculated as the average value of the peak times obtained with the use of three methods (Table 2), whereas the thin horizontal error bars mark the corresponding standard errors.

Table 2. Flare parameters retrieved from the three model fitting.

6.7 GHz			12.2 GHz		
Epoch (MJD)	*FWHM* (d)	S_p (Jy)	Epoch (MJD)	*FWHM* (d)	S_p (Jy)
Asymmetric power function					
58 678.80	5.76	175.5	58 677.85	4.46	26.0
58 714.46	4.41	107.6	58 713.82	2.90	8.4
58 748.20	4.52	112.0	58 747.43	1.93	16.5
Gaussian function					
58 679.25	5.18	191.4	58 677.93	3.81	27.2
58 714.63	4.37	109.5	58 713.82	2.85	8.4
58 748.59	4.53	113.4	58 747.46	1.81	16.9
2-nd order polynomial					
58 679.02	–	162.6	58 677.91	–	25.6
58 714.51	–	99.5	58 713.90	–	8.1
58 748.00	–	110.2	58 747.45	–	16.2

Notes. The points with the flux density greater than 50% of the peak value were used for the parabola fitting. S_p is the fitted flux density at flare peak.

4. Comments on previously known sources

In this section, we provide commentary on our observational data with the aim of providing useful information on the 6.7 to 12.2 GHz flux density ratio. Taken together with results of previous surveys given in Table 1, it is possible to estimate the degree and timescale of variability.

G30.225−0.180. The 12.2 GHz maser spectrum detected in September and December 1992 by Caswell et al. (1995a) was composed of two features at $V_{12.2}$ = 112.8 and 113.6 km s^{-1}, with a peak flux density $S_{12.2}$ ∼ 2.8 and 1.2 Jy, respectively. Our observations reveal the spectrum of different shape with a peak flux density of $S_{12.2}$ = 6.7 Jy at $V_{12.2}$ = 113.3 km s^{-1}. There was no emission found, with a 5σ sensitivity level of 1.8 Jy, in March 2010 (Breen et al. 2016). This implies significant variability on timescales of 9–27 yr. The emission at a velocity lower than 111 km s^{-1} (Fig. A.1) comes from another source, namely, G30.198−0.169 (Caswell et al. 1995a; Breen et al. 2016), which was detected in the beam sidelobe.

G32.744−0.075. A comparison of our observations with those in the literature suggests that the overall spectral profile of the 12.2 GHz maser emission has been unchanged over more than 40 yr (Caswell et al. 1993). The peak flux density of individual features differ by ≤40% on timescales of 9–27 yr (Caswell et al. 1993, 1995a; Breen et al. 2016), suggesting only modest variability.

G33.641−0.228. The brightest features in our spectrum have similar velocities to those reported in Breen et al. (2016), but their flux densities differ by a factor of 0.3–2.3. Furthermore, the emission at $V_{12.2}$ = 58.8 km s^{-1} decreased by an order of magnitude as compared to that observed in 2002 by Błaszkiewicz & Kus (2004). This implies significant variability on timescales of 9–18 yr. The source also shows a variety of variability patterns in the 6.7 GHz methanol maser emission from short (2–5 d) flares, with a seven-fold rise within 24 hr (Fujisawa et al. 2012, 2014), up to quasi-periodic (>500 d) variations of low amplitude (Olech et al. 2019).

G35.132−0.744. The strongest feature at $V_{12.2}$ = 31.2 km s^{-1} that was observed by Breen et al. (2016) increased by a factor of 2, whereas the feature at $V_{12.2}$ = 29.7 km s^{-1} increased by one order of magnitude. This implies strong variability on a timescale of 9 yr.

G35.197−0.743. The spectrum observed in April 1988 (Caswell et al. 1993) is complex, with a prominent feature at $V_{12.2}$ = 30.5 km s^{-1}, with a peak flux of $S_{12.2}$ = 44 Jy. The intensity of this feature decreased by ∼30%, while the emission peak at $V_{12.2}$ = 28.5 km s^{-1} increased by the same amount after ∼4.5 yr (Caswell et al. 1995a). MacLeod et al. (1993) and Błaszkiewicz & Kus (2004) reported the spectrum similar to that observed in December 1992 by Caswell et al. (1995a), while the Breen et al. (2016) spectrum is similar to that presented in Caswell et al. (1993). Thus, from the data reported in the literature we infer a variability of 30–40% on a timescale of 4–20 yr. Our survey suggests that this level of variability remains on timescale of ≥30 yr for the redshifted emission (30.5 km s^{-1}) but the feature at $V_{12.2}$ = 28.2 km s^{-1} increased by a factor of 4 as compared to the spectrum from Breen et al. (2016).

G35.200−1.736. Norris et al. (1987) reported the spectrum, consisting of two features at $V_{12.2}$ = 41.5 and 45.0 km s^{-1} with peak flux densities of $S_{12.2}$ = 100 and 146 Jy, respectively. A similar spectrum was seen after 1–5 yr with slight (≤15%) decreases of peak intensity (Caswell et al. 1993, 1995a; Catarzi et al. 1993). Observations in 2002 (Błaszkiewicz & Kus 2004) and 2010 (Breen et al. 2016) displayed an ongoing complex spectrum with two prominent features but with the flux density of the strongest feature at $V_{12.2}$ = 45.0 km s^{-1} decreasing to $S_{12.2}$ = ∼80 Jy in 2002 and $S_{12.2}$ = 46 Jy in 2010. We report only a single feature with a peak of $S_{12.2}$ = 12 Jy at $V_{12.2}$ = 45.2 km s^{-1}. We conclude that the 12.2 GHz line intensity declined by an order of magnitude within 32 yr.

G37.430+1.518. Our spectrum, with a single feature of $S_{12.2}$ = 74 Jy at $V_{12.2}$ = 41.3 km s^{-1}, is very similar to that reported by Błaszkiewicz & Kus (2004) and Breen et al. (2016), implying a variability lower than 20% on a timescale of 17 yr. The

emission observed 26 yr ago (Gaylard et al. 1994) was a factor of 6 weaker, suggesting significant variability on longer timescales.

G40.282−0.219. The three-feature spectrum is similar to that observed nine years ago (Breen et al. 2016) but the flux density of the primary feature at $V_{12.2}$ = 74.3 km s^{-1} decreased by ∼50%.

G42.034+0.190. We detected a weak and complex 12.2 GHz spectrum of similar shape to that shown in Breen et al. (2016). In general, the intensity of features increased by a factor of 1.8–4.5 after nine years.

G43.149+0.013. The 12.2 GHz spectrum consisted of a single feature at $V_{12.2}$ = 13.6 km s^{-1}. Its intensity declined by 35% over 26 yr (Caswell et al. 1995a; Breen et al. 2016).

G43.890−0.784. Little variability is visible in the two features at $V_{12.2}$ = 47.4 and 51.8 km s^{-1} when compared to spectra from 2002 (Błaszkiewicz & Kus 2004) an 2010 (Breen et al. 2016). From our observations, it can be seen that the emission at $V_{12.2}$ = 51.8 km s^{-1} decreased by a factor of 2. There was no emission detected at $V_{12.2}$ = 47.7 km s^{-1}, whereas a new feature appeared at $V_{12.2}$ = 45.3 km s^{-1}, indicating significant variability.

G49.043−1.079. Nine years ago, this 12.2 GHz source had a complex spectra (Breen et al. 2016). In our observations, the strongest feature they detected ($S_{12.2}$ = 7.1 Jy at $V_{12.2}$ = 37.4 km s^{-1}) is now only ∼1 Jy. This suggests strong variability on this timescale.

G49.416+0.326. The spectrum is similar to that presented in Breen et al. (2016), with little variability above the noise level.

G49.490−0.388. The spectrum is composed of the emission from G49.489−0.369 and G49.490−0.388 as part of the W51 complex. Batrla et al. (1987) discovered a single feature, with a peak flux density of $S_{12.2}$ = 8 Jy at $V_{12.2}$ ∼ 56 km s^{-1}, and a broad absorption feature (from 60 to 75 km s^{-1}). Catarzi et al. (1993) observed a similar spectrum with a peak flux density of $S_{12.2}$ = 20 Jy without absorption. Caswell et al. (1993, 1995a) also reported one feature with the peak flux density of $S_{12.2}$ = 14 and 21 Jy, respectively with barely visible absorption. A simple spectrum with a single feature at $V_{12.2}$ = 56.2 km s^{-1} with $S_{12.2}$ = 13.8 Jy was also observed by Błaszkiewicz & Kus (2004). The flux density of this feature dropped to 4.5–5.5 Jy (in 2008 and 2010, Breen et al. 2016) and increased to ∼10 Jy during our observations. This suggests that the emission towards G49.490−0.388 shows significant and complicated temporal changes. Features at velocity >56.6 km s^{-1} were also visible only in 2010 (Breen et al. 2016) that might suggest variability of G49.489−0.369. It is difficult, given our beam size, to distinguish unequivocally which spectral feature comes from which object; hence, the velocity ranges marked in Fig. A.1 are taken from Breen et al. (2016).

G49.599−0.249. The spectrum is almost the same as the one seen in Breen et al. (2016), with the exception of the 63.0 km s^{-1} feature, which decreased by a factor of 2 after 9 yr.

G59.783+0.065. The feature at $V_{12.2}$ = 27.1 km s^{-1} declined from $S_{12.2}$ = 15.8 Jy in 1992 (Caswell et al. 1995a) to $S_{12.2}$ = 9.2 Jy in 2002 (Błaszkiewicz & Kus 2004) and $S_{12.2}$ = 4.3 Jy during our observations. The second feature at $V_{12.2}$ = 17.0 km s^{-1}, with a peak flux of $S_{12.2}$ = 4 Jy (Caswell et al. 1995a) increased by ∼50% (Błaszkiewicz & Kus 2004) and decreased below our sensitivity limit of ∼1 Jy.

G109.871+2.114. Observations made in 1990 (Catarzi et al. 1993), with a peak flux density of $S_{12.2}$ = 128.8 Jy at $V_{12.2}$ = −4.15 km s^{-1}, found a similar spectral profile shape to that seen in 1987 (Koo et al. 1988), but with flux density that was a factor of ∼2 lower. Błaszkiewicz & Kus (2004) revealed a similar profile but with peak flux densities that were a factor of 3 lower than Koo et al. (1988). We detected a complex spectrum with the emission from $V_{12.2}$ = −5 to −1 km s^{-1} and a peak flux density of $S_{12.2}$ = 45 Jy at $V_{12.2}$ = −4.1 km s^{-1}. Thus, the source is significantly variable, namely, by a factor of 7 on a timescale of ∼30 yr.

G111.542+0.777. Batrla et al. (1987) discovered a double peaked spectrum, the brightest feature at $V_{12.2}$ = −56.3 km s^{-1}, with $S_{12.2}$ ∼200 Jy remained stable within 15% over 1–3 yr (Koo et al. 1988; Catarzi et al. 1993). The spectral shape was found to be unchanged in 2002 (Błaszkiewicz & Kus 2004) but the peak flux density decreased by a factor of 2. Here, we present a very different spectrum with several blended features from −62 to −55 km s^{-1}. The feature at $V_{12.2}$ = −56.3 km s^{-1} dimmed by a factor of 20 compared to that reported by Batrla et al. (1987), whereas the feature near $V_{12.2}$ = −61.5 km s^{-1} increased by a factor of less than 2. This suggests strong variability on a timescale of ≥20 yr.

G188.946+0.886. The flux density of the strongest feature at $V_{12.2}$ = 10.4 km s^{-1} increased by ∼30% between 1987 and 1992 (Koo et al. 1988; Kemball et al. 1988; Caswell et al. 1993, 1995a; Catarzi et al. 1993). The profile of the spectrum significantly transformed in 2008 (Breen et al. 2012a) but the intensity remained unchanged within 10%. We found spectra similar to those reported in Breen et al. (2012a), and the peak flux of feature at $V_{12.2}$ = 10.8 km s^{-1} increased by ∼15%. More information on the variability of this object is provided in Sect. 2.

G192.600−0.048. A faint (0.5–0.6 Jy) feature at $V_{12.2}$ = 3.6 km s^{-1} was detected in June and December 2008 (Breen et al. 2012a). Our observations revealed a complex spectrum with the strongest feature of $S_{12.2}$ = 26 Jy at $V_{12.2}$ = 5.8 km s^{-1}. Significant change in the spectral profile and intensity is likely related to a significant outburst of a 6.7 GHz maser that occurred in mid-2015 (Moscadelli et al. 2017; Szymczak et al. 2018).

There is a group of 12.2 GHz masers that have gone undetected in the present survey (Table A.1) and 13 out of those 17 masers were observed with a 5σ sensitivity of 0.7–4.2 Jy, that is, lower than the peak flux densities at the time of their detection from the literature. We failed to detect, with 5σ sensitivity of 0.6–0.9 Jy, the following objects: G42.698−0.147, G45.467+0.053, G94.602−1.796, and G196.454−1.677, with a peak flux density of 1.2–12.3 Jy in earlier observations (Caswell et al. 1995a; Błaszkiewicz & Kus 2004; Breen et al. 2012a, 2016). These four sources may be variable on timescales smaller than 9–28 yr.

5. Discussion

5.1. Detection rate

The present observations of our sample of 153 6.7 GHz masers resulted in the detection of 36 12.2 GHz methanol maser sources, corresponding to a ∼24% detection rate. This is about a factor of 2 lower than the overall detection rate of 43% in the Galactic longitude range of 290° ≤ l ≤ 60° (Breen et al. 2016). We compared our detection rate with the rates from Breen et al. (2016) as a function of 10° longitude bins. For the 30°−40°, 40°−50°, and

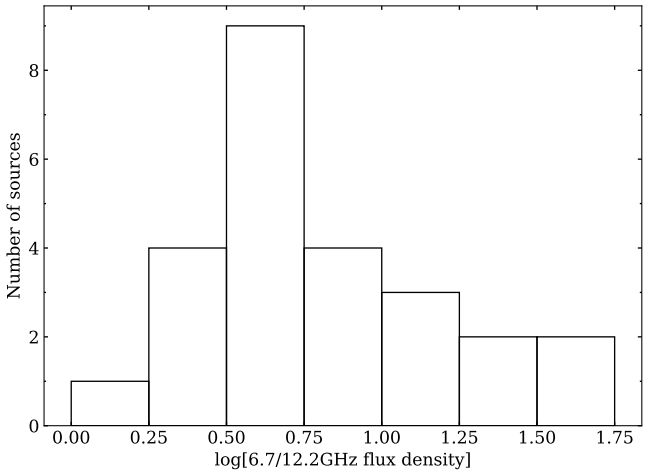

Fig. 3. Histogram of the 6.7–12.2 GHz peak flux density ratio.

50°−60° longitude bins, our detection rates are lower by 20, 9, and 2%, respectively, than those reported in Breen et al. (2016). This confirms a significant lowering of our sensitivity for low declination sources as shown in Table A.1. The reason for this is a degradation of sensitivity due to interference from geostationary satellites or imperfect removal of some corrupted scans during the edition of spectra. The detection rate in the range of $70° \leq l \leq 90°$ decreases to ∼16% and shows a statistically significant difference from that for the neighbouring range of 50°−60° (23.5%).

5.2. Flux density ratio

Our survey indicates that the flux density of individual features and integrated flux density of the 6.7 GHz maser sources are all greater than those of their 12.2 GHz counterparts. This is consistent with conclusions inferred from more comprehensive statistical analysis based on a large sample (Breen et al. 2011). In the following, we confine discussion to the flux density ratio $R_{6/12}$ for the spectral features with the same velocity in both transitions contemporaneously observed in order to exclude the possible effect of variability. There is strong observational evidence of spatial coincidence of the 6.7 and 12.2 GHz masers to within a few milliarcseconds, especially when the spectral profiles of both transitions are similar (Menten et al. 1992; Norris et al. 1993; Minier et al. 2000; Moscadelli et al. 2002). Thus, it is suggestive that the flux density comparison can be meaningful in the absence of high angular resolution maps. We found 70% of the detected 12.2 GHz methanol maser peaks are coincident in velocity with the 6.7 GHz maser peak.

For the 6.7 and 12.2 GHz spectra of nine sources taken within 7 days of each other, we performed Gaussian function fits to obtain the velocity and flux density of feature peaks. For all features with the same peak velocity (±0.1 km s^{-1}) at both transitions, the flux density ratio, $R_{6/12}$, was determined (Table 3). The range of $R_{6/12}$ is 1.5 to 50.9, with a median value of 5.1 (Fig. 3). Our median is comparable to that determined by Caswell et al. (1995b). The analysis by Breen et al. (2011) of the statistical properties of 580 southern sources found a median peak-to-peak ratio of 4.3. Although their samples are more numerous, with little overlap with ours, the median ratios are similar. This suggests that each of these samples come from a similar population of HMYSOs.

There is a significant dispersion of $R_{6/12}$ for spectral features of some sources (e.g. G111.524+0.777, Table 3). Furthermore, our observations of G107 reveal that around the flare maxima, $R_{6/12}$ varies by up to 50% between two consecutive cycles. In addition, the temporal behaviour of $R_{6/12}$ is poorly repeated from cycle to cycle, even though a general trend remains, that is, the ratio reaches a minimum around the flare peak and is larger at the onset and final stages of the flare profile. This could be caused by variations in the physical conditions along the maser path length of 10^{16} cm (Moscadelli et al. 2002) for individual features on different timescales.

In G107, the maser intensity varies with a period of 34.4 days, perhaps due to changes of infrared emission (Olech et al. 2020); it is difficult to identify processes that can significantly change the gas density, molecule abundance, and kinetic temperature in the maser regions on such a short timescale. Since the heating and cooling times of dust grains are less than a few minutes and one day, respectively, for the optically thick case (van der Walt et al. 2009; Johnstone et al. 2013), rapid changes in the maser intensity may be related to variations in the dust temperature (T_d). Timescales of gas heating and cooling are 2–3 orders of magnitude greater than those of dust grains (e.g. Johnstone et al. 2013); thus, the gas temperature variation can affect the maser emission in G107 on timescales of several months.

Numerical models of infrared pumping indicate that the 6.7 and 12.2 GHz methanol masers over a wide range of the gas densities and kinetic temperatures (Cragg et al. 2002, 2005), but there is a narrow range of dust temperature, T_d, for which the flux ratio varies quite rapidly (Cragg et al. 2005, their Fig. 2). When the dust temperature increases from ∼130 to ∼170 K, $R_{6/12}$ decreases by a factor of 2 and vice versa. Therefore, the variations in T_d qualitatively explain the observed change in the flux ratio during the flare of G107. However, it should be noted that the temporal behaviour of $R_{6/12}$ varies considerably from cycle to cycle, which is possibly the result of small variations in the physical conditions along the maser path and the degree of saturation (e.g. Breen et al. 2012b). High-cadence monitoring observations combined with a high angular resolution are required to resolve this discrepancy.

5.3. Variability

There are 24 detected sources in our sample that are in common with those observed by Breen et al. (2016) at 12.2 GHz and Breen et al. (2015) at 6.7 GHz, providing an opportunity to study variations on a timescale of ∼10 yr. Seven objects with spectra comprised of multiple sources were not considered. In Fig. 4, we present the relative changes in the integrated flux density (S_{int}) between the two methanol maser transitions. In Fig. 5, the same analysis is presented, but for peak flux densities (Table A.2 shows exact values). Among 17 sources detected in two epochs, only two show S_{int} variability of more than 50% in both transitions, these are: G35.200−1.736 and G49.043−1.079. The first object dimmed by a factor of 14.5 and 8.2 at 12.2 GHz and 6.7 GHz, respectively. The second object weakened by a factor of 12.7 at 12.2 GHz but only a factor of 2.3 at 6.7 GHz. G36.115+0.552 decreased by a factor of 2.2 at both lines. Two other objects (G45.804−0.356 and G49.265+0.311) varied by slightly more than 50% at 12.2 GHz but did not show significant variability at 6.7 GHz. For the subsample of 17 sources, the median value of relative changes in S_{int} is 1.19 and 1.33 for the 6.7 and 12.2 GHz lines, respectively. This general trend of a larger level of variability at 12.2 GHz than that at 6.7 GHz is more pronounced for the entire sample (Figs. 4 and 5) and is consistent with the standard model of methanol masers (Cragg et al. 2002, 2005). They demonstrated that both masers operate in a wide range of gas

Table 3. 6.7–12.2 GHz flux density ratio ($R_{6/12}$) for the Gaussian fitted features for all the sources contemporaneously observed at both maser transitions.

Source (l b) (° °)	V (km s^{-1})	$S_{6.7}$ (Jy)	$S_{12.2}$ (Jy)	$R_{6/12}$
G35.200−1.736	44.62	34.3(0.4)	2.1(0.4)	16.0(2.4)
	45.21	17.8(0.2)	11.9(0.3)	1.5(0.1)
G49.416+0.326	−10.13	2.3(0.1)	0.8(0.2)	2.7(0.6)
G49.599−0.249	65.51	10.5(2.0)	3.0(0.6)	3.5(1.0)
	62.93	15.9(0.1)	3.7(0.1)	4.3(0.1)
	64.14	15.4(0.3)	4.5(0.2)	3.4(0.2)
	64.61	16.6(2.3)	4.2(0.2)	3.9(0.6)
	65.34	15.3(4.0)	3.0(0.6)	5.1(1.7)
G85.410+0.003	−31.55	9.9(3.5)	1.2(0.2)	8.4(3.1)
	−28.65	5.7(0.2)	2.5(0.2)	2.3(0.2)
G107.29+5.64	−7.35	170.2(1.0)	25.8(0.4)	6.6(0.2)
G109.871+2.114	−3.72	125.7(22.0)	3.8(0.2)	32.7(5.9)
	−1.80	245.8(1.4)	4.8(0.2)	50.9(1.6)
G111.542+0.777	−61.33	154.9(0.6)	36.7(0.4)	4.2(0.1)
	−60.77	118.7(0.5)	14.6(0.3)	8.1(0.2)
	−58.08	230.2(3.2)	12.0(0.3)	19.2(0.6)
	−57.60	151.2(3.5)	7.0(0.8)	21.6(2.3)
	−57.22	91.7(6.0)	6.6(0.5)	13.9(1.3)
	−56.75	93.9(0.7)	13.4(0.3)	7.0(0.2)
G188.946+0.886	10.43	400.4(3.9)	109.2(3.2)	3.7(0.2)
	10.86	858.2(4.7)	269.6(1.8)	3.2(0.1)
G192.600−0.048	3.93	8.8(0.4)	4.0(0.2)	2.2(0.2)
	4.79	13.5(0.4)	5.3(0.3)	2.5(0.2)
	5.46	55.6(1.4)	5.2(0.5)	10.7(1.0)
	5.83	139.7(3.3)	25.5(0.5)	5.5(0.2)

Notes. The fitted peak velocity (V), peak flux density at 6.7 ($S_{6.7}$) and at 12.2 GHz ($S_{12.2}$) are listed. The values in brackets correspond to uncertainty, derived from covariance matrix of the least-squares fit method.

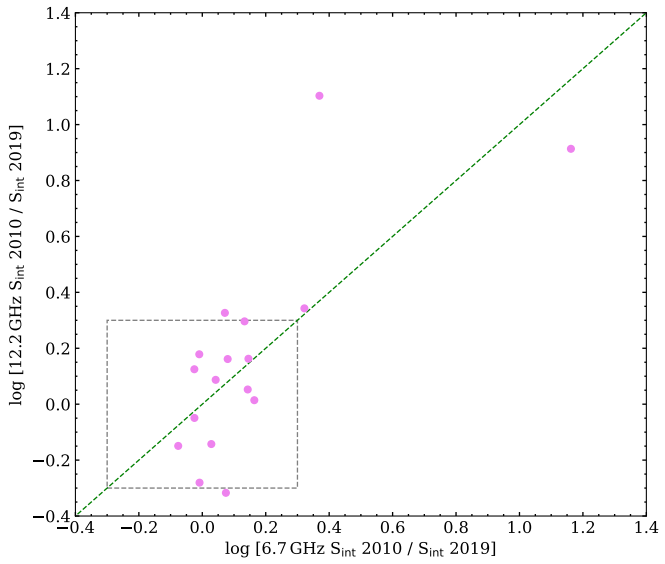

Fig. 4. Relative change in the integrated flux density, S_{int} at 6.7 and 12.2 GHz between 2010 (Breen et al. 2015, 2016) and 2019 (this survey). The square marks 50% level of variability.

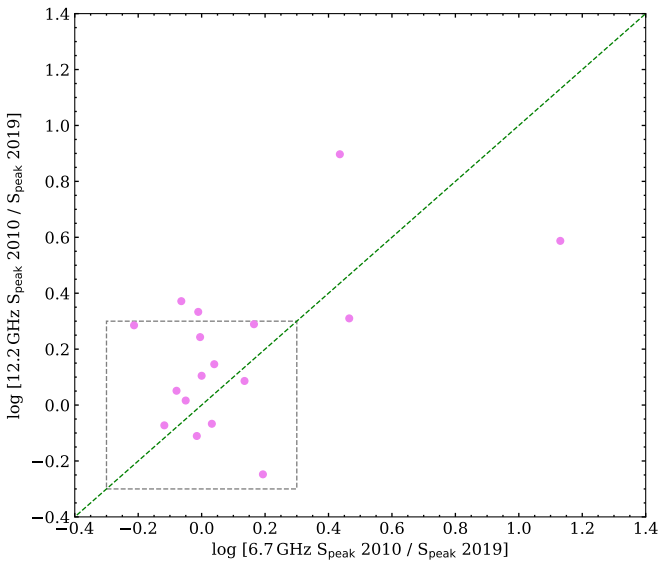

Fig. 5. Relative change in the peak flux density, S_{peak} at 6.7 and 12.2 GHz between 2010 (Breen et al. 2015, 2016) and 2019 (this survey). The square marks 50% level of variability. Data used to create this graph is presented in Table A.2.

density (10^4–10^8 cm^{-3}), gas temperature (30–200 K), and dust temperature (130–350 K) but we can see that the slopes of the intensity versus these parameters are more flat at 6.7 GHz than at 12.2 GHz (Cragg et al. 2005). Thus, long-term (9–10 yr) changes of the parameters may lead to higher variability in the 12.2 GHz line. Since high angular resolution interferometric studies have revealed that the 6.7 and 12.2 GHz emission is spatially coincident, the effect of turbulence or changes in velocity coherence

should be the same for both transitions. Table A.2 also presents comparison of the number of the features visible in 12.2 GHz spectra among the literature data (Breen et al. 2016) and this survey. Many of the features generally remain unchanged (±1 feature), with the exception of G35.200−1.736, for which a significant decrease of luminosity is observed in both 6.7 and 12.2 GHz lines.

6. Conclusions

We report that we detected 36 12.2 GHz methanol masers in our sample of 153, of which 4 are new detections, corresponding to detection rate of 24%.

Values of the 6.7–12.2 GHz flux density ratio for spectral features at the same velocity, when both transitions are observed contemporaneously, are within the range from 1.5 to 51. The median value of 5.1 is similar to that reported for other large samples of HYMSOs. This ratio in the periodic source G107.298+5.639 is smallest when the flare reaches its maximum, but it varies considerably from cycle to cycle. It decreases from its maximum value at the onset through its minimum at the peak of the flare and then increases during the decay phase of the flare. This temporal behaviour appears to be consistent with the standard model of methanol masers when the dust temperature varies in the narrow range of 130–170 K.

A minority (14%) of the objects that we observed show strong (>50%) variability at 6.7 GHz over a timescale of 9–10 yr, but at 12.2 GHz, nearly half of the observed sources experienced strong variability. These results appear to be compatible with maser model predictions.

Acknowledgements. We thank the staff of the 32 m telescope for assistance with the observations. We also thank the referee for the careful reading of the manuscript and recommendations. The research has made use of the SIMBAD data base, operated at CDS (Strasbourg, France), as well as NASA's Astrophysics Data System Bibliographic Services. The 32 m telescope is operated by the Institute of Astronomy, Nicolaus Copernicus University and supported by the Polish Ministry of Science and Higher Education SpUB grant.

References

Barrett, A. H., Schwartz, P. R., & Waters, J. W. 1971, ApJ, 168, L101
Batrla, W., Matthews, H. E., Menten, K. M., & Walmsley, C. M. 1987, Nature, 326, 49
Błaszkiewicz, L., & Kus, A. J. 2004, A&A, 413, 233
Breen, S. L., Ellingsen, S. P., Caswell, J. L., & Lewis, B. E. 2010, MNRAS, 401, 2219
Breen, S. L., Ellingsen, S. P., Caswell, J. L., et al. 2011, ApJ, 733, 80
Breen, S. L., Ellingsen, S. P., Caswell, J. L., et al. 2012a, MNRAS, 426, 2189
Breen, S. L., Ellingsen, S. P., Caswell, J. L., et al. 2012b, MNRAS, 421, 1703
Breen, S. L., Ellingsen, S. P., Caswell, J. L., et al. 2014, MNRAS, 438, 3368
Breen, S. L., Fuller, G. A., Caswell, J. L., et al. 2015, MNRAS, 450, 4109
Breen, S. L., Ellingsen, S. P., Caswell, J. L., et al. 2016, MNRAS, 459, 4066
Breen, S. L., Sobolev, A. M., Kaczmarek, J. F., et al. 2019, ApJ, 876, L25
Brogan, C. L., Hunter, T. R., Towner, A. P. M., et al. 2019, ApJ, 881, L39
Caswell, J. L., Gardner, F. F., Norris, R. P., et al. 1993, MNRAS, 260, 425
Caswell, J. L., Vaile, R. A., Ellingsen, S. P., & Norris, R. P. 1995a, MNRAS, 274, 1126
Caswell, J. L., Vaile, R. A., Ellingsen, S. P., Whiteoak, J. B., & Norris, R. P. 1995b, MNRAS, 272, 96
Catarzi, M., Moscadelli, L., & Panella, D. 1993, A&AS, 98, 127
Cragg, D. M., Sobolev, A. M., & Godfrey, P. D. 2002, MNRAS, 331, 521
Cragg, D. M., Sobolev, A. M., & Godfrey, P. D. 2005, MNRAS, 360, 533
David, P., Etoka, S., & Le Squeren, A. M. 1996, A&AS, 115, 387
Ellingsen, S. P., von Bibra, M. L., McCulloch, P. M., et al. 1996, MNRAS, 280, 378
Fujisawa, K., Sugiyama, K., Aoki, N., et al. 2012, PASJ, 64, 17
Fujisawa, K., Aoki, N., Nagadomi, Y., et al. 2014, PASJ, 66, 109
Gaylard, M. J., MacLeod, G. C., & van der Walt, D. J. 1994, MNRAS, 269, 257
Goedhart, S., Maswanganye, J. P., Gaylard, M. J., & van der Walt, D. J. 2014, MNRAS, 437, 1808
Green, J. A., Caswell, J. L., Fuller, G. A., et al. 2010, MNRAS, 409, 913
Hu, B., Menten, K. M., Wu, Y., et al. 2016, ApJ, 833, 18
Johnstone, D., Hendricks, B., Herczeg, G. J., & Bruderer, S. 2013, ApJ, 765, 133
Kemball, A. J., Gaylard, M. J., & Nicolson, G. D. 1988, ApJ, 331, L37
Koo, B.-C., Williams, D. R. D., Heiles, C., & Backer, D. C. 1988, ApJ, 326, 931
MacLeod, G. C., Gaylard, M. J., & Kemball, A. J. 1993, MNRAS, 262, 343
MacLeod, G. C., Sugiyama, K., Hunter, T. R., et al. 2019, MNRAS, 489, 3981
McCutcheon, W. H., Wellington, K. J., Norris, R. P., et al. 1988, ApJ, 333, L79
Menten, K. M. 1991, ApJ, 380, L75
Menten, K. M., Reid, M. J., Pratap, P., Moran, J. M., & Wilson, T. L. 1992, ApJ, 401, L39
Minier, V., Booth, R. S., & Conway, J. E. 2000, A&A, 362, 1093
Moscadelli, L., & Catarzi, M. 1996, A&AS, 116, 211
Moscadelli, L., Menten, K. M., Walmsley, C. M., & Reid, M. J. 2002, ApJ, 564, 813
Moscadelli, L., Sanna, A., Goddi, C., et al. 2017, A&A, 600, L8
Müller, H. S. P., Menten, K. M., & Mäder, H. 2004, A&A, 428, 1019
Norris, R. P., Caswell, J. L., Gardner, F. F., & Wellington, K. J. 1987, ApJ, 321, L159
Norris, R. P., Whiteoak, J. B., Caswell, J. L., Wieringa, M. H., & Gough, R. G. 1993, ApJ, 412, 222
Olech, M., Szymczak, M., Wolak, P., Sarniak, R., & Bartkiewicz, A. 2019, MNRAS, 486, 1236
Olech, M., Szymczak, M., Wolak, P., Gérard, E., & Bartkiewicz, A. 2020, A&A, 634, A41
Ott, M., Witzel, A., Quirrenbach, A., et al. 1994, A&A, 284, 331
Pandian, J. D., Goldsmith, P. F., & Deshpande, A. A. 2007, ApJ, 656, 255
Pazderski, E. 2018, Balt. URSI Symp., 33
Szymczak, M., Wolak, P., Bartkiewicz, A., & van Langevelde, H. J. 2011, A&A, 531, L3
Szymczak, M., Wolak, P., Bartkiewicz, A., & Borkowski, K. M. 2012, Astron. Nachr., 333, 634
Szymczak, M., Olech, M., Wolak, P., Bartkiewicz, A., & Gawroński, M. 2016, MNRAS, 459, L56
Szymczak, M., Olech, M., Sarniak, R., Wolak, P., & Bartkiewicz, A. 2018, MNRAS, 474, 219
van der Walt, D. J., Goedhart, S., & Gaylard, M. J. 2009, MNRAS, 398, 961

Appendix A: Additional material

Table A.1. Targets towards which no 12.2 GHz emission was detected in the survey.

Name (l b) (° °)	RA(J2000) (h m s)	Dec(J2000) (° ′ ″)	5σ Jy	Epoch MJD	References
G32.105−0.074	18 50 11.58	−00 46 12.32	3.00	58 827	
G33.133−0.092	18 52 07.82	00 08 12.80	3.80	58 812	1, 3, 4
G33.199+0.001	18 51 55.34	00 14 19.38	4.90	58 716	
G33.204−0.010	18 51 58.14	00 14 13.61	3.65	58 813	
G33.317−0.360	18 53 25.30	00 10 43.90	4.20	58 861	4
G33.393+0.010	18 52 14.62	00 24 52.90	3.00	58 866	4
G33.725−0.120	18 53 18.78	00 39 05.00	4.85	58 874	
G33.980−0.019	18 53 25.01	00 55 25.98	1.25	58 812	
G34.096+0.018	18 53 29.94	01 02 39.40	4.30	58 831	
G34.244+0.133	18 53 21.44	01 13 44.40	2.45	58 859	1, 3, 4
G34.257+0.153	18 53 18.63	01 14 57.40	6.80	58 866	1, 4
G34.267−0.210	18 54 37.25	01 05 33.70	2.75	58 856	
G34.396+0.222	18 53 19.08	01 24 13.80	4.15	58 860	
G34.411+0.235	18 53 17.99	01 25 25.26	3.00	58 713	
G34.751−0.093	18 55 05.22	01 34 36.26	1.95	58 860	
G34.757+0.025	18 54 40.74	01 38 06.40	2.30	58 864	
G34.822+0.352	18 53 37.84	01 50 33.00	3.20	58 875	
G35.025+0.350	18 54 00.66	02 01 19.30	2.35	58 725	3, 4
G35.226−0.354	18 56 53.15	01 52 46.89	1.75	58 706	
G35.247−0.237	18 56 30.38	01 57 08.88	3.55	58 819	
G35.397+0.025	18 55 50.78	02 12 19.10	1.85	58 868	
G35.417−0.284	18 56 59.02	02 04 55.65	2.00	58 868	
G35.457−0.179	18 56 40.98	02 09 57.16	2.75	58 875	
G35.588+0.060	18 56 04.22	02 23 28.30	5.00	58 880	
G35.793−0.175	18 57 16.89	02 27 57.91	1.70	58 882	4
G36.705+0.096	18 57 59.12	03 24 06.11	2.10	58 883	
G36.918+0.483	18 56 59.78	03 46 03.60	1.50	58 884	
G37.030−0.039	18 59 03.64	03 37 45.09	4.35	58 894	
G37.554+0.201	18 59 09.98	04 12 15.54	2.75	58 874	
G37.598+0.425	18 58 26.79	04 20 45.46	2.35	58 867	
G37.735−0.112	19 00 36.84	04 13 20.00	2.05	58 859	
G37.753−0.189	19 00 55.42	04 12 12.56	1.00	58 802	
G37.767−0.214	19 01 02.27	04 12 16.60	1.55	58 731	
G38.038−0.300	19 01 50.46	04 24 18.96	1.80	58 882	
G38.119−0.229	19 01 44.15	04 30 37.42	4.25	58 873	4
G38.203−0.067	19 01 18.73	04 39 34.29	1.95	58 856	
G38.255−0.200	19 01 52.95	04 38 39.47	1.15	58 762	
G38.258−0.073	19 01 26.25	04 42 19.90	1.80	58 867	
G38.565+0.538	18 59 49.13	05 15 28.90	1.05	58 810	
G38.598−0.212	19 02 33.46	04 56 36.40	1.75	58 857	
G38.653+0.088	19 01 35.24	05 07 47.36	1.80	58 857	
G38.916−0.353	19 03 38.65	05 09 42.49	1.40	58 818	
G39.388−0.141	19 03 45.31	05 40 42.68	1.05	58 712	
G40.623−0.138	19 06 01.63	06 46 36.50	0.90	58 714	
G40.934−0.041	19 06 15.37	07 05 54.49	1.80	58 819	
G41.121−0.107	19 06 50.24	07 14 01.49	1.70	58 867	
G41.123−0.220	19 07 14.85	07 11 00.69	1.40	58 860	
G41.156−0.201	19 07 14.37	07 13 18.10	0.90	58 713	
G41.226−0.197	19 07 21.37	07 17 08.17	0.85	58 704	
G41.347−0.136	19 07 21.84	07 25 17.27	1.80	58 856	4
G42.13+0.52	19 06 28.90	08 25 10.00	4.05	58 705	
G42.303−0.299	19 09 43.59	08 11 41.41	1.65	58 705	
G42.435−0.260	19 09 49.85	08 19 45.40	0.85	58 705	
G42.698−0.147	19 09 55.06	08 36 53.45	0.85	58 718	4
G43.038−0.453	19 11 38.98	08 46 30.71	1.05	58 722	

Notes. The source name in bold denotes previously detected masers.
References. (1) Caswell et al. (1995a); (2) Błaszkiewicz & Kus (2004) (3) Breen et al. (2010); (4) Breen et al. (2016).

Table A.1. continued.

Source (l b) (° °)	RA(J2000) (h m s)	Dec(J2000) (° ′ ″)	5σ Jy	Epoch MJD	References
G43.074−0.077	19 10 22.05	08 58 51.49	3.50	58 832	
G43.180−0.518	19 12 09.02	08 52 14.30	0.95	58 766	
G43.796−0.127	19 11 53.97	09 35 53.50	0.95	58 726	
G44.310+0.041	19 12 15.81	10 07 53.52	1.00	58 811	
G44.644−0.516	19 14 53.76	10 10 07.69	2.55	58 832	
G45.071+0.132	19 13 22.12	10 50 53.11	1.90	58 832	
G45.380−0.594	19 16 34.14	10 47 01.60	0.85	58 770	
G45.445+0.069	19 14 18.31	11 08 59.40	0.75	58 706	
G45.467+0.053	19 14 24.15	11 09 43.00	0.85	58 711	1, 4
G45.473+0.134	19 14 07.36	11 12 16.00	0.85	58 725	
G45.493+0.126	19 14 11.35	11 13 06.20	1.50	58 866	
G46.066+0.220	19 14 56.07	11 46 12.98	0.70	58 814	
G46.115+0.387	19 14 25.52	11 53 25.99	0.70	58 703	
G48.902−0.273	19 22 10.33	14 02 43.51	0.95	58 719	
G48.990−0.299	19 22 26.13	14 06 39.78	0.80	58 767	4
G49.417+0.324	19 20 59.82	14 46 49.10	0.75	58 726	
G49.470−0.371	19 23 37.90	14 29 59.30	0.95	58 810	3, 4
G49.617−0.360	19 23 52.81	14 38 03.30	1.65	58 832	
G50.315+0.676	19 21 27.47	15 44 18.60	0.75	58 802	
G50.779+0.152	19 24 17.41	15 54 01.60	1.75	58 862	4
G51.679+0.719	19 23 58.87	16 57 41.80	1.50	58 833	
G51.818+1.250	19 22 17.95	17 20 06.50	0.75	58 770	
G52.922+0.414	19 27 34.96	17 54 38.14	1.70	58 759	
G53.036+0.113	19 28 55.49	17 52 03.11	1.05	58 731	
G53.142+0.071	19 29 17.58	17 56 23.21	0.70	58 713	
G53.618+0.036	19 30 23.01	18 20 26.68	0.70	58 704	
G56.963−0.235	19 38 17.10	21 08 05.40	0.75	58 707	
G57.610+0.025	19 38 40.74	21 49 32.70	0.75	58 719	
G58.775+0.644	19 38 49.13	23 08 40.20	0.80	58 720	
G59.634−0.192	19 43 50.00	23 28 38.80	0.70	58 712	
G59.833+0.672	19 40 59.33	24 04 46.50	0.85	58 714	
G60.575+0.186	19 45 52.48	24 17 42.99	0.70	58 706	
G69.539+0.975	20 10 09.07	31 31 34.86	0.70	58 704	
G70.181+1.741	20 00 54.16	33 31 30.88	0.70	58 705	
G71.522+0.385	20 12 57.91	33 30 26.95	0.75	58 725	
G73.06+1.80	20 08 10.20	35 59 23.70	0.65	58 705	
G75.782+0.342	20 21 44.05	37 26 36.91	0.70	58 706	
G78.122+3.633	20 14 26.04	41 13 33.39	0.70	58 705	
G78.886+0.708	20 29 24.94	40 11 19.28	1.40	58 866	
G80.861+0.383	20 37 00.96	41 34 55.70	0.80	58 705	
G81.722+0.571	20 39 01.05	42 22 49.18	0.80	58 726	
G81.744+0.590	20 39 00.38	42 24 36.91	0.90	58 707	
G81.752+0.590	20 39 01.99	42 24 59.08	0.80	58 725	
G81.871+0.780	20 38 36.42	42 37 34.56	0.65	58 704	
G90.921+1.486	21 09 12.98	50 01 03.56	0.75	58 703	
G94.602−1.796	21 39 58.26	50 14 20.96	0.60	58 703	2
G97.52+3.17	21 32 13.00	55 52 56.00	0.85	58 707	
G98.035+1.446	21 43 01.43	54 56 17.75	0.75	58 712	
G108.184+5.519	22 28 51.40	64 13 41.31	0.65	58 706	
G108.766−0.986	22 58 51.18	58 45 14.37	0.95	58 702	
G111.255−0.769	23 16 10.33	59 55 28.43	0.80	58 702	
G121.298+0.659	00 36 47.35	63 29 02.16	0.75	58 712	
G123.066−6.309	00 52 24.19	56 33 43.17	0.70	58 712	
G136.845+1.167	02 49 33.59	60 48 27.95	0.85	58 705	
G173.482+2.446	05 39 13.05	35 45 51.29	0.75	58 705	
G173.70+2.89	05 41 37.40	35 48 49.00	0.70	58 726	
G174.201−0.071	05 30 48.01	33 47 54.61	0.85	58 726	
G188.793+1.030	06 09 06.96	21 50 41.23	0.80	58 703	
G189.030+0.784	06 08 40.67	21 31 06.90	0.85	58 705	
G189.471−1.216	06 02 08.37	20 09 20.10	0.80	58 727	
G189.777+0.344	06 08 35.30	20 39 06.59	0.90	58 727	
G196.454−1.677	06 14 37.05	13 49 36.16	0.80	58 719	1

Table A.2. Data used to create Fig. 5.

Source (l b)	6.7 GHz		12.2 GHz					
(° °)	$S_{\text{peak 2010}}$ (Jy)	$S_{\text{peak 2019}}$ (Jy)	$S_{\text{peak 2010}}$ (Jy)	$S_{\text{peak 2019}}$ (Jy)	$V_{\text{peak 2010}}$ (km s^{-1})	$V_{\text{peak 2019}}$ (km s^{-1})	$N_{\text{feat. 2010}}$	$N_{\text{feat. 2019}}$
G32.744−0.075	56.0	38.3	7.2	3.7	30.5	30.6	3	3
G33.641−0.228	140.0	145.0	29.3	37.8	58.8	60.3	3	2
G35.200−1.736	500.0	37.0	46.0	11.9	44.6	45.2	8	1
G36.115+0.552	40.0	13.7	4.9	2.4	74.6	75.1	1	1
G37.430+1.518	400.0	293.0	90.0	73.8	41.2	41.3	1	1
G37.546−0.112	4.0	4.0	1.4	1.1	50.0	50.0	1	1
G40.282−0.219	22.0	25.5	3.7	1.7	74.3	74.4	3	3
G40.425+0.700	22.0	24.7	8.2	7.9	6.7	6.6	2	2
G42.034+0.190	22.0	14.1	2.6	4.6	11.5	11.5	4	4
G43.890−0.784	9.0	9.1	4.2	2.4	47.9	51.7	2	2
G45.804−0.356	12.0	12.3	2.8	1.3	60.0	60.0	1	1
G49.043−1.079	33.0	12.1	7.1	0.9	37.4	36.3	2	1
G49.265+0.311	7.0	6.5	1.2	1.4	–4.2	–4.6	1	2
G49.349+0.413	8.0	7.3	2.8	2.0	68.3	68.1	2	2
G49.416+0.324	8.0	9.6	0.9	0.8	–10.5	-10.2	1	1
G52.199+0.723	6.0	9.8	5.4	2.8	3.7	3.3	2	2
G52.663−1.092	4.5	5.9	2.2	2.6	65.2	65.2	1	1

Notes. Column 2 presents crude estimation of the 6.7 GHz maser peak flux density from Breen et al. (2015), Col. 3 presents peak flux densities from unpublished 6.7 GHz line survey. Data for Cols. 4 and 6 is taken from Breen et al. (2016), Table 2. Columns 5 and 7 present the same data, as in Table 1. Last two columns present number of visible features on 12 GHz spectra from Breen et al. (2016) and this survey, respectively.

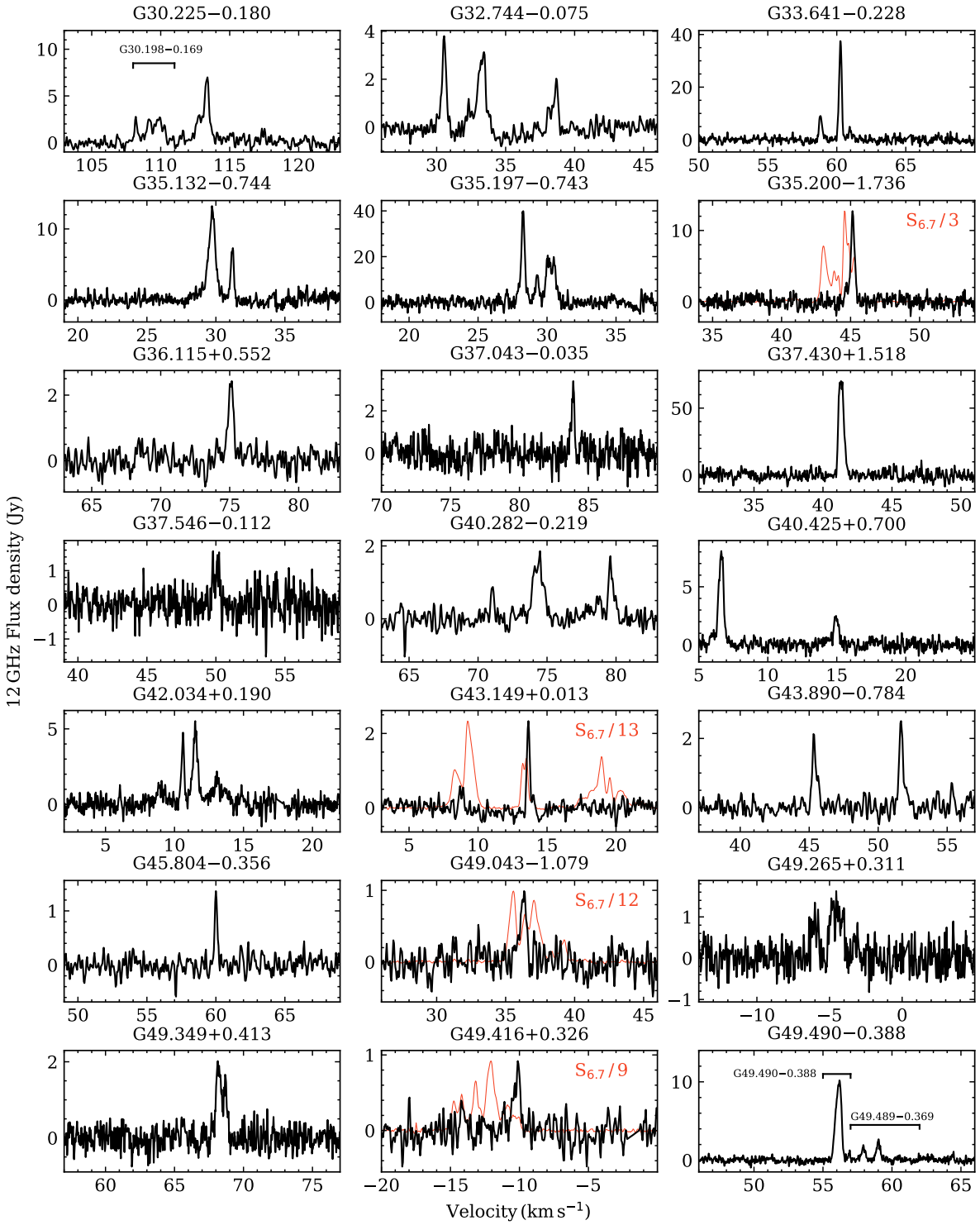

Fig. A.1. Spectra of 12.2 (black) and 6.7 GHz (red) methanol maser lines for previously known sources. The 6.7 GHz spectrum is shown only if taken contemporaneously with that at 12.2 GHz. The flux density of 6.7 GHz line is scaled by the factor given in the upper right corner.

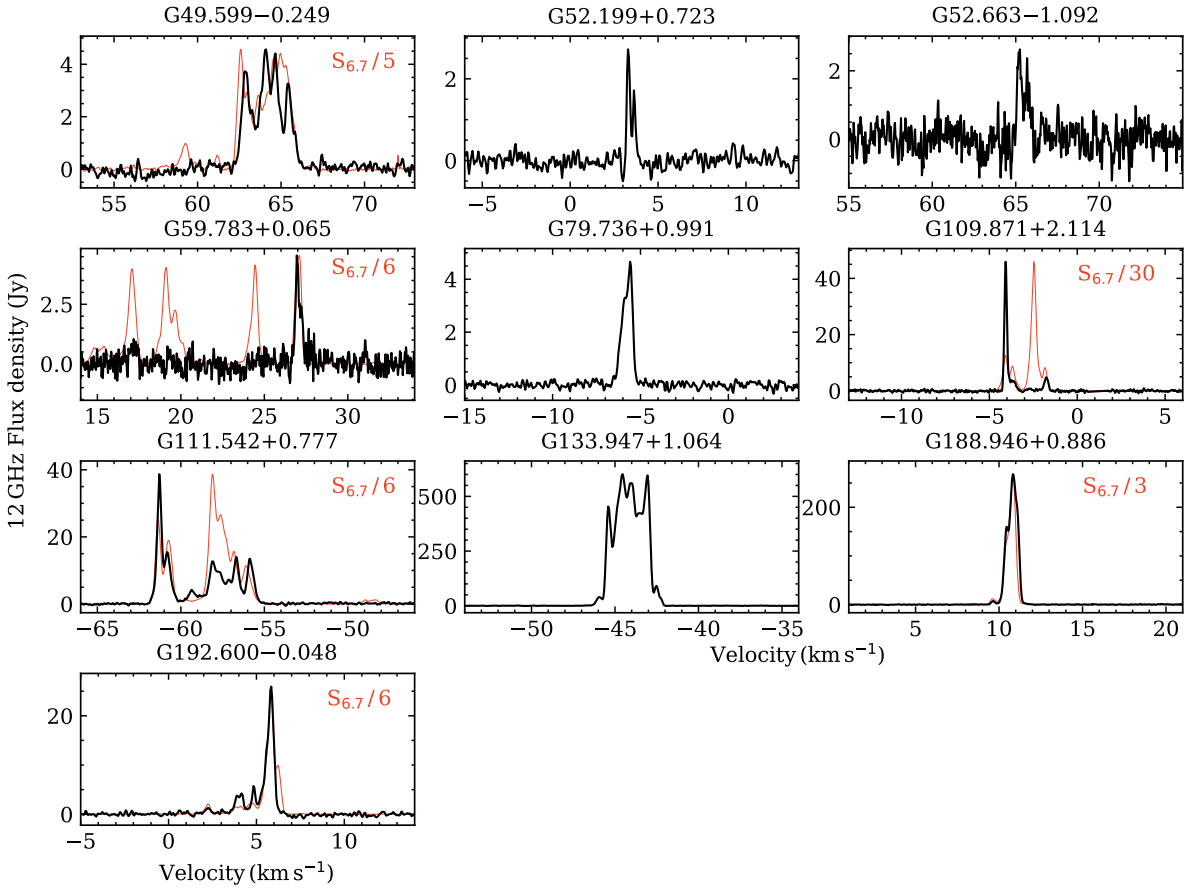

Fig. A.1. continued.

A&A 663, A123 (2022)
https://doi.org/10.1051/0004-6361/202243552
© M. Durjasz et al. 2022

Astronomy & Astrophysics

Discovery of recurrent flares of 6.7 GHz methanol maser emission in Cepheus A HW2

M. Durjasz[1], M. Szymczak[1], M. Olech[2], and A. Bartkiewicz[1]

[1] Institute of Astronomy, Faculty of Physics, Astronomy and Informatics, Nicolaus Copernicus University, Grudziadzka 5, 87-100 Torun, Poland
e-mail: md@astro.umk.pl
[2] Space Radio-Diagnostic Research Center, Faculty of Geoengineering, University of Warmia and Mazury Oczapowskiego 2, 10-719 Olsztyn, Poland

Received 15 March 2022 / Accepted 6 May 2022

ABSTRACT

Context. Class II methanol masers at 6.7 GHz originate close to high-mass young stellar objects (HMYSOs). Their high sensitivity to local condition variations makes them a useful marker of the activity of the emerging massive stars.
Aims. We aim to closely examine the variability of the 6.7 GHz CH_3OH masers in Cep A HW2 using the new and archival single-dish and high-resolution Very-Long-Baseline Interferometry (VLBI) datasets.
Methods. We monitored 6.7 GHz methanol masers towards the target between 2009 and 2021 using the Torun 32 m radio telescope, and analysed nine datasets of VLBI observations taken over 16 yr.
Results. Faint, extremely redshifted maser emission located close to the presumed central star position and coincident with the radio jet shows flaring activity with a period of ∼5 yr. Flares have an asymmetric profile with a rise-to-decay time ratio of 0.18 and relative amplitude higher than 10. The velocity of the flaring cloudlets drifts at a rate of $3–4 \times 10^{-5}$ km s^{-1} d^{-1} for about 11.5 yr of the monitoring. The time-lag between the peaks of the two flaring features implies a propagation speed of the exciting factor of ∼1000 km s^{-1}. Synchronised and anticorrelated variations of the flux density of blue- and redshifted features begin ∼2.5 yr after flares of the extremely redshifted emission.
Conclusions. Our observations suggest that the recurrent flares are the response of low-gain unsaturated maser regions to a relatively low increase in luminosity, which has little effect on the behaviour of most maser regions of higher gain.

Key words. masers – stars: massive – stars: formation – ISM: molecules – radio lines: ISM

1. Introduction

The 6.7 GHz class II methanol maser is the second strongest (after 22 GHz H_2O maser) interstellar emission line and originates from inside the vicinity of high-mass young stellar objects (HMYSOs) (Menten 1991). About one-third of these emission lines are associated with ultra-compact HII regions (UCHII) and it is believed that they originate primarily from younger objects, where ionisation processes have not yet developed (Hu et al. 2016). Theoretical models show that maser emission originates in regions with number densities up to 10^9 cm^{-3} and dust temperatures higher than 100 K (Sobolev et al. 1997; Cragg et al. 2005). There is theoretical (Sobolev et al. 1997) and observational (Olech et al. 2019, 2020) evidence that far-infrared (FIR) photons pump class II CH_3OH masers; their relation with IR radiation makes them a good marker of protostellar activity.

There are currently 1302 class II CH_3OH maser sources reported[1] (Ladeyschikov et al. 2019); most are associated with high- and intermediate-mass protostars (Szymczak et al. 2000; Pandian et al. 2007; Green et al. 2010; Breen et al. 2015; Hu et al. 2016). Some of them present substantial variability (e.g. Szymczak et al. 2018; Durjasz et al. 2019; Olech et al. 2019, 2020), suggesting that protostellar activity fluctuates on timescales ranging from less than a month up to a few years and more. There are also examples proving that massive protostars also show episodic outbursts that can change maser flux density by more than two orders of magnitude, namely S255−NIRS3 (Moscadelli et al. 2017; Szymczak et al. 2018), NGC 6334I-MM1B (Hunter et al. 2018), and G358.93−0.03 (Burns et al. 2020). These phenomena are believed to be caused by an increase in protostar accretion rate which increases star luminosity, effectively boosting the maser pump rate. Although these phenomena result in different flare profiles, they generally show a rapid increase in luminosity followed by much more gradual decay. These flare profiles suggest that maser emission is pumped during an outburst by radiative propagation rather than the physical motion of denser and/or hotter matter. Recent studies revealed thermal propagation in the protostellar disc plane with subluminal (≥4% of the speed of light) velocity (Burns et al. 2020). This phenomenon is explained by introducing a heatwave energy transfer due to photons, which are absorbed and re-emitted by dust grains.

The last two decades also brought the discovery of the periodic masers (Goedhart et al. 2003, 2004, 2009; Szymczak et al. 2011, 2016; Fujisawa et al. 2014; Maswanganye et al. 2016). Amongst them, there are short-period (∼1 month) and long-period (up to a few hundred days) sources; in some cases, only a few spectral features show periodic variations (Olech et al. 2019). As the CH_3OH masers have been monitored on a regular basis for over a decade now, we expect that masers with more extended

[1] https://maserdb.net

Open Access article, published by EDP Sciences, under the terms of the Creative Commons Attribution License (https://creativecommons.org/licenses/by/4.0), which permits unrestricted use, distribution, and reproduction in any medium, provided the original work is properly cited.
This article is published in open access under the Subscribe-to-Open model. Subscribe to A&A to support open access publication.

periods will start to be reported, as in the emission originating from around Cep A HW2 described in this work.

Cepheus A is a high-mass star-forming region located at a trigonometric distance of 700 ± 40 pc (Moscadelli et al. 2009) that hosts a cluster of YSOs. The brightest continuum source in this cluster is Cep A HW2 (Hughes & Wouterloot 1984), which is a HMYSO with a mass of ∼10 $M_\odot$ and bolometric luminosity of 2×10^4 $L_\odot$ (Sanna et al. 2017). Patel et al. (2005) revealed a dust emission core with a radius of ∼330 AU, inclination angle of 26° and mass of ∼1 $M_\odot$. HW2 also shows complex outflow activity; Rodriguez et al. (1994) estimated the ionised mass-loss rate to about 8×10^{-7} $M_\odot$ yr^{-1}, and Curiel et al. (2006) revealed proper motions of the jet components with an estimated velocity of ∼500 km s^{-1}. Jets also appeared to be slightly anti-parallel, which could be a result of the precession of the HW2 system. Observations of 2.12 µm H_2 and 115 GHz ^{12}CO ($J = 1-0$) (Cunningham et al. 2009) provided further data supporting the hypothesis of precession, presumably driven by a companion in an eccentric, non-coplanar orbit that triggers pulsing activity with passage through its periastron every ∼2500 yr.

Observations of the 22 GHz water vapour maser (Torrelles et al. 1996, 2001) revealed complex morphology with arc-like structures, which appeared to be tracing slow shock waves propagating through a rotating disc (Gallimore et al. 2003). Multi-epoch H_2O maser imaging (Torrelles et al. 2011) revealed the simultaneous presence of a wide-angle (102°), slow (13–18 km s^{-1}) outflow and narrow-angle (18°) ionised, fast (70 km s^{-1}) jet.

Recent 44 GHz continuum imaging (Carrasco-González et al. 2021) revealed that slow outflow originates from a region at a distance of ∼3 AU from the HW2 protostar and is collimated into a jet ∼25 AU away. The proposed scenario of external collimation is the presence of a large-scale magnetic field and a dense ambient medium. Vlemmings et al. (2010) reported the presence of a large-scale magnetic field of ∼23 mG directed perpendicularly to the disc plane, suggesting that in this case the accretion onto the disc plane is likely regulated by magnetic forces.

Menten (1991) were the first to report 6.7 GHz CH_3OH masers in Cep A HW2 with a peak flux density $F_{6.7} = 1420$ Jy at $V_{\rm lsr} \simeq 2.5$ km s^{-1}. Subsequent observations did not show significant variations in the profile shape but substantial variations in the amplitude, which reached a factor of 3 over ∼25 yr (Szymczak et al. 2000, 2012; Vlemmings 2008; Sugiyama et al. 2008; Fontani et al. 2010; Hu et al. 2016; Sanna et al. 2017; Yang et al. 2017). Synchronised and anticorrelated variations between the three most blueshifted and two most redshifted spectral features were reported by Sugiyama et al. (2008). VLBI observations of the methanol masers revealed that they originate from a distance of between 300 and 1000 AU from the presumed position of HW2 and present arc-like structure with velocity field showing no signs of rotation, but consistent with the infall scenario (Torstensson et al. 2011). Proper-motion measurements (Sugiyama et al. 2014; Sanna et al. 2017) confirmed this scheme, which suggests that disc accretion is the most likely scenario of the formation of Cep A HW2. Long-term monitoring (Szymczak et al. 2014) also revealed the episodic presence of the redshifted low-amplitude spectral features and radial velocity drifts of these and a few persistent features.

In the present work, we extend the Szymczak et al. (2014) dataset by reporting results from 12 yr of single-dish monitoring and VLBI imaging of the CH_3OH masers in Cep A HW2. Our main result is the detection of periodic (≃5 yr) variability of the redshifted faint emission.

2. Observations

2.1. Single-dish observations

We used new and archival (Szymczak et al. 2014) 6.7 GHz data obtained with the Torun 32 m radio telescope. We observed the target source as part of a monitoring program from June 2009 to December 2021 and acquired new data from March 2013 with a typical cadence of nine observations per month. There were several gaps of 3–4 weeks. Due to telescope maintenance, we took no single-dish spectra between 2020 May and October.

The full-beam width at half maximum of the antenna at 6.7 GHz was 5′.8, and the pointing error was ∼25″ before mid-2016 and ∼10″ later (Lew 2018). The system temperature ranged from 25 to 40 K. The data were dual-polarisation taken in frequency switching mode. We used the autocorrelation spectrometer to acquire spectra with a resolution of 0.09 km s^{-1} after Hanning smoothing and a typical 1σ noise level of 0.35 Jy before May 2015 and 0.25 Jy afterward. We based the flux density scale on continuum observations of 3C123 and spectra of little variable methanol maser source G32.744−0.076 (Szymczak et al. 2014). The resulting accuracy of the absolute flux density was better than 10%.

2.2. European VLBI Network observations

We carried out European VLBI Network (EVN)[2] observations in June and October 2020; project codes were RD002 and ED048B, respectively (Table 1). Phase-referencing observations of the 6.7 GHz methanol maser line were performed and correlated with two polarisation combinations (RR, LL). J2302+6405 was used as a phase-referencing calibrator and 2007+777 as a fringe finder. J2254+6209 was used as a phase-referencing calibrator for the RD002 project. Scans on the target and phase calibrators were performed in 5 min cycle: 3 min 15 s on Cep A, 1 min 45 s on phase calibrator. The data were processed with the SFXC software correlator (Keimpema et al. 2015) at the Joint Institute for VLBI in Europe using 1 s averaging time and two frequency setups. The first setup for high spectral sampling used 2048 channels over a 4 MHz band (2 MHz for RD002), yielding channel spacing of 0.088 km s^{-1} (0.044 for RD002) and the second setup used 8 × 4 MHz band with 128 channels to improve the sensitivity of the calibrator maps. We reduced the data using the NRAO Astronomical Image Processing System (AIPS), following standard procedures described in the EVN data reduction guide[3]. Fringe fitting in both projects was done using phase-referencing calibrators to improve astrometry. We produced intensity maps (Stokes I) within an area of 2″ × 2″ around the phase-centre and estimated the intensity of maser emission by fitting a 2D Gaussian function (task JMFIT in NRAO AIPS package). The final 1σ noise level in both projects was better than 6 mJy beam^{-1} for emission-free channels.

2.3. Archival VLBI data

In this work, we also make use of the publicly available EVN (Torstensson et al. 2011; Sanna et al. 2017) data and Japanese VLBI Network (JVN; Sugiyama et al. 2014) observational results for a total of seven epochs. Archival EVN data from experiments ES071A, ES071B, and ES071C (Sanna et al. 2017) were reduced,

[2] The EVN is a joint facility of European, Chinese, South African and other radio astronomy institutes funded by their national research councils.

[3] https://www.evlbi.org/evn-data-reduction-guide

Table 1. VLBI observations used in the paper.

Epoch			Exp.	Telescope[(a)]	Vel. res.	1σ noise	Beam	Ref.
No.	Date	MJD	code		(km s^{-1})	(mJy beam^{-1})	(mas × mas, °)	
1	2004 Nov. 06	53 315	EL032	EVN(8)	0.09	7	13.8 × 5.3, −57	1
2	2006 Sep. 09	53 987		JVN(4)	0.18	60	9.4 × 4.3, −70	2
3	2007 Jul. 28	54 309		JVN(5)	0.18	90	9.2 × 4.3, −43	2
4	2008 Oct. 25	54 764		JVN(5)	0.18	120	7.0 × 3.9, −79	2
5	2013 Mar. 01	56 352	ES071A	EVN(8)	0.04	4–6	4.3 × 3.1, −58	3
6	2014 Feb. 28	56 716	ES071B	EVN(8)	0.04	4–6	4.0 × 3.4, −67	3
7	2015 Mar. 13	57 094	ES071C	EVN(9)	0.04	4–6	3.9 × 3.0, −53	3
8	2020 Jun. 02	59 002	RD002	EVN(4)	0.04	5	7.5 × 3.5, +86	4
9	2020 Oct. 18	59 140	ED048B	EVN(8)	0.09	4	4.5 × 3.8, +12	4

Notes. [(a)]Telescopes are the EVN and the Japan VLBI Network (JVN). The number of antennas is given in parentheses.
References. (1) Torstensson et al. (2011); (2) Sugiyama et al. (2014); (3) Sanna et al. (2017); (4) this work.

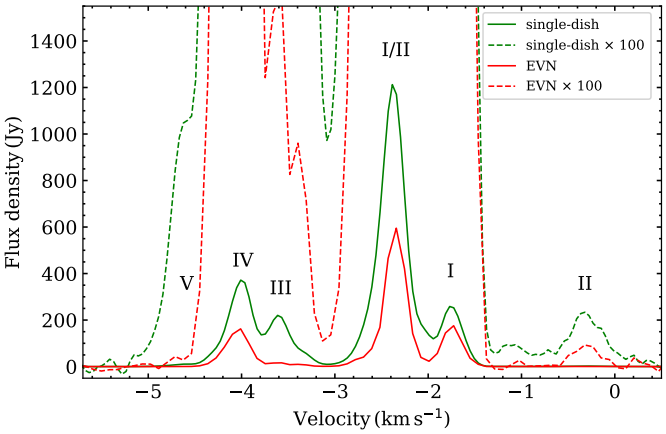

Fig. 1. 6.7 GHz maser single-dish auto-correlation spectrum of Cep A HW2 (green) obtained on 2020 October 18 and the cross-correlated spectrum from EVN observations (red) taken on the same date. The dashed lines represent the same spectra magnified 100 times to show low-flux-density features. The features are marked by roman numerals following Sugiyama et al. (2008), which correspond to clusters shown in Fig. 3.

while for the rest, the parameters of maser spots were taken from published tables (Torstensson et al. 2011; Sugiyama et al. 2014, their Tables 3 and 5, respectively). Details of all VLBI projects used in this paper are listed in Table 1.

3. Results

We find that in addition to five persistent features known since discovery (Menten 1991), the 6.7 GHz maser spectrum of the target has two intermittent low-intensity features (Fig. 1). At the beginning of the first flare observed during the monitoring, these two most redshifted features peaked at −1.3 and −0.5 km s^{-1}. This designation is used hereafter for clarity, even though both features drift in velocity (Sect. 3.1). Light curves of the main features (Fig. 2) illustrate significant variability of the emission. They present previously reported synchronous anticorrelation of red- and blueshifted features (Sugiyama et al. 2008; Szymczak et al. 2014) and the cyclical activity of the most redshifted, weak features over ∼12 yr are revealed for the first time.

In this publication, we adopt the definition of *spot* and *cloudlet* provided by Sanna et al. (2017). New VLBI data are summarised in Fig. 3, showing the spatial distribution of the maser cloudlets, and in Tables A.1 and A.2, which list the spot parameters. We detected 90 and 71 individual maser spots above the 5σ threshold in epochs 8 and 9, respectively. The main properties of cloudlets derived from our EVN observations in epochs 8 and 9 are given in Table A.3. In addition, the parameters of the corresponding cloudlets detected in epochs 5–7 are added.

In our observation epochs, the maser cloudlets were distributed over five clusters (Fig. 3), forming the arched structure well known from previous studies (Vlemmings et al. 2010; Torstensson et al. 2011; Sugiyama et al. 2014; Sanna et al. 2017); this implies the overall 6.7 GHz maser structure is stable for ∼15 yr.

3.1. Recurrent flares of the most redshifted emission

The features −1.3 and −0.5 km s^{-1} were detected three times during our 12-year monitoring period. The parameters of the flares are listed in Table 2, where we assume the start and end of burst as the nearest data points with flux density below 3σ before and after the data point which has flux density exceeding 5σ (similarly to Pietka et al. 2015). The intervals between the onset of subsequent flares are 1796, 1870 d and 1787, 1859 d for −1.3 and −0.5 km s^{-1} features, respectively, resulting in an average period of 1828 d with the range of 168 d. Flares at −1.3 and −0.5 km s^{-1} lasted 99–387 and 227–583 d, respectively, which are on average 13 and 22% of the period. The flared profile is highly asymmetric; the average rise and decay times are 35d and 200 d (−1.3 km s^{-1}), and 32d and 373 d (−0.5 km s^{-1}). We notice that the flare parameters for the −1.3 km s^{-1} feature show greater dispersion than those for −0.5 km s^{-1}.

Figure 4 shows the time series of the two redshifted features folded with a period of 1828 d. The flare duration and peak flux density differ significantly from cycle to cycle. At −1.3 km s^{-1}, the flare onset occurs 41–61 d earlier than that at −0.5 km s^{-1}.

During the first flare, both flaring features exhibited a systematic drift of peak velocity (Szymczak et al. 2014). The present study extends the data for two subsequent cycles. To quantify the rate of velocity drift, we fitted the Gaussian function to the spectra using the CURVE_FIT method from the SCIPY.OPTIMIZE package (Virtanen et al. 2020). The following intervals are analysed: MJD 55 224–55 792 (flare #1),

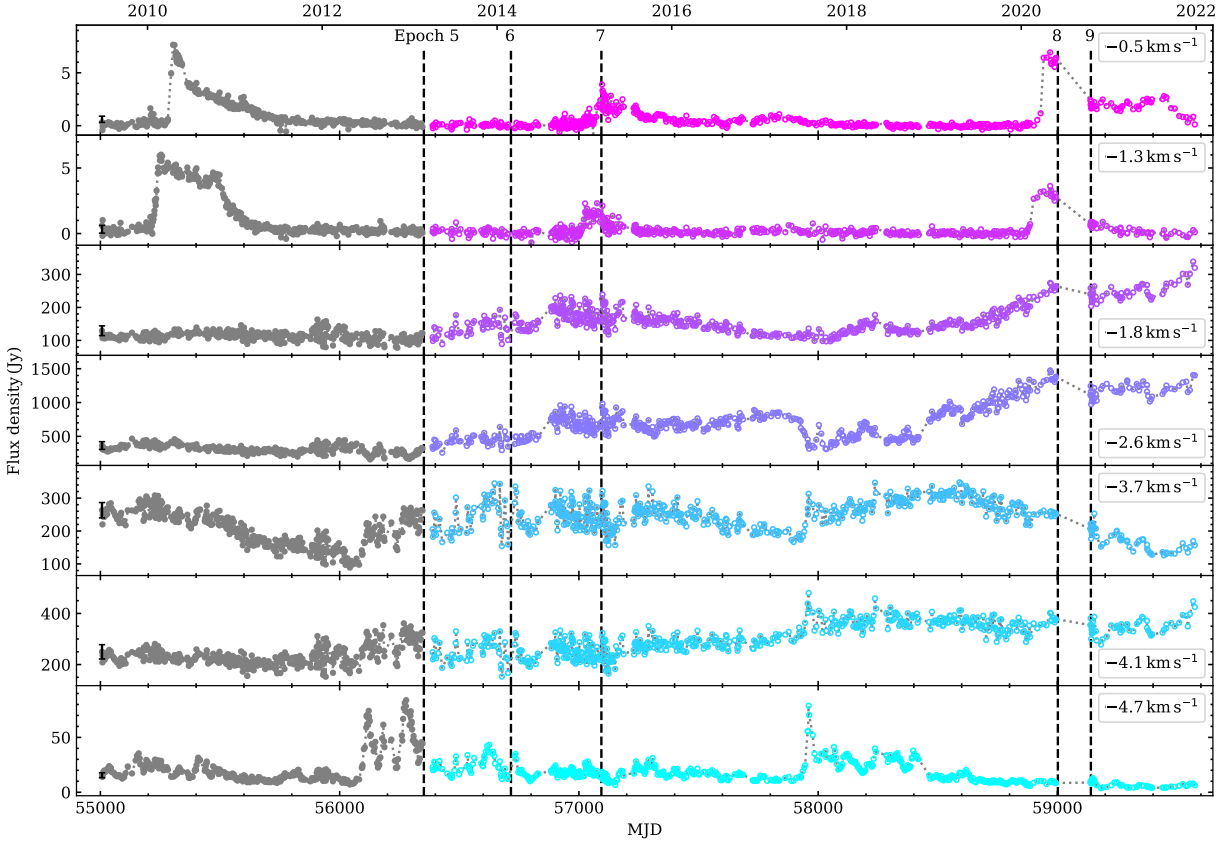

Fig. 2. Light curves of the main spectral features of the 6.7 GHz transition in Cep A HW2. Data before MJD 56 352 (grey dots) were published in Szymczak et al. (2014). Typical measurement uncertainty is shown by the black bar for the first data point. The light curves were produced using single-dish data (Sect. 2.1) by averaging three channels; the velocity of the central channel is given for each panel. Colours indicate different spectral features at velocities given to the right of the plots. The vertical black dashed lines mark VLBI observations; epoch numbers correspond to those given in Table 1. VLBI observations at epochs 1–4 were performed before our single-dish monitoring started.

Table 2. Flare parameters of the −1.3 and −0.5 km s^{-1} features.

$V_{\rm lsr}$ (km s^{-1})	$t_{\rm start}$ (MJD)	$t_{\rm peak}$ (MJD)	$t_{\rm end}$ (MJD)	$F_{\rm peak}$ (Jy)
Flare #1				
−1.3	55 222	55 255	55 609	6.0
−0.5	55 283	55 307	55 679	7.6
Flare #2				
−1.3	57 018	57 025	57 117	2.7
−0.5	57 070	57 095	57 297	3.3
Flare #3				
−1.3	58 888	58 953	59 104	3.5
−0.5	58 929	58 966	59 512	7.0

Notes. $V_{\rm lsr}$ is the peak velocity at the beginning of the first flare, $t_{\rm start}$, $t_{\rm peak}$, and $t_{\rm end}$, are the start, maximum, and end times of the flare, respectively, and $F_{\rm peak}$ is the peak flux density.

57 007–57 488 (flare #2), and 58 882–59 792 (flare #3). The result obtained is shown in Fig. 5. The rates of velocity drift are 0.015 ± 0.001 and 0.012 ± 0.001 km s^{-1} yr^{-1} for the features at −0.5 and −1.3 km s^{-1}, respectively. For the feature at −0.5 km s^{-1}, there is evidence of an increase in drift rate at the end of flares #1 and #3 that deviates from the average value derived from the long-term data.

3.2. Position and properties of the most redshifted cloudlets

The emission of the −0.5 km s^{-1} feature originates from cluster II (Fig. 3, Tables A.1 and A.2). EVN observations in epoch 8 revealed the emission of −0.5 km s^{-1} feature with the peak brightness of 0.42 Jy beam^{-1} at −0.38 km s^{-1} and with FWHM equal to 0.34 km s^{-1}. After 4.5 months, in epoch 9, the brightness decreased to 0.28 Jy beam^{-1}, the peak velocity shifted to −0.30 km s^{-1} and FWHM increased to 0.40 km s^{-1} (Fig. 6). This feature in the 32 m spectrum taken on 2020 May 24, a week before the EVN experiment, reached a peak flux density of 6.2 Jy, indicating that about 93% of the maser flux is missing; thus, this flaring emission is highly resolved out with the EVN beam.

In epoch 8, the −0.5 km s^{-1} cloudlet has a linear structure of about 3 mas × 2.5 mas in size with the velocity gradient of 4.19 mas/ km s^{-1} along with PA ≃ −75° (Fig. 6). In epoch 9, the blue part of the cloudlet is preserved, while the red part folds into a hook. A slightly curved morphology was observed in epoch 7 by Sanna et al. (2017; Fig. 6), but its general appearance resembles that seen in our data. Details of cloudlet parameters from Gaussian fitting are presented in Table A.3.

We note that the peak velocities inferred from EVN observations in epochs 7–9 are consistent with values obtained from the single-dish spectra and confirm the rate of velocity drift of 0.015 km s^{-1} yr^{-1}.

No emission at −0.5 km s^{-1} was detected in epochs 5 and 6 (Sanna et al. 2017) when the RMS noise level in a line-free

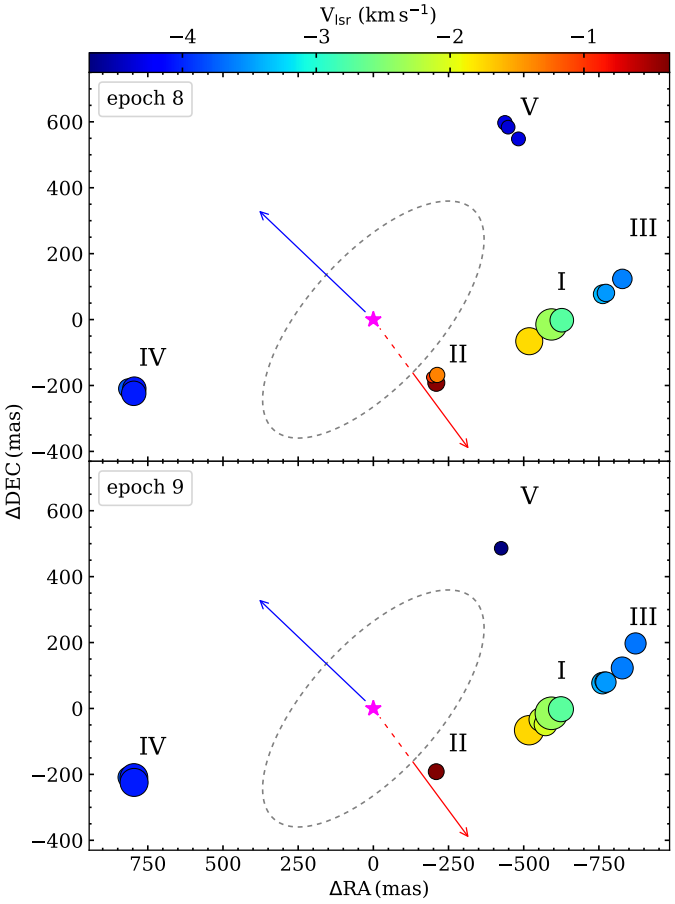

Fig. 3. Spatial distributions of the 6.7 GHz methanol maser cloudlets in Cep A HW2 in epochs 8 and 9. The circle size is scaled as the logarithm of peak brightness; its colour corresponds to the local standard of rest velocity scale shown in the wedge. Roman units indicate the cloudlet numbering according to Sugiyama et al. (2014) and Sanna et al. (2017). The magenta star marks the Cep A HW2 position (Curiel et al. 2006): $\alpha(\mathrm{J2000}) = 22^{\mathrm{h}}56^{\mathrm{m}}17.9816^{\mathrm{s}}$, $\delta(\mathrm{J2000}) = 62°01'49.572''$. The ellipse denotes the dust disc emission at 0.9 mm (Patel et al. 2005), and the arrows mark the elongated knot directions at the base of the jet detected at 7.5 mm (Carrasco-González et al. 2021).

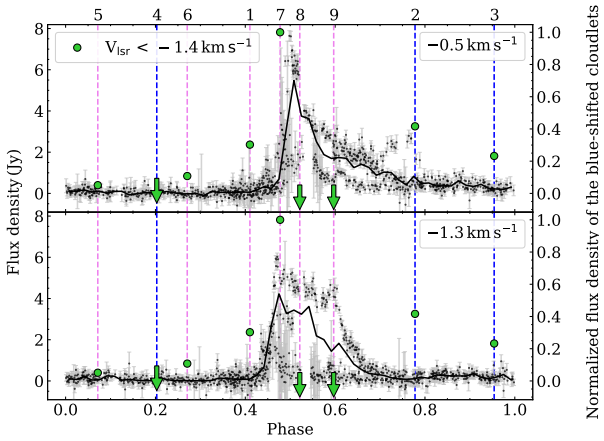

Fig. 4. Folded light curves of the redshifted flaring emission for −0.5 (*top*) and −1.3 km s^{-1} (*bottom*) features. The data points are black with grey error bars, while the black solid lines show the average profiles. Green points refer to the relative intensities of the blueshifted emission observable in cluster II; arrows mark upper limits for the blueshifted emission in epochs with no detection. The vertical dashed lines correspond to the computed phases of VLBI observations (magenta – EVN, blue – JVN); the epoch numbers (Table 1) are given above the top abscissa.

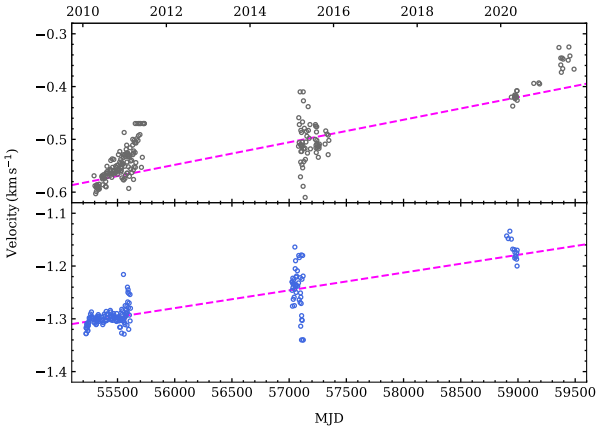

Fig. 5. Drifts of radial velocity of the −0.5 (*top*) and −1.3 km s^{-1} (*bottom*) features. The magenta dashed line marks the linear function fit.

channel was ∼5 mJy beam^{-1}, which corresponds to a brightness temperature of 8×10^6 K. During the flare, in epochs 8 and 9, the brightness temperature of the brightest part of the cloudlet has increased to 2.2×10^8 and 1.5×10^8 K, respectively.

Using the procedure outlined by (Sanna et al. 2017) and the EVN data from epochs 7 and 9, we estimated that the proper motion of the −0.5 km s^{-1} cloudlet is $V_{\mathrm{RA}} = -2.06 \pm 0.12$ km s^{-1}, $V_{\mathrm{Dec}} = 2.91 \pm 0.17$ km s^{-1}; which implies infall and rotation velocity components of 4.0 and 3.8 km s^{-1}, respectively. Therefore, the rotational velocity is about 85% of the expected Keplerian velocity at a distance of 450 AU for the assumed mass of HW2 of 10 $M_\odot$.

Our EVN data imply that the −1.3 km s^{-1} emission was only detected in epoch 8 as two groups of spots separated in position (>15 mas) and velocity (Fig. 6). The profile of the group with the intensity peaking near −1.4 km s^{-1} appears as an incomplete Gaussian, while that peaking near −1.1 km s^{-1} is irregular. The latter, composed of three spots in contiguous channels, has an intensity slightly above the 5σ level and a brightness temperature of 2×10^7 K; its position is very close to that observed in epoch 7, and the difference in velocity between the two epochs is consistent with the velocity drift trend inferred from the single-dish observations. A comparison of the cross-correlation and auto-correlation spectra reveals that the −1.3 km s^{-1} emission is highly resolved out; the missing flux is about 95%. We suggest that significant evolution of this redshifted emission took place over a timescale of 5 yr. However, as the data in epoch 8 were obtained with use of a limited number of antennas and the map dynamic and angular resolution is lower than in the other epochs, the observed morphology and profile may be distorted.

Both −0.5 and −1.3 km s^{-1} cloudlets are located close to each other at a distance of 35 mas, which corresponds to 50 AU when the inclination angle of 64° and position angle of 134° (Sanna et al. 2017) are taken into account. For the presumed position of the star proposed by Curiel et al. (2006), the corresponding distances are 650 mas (450 AU) and 600 mas (420 AU). Assuming that the central source produces the flare, a triggering factor would first reach the −1.3 km s^{-1} and then the −0.5 km s^{-1} cloudlet; this is in good agreement with the single-dish

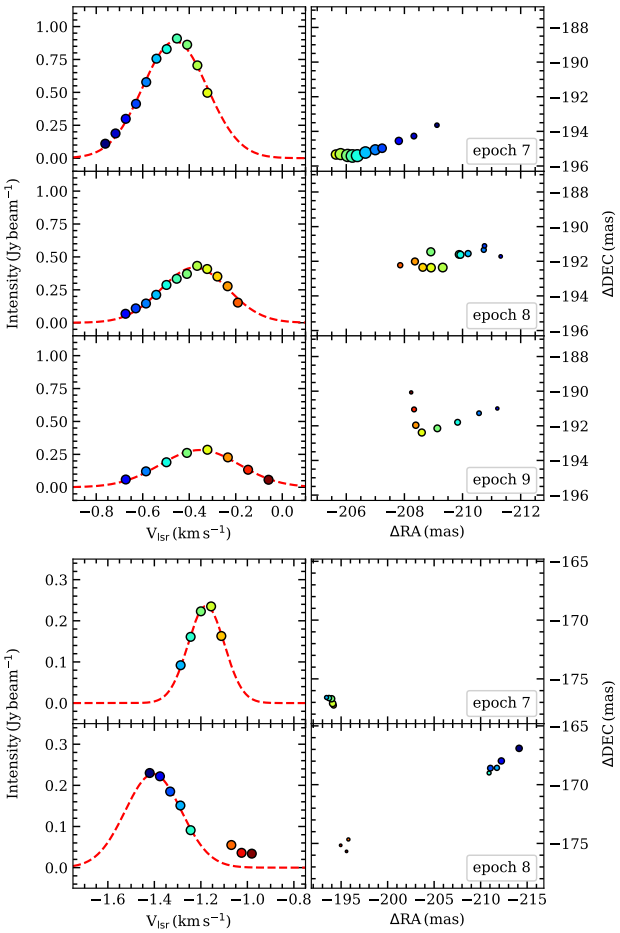

Fig. 6. Line profiles (*left*) and distributions (*right*) of the maser spots in the two most redshifted cloudlets at the indicated epochs (Table 1). Each symbol represents a methanol maser spot. The red dashed line denotes the Gaussian function fit (Table A.3). The symbol sizes in the right column are proportional to the square root of brightness, whereas the colours refer to velocity.

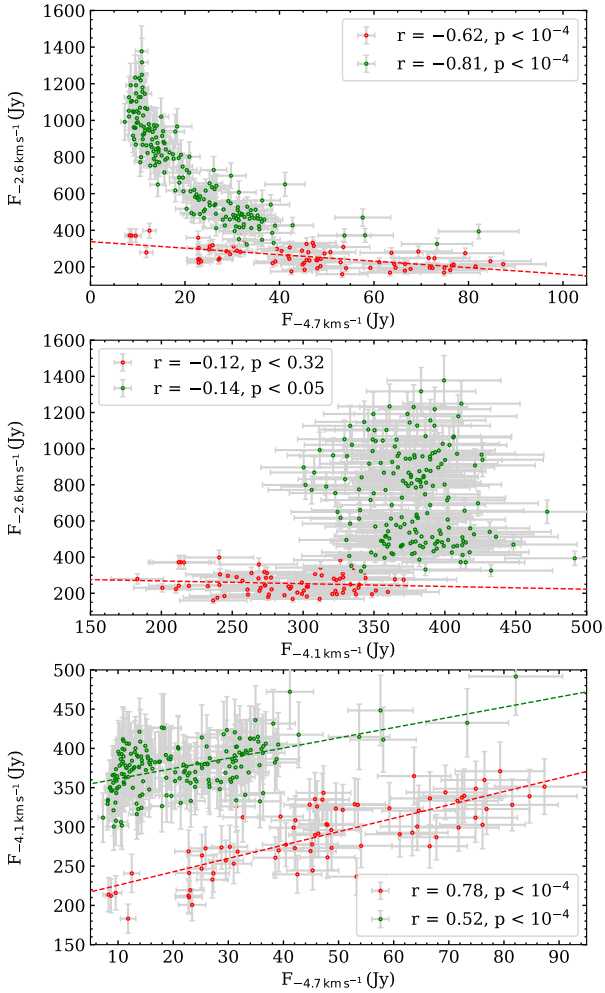

Fig. 7. Comparison of peak flux densities of the selected features. Red and green points refer to measurements from intervals of MJD 56 057–56 347 (similarly as in Szymczak et al. 2014) and MJD 57 862–58 851, respectively. The dashed lines mark the best fit of the linear function.

monitoring results, which revealed time-lags between the onset of the flares. The time-lag of 51 d estimated for the 2015 flare (~MJD 57 020) implies that an exciting factor is moving with a velocity of ~1000 km s^{-1} in the plane of the maser disc.

3.3. Long-term variability of cluster II

Figure B.1 presents the spot maps of cluster II in nine epochs of VLBI observations. The redshifted flaring emission was visible in epochs 2, 7, 8, and 9. These epochs were in active state assuming a variation period of 1828 d (Fig. 4). Our EVN measurements provide evidence that the flaring emission comes preferentially from cluster II which is located very close to the outer edge of the dust disc (Patel et al. 2005; Sanna et al. 2017). In six VLBI observation epochs, the emission peaking at −2.4 km s^{-1} (Fig. B.1) was detected in cluster II.

3.4. Synchronous and anticorrelated variability

Closer examination of the light curves in Fig. 2 reveals anticorrelation between peak flux densities of the −2.6, −4.1, and −4.7 km s^{-1} features during high-variability periods of the −4.7 km s^{-1} component. To quantify this anticorrelation, we calculated Pearson correlation coefficients using the method PEARSONR from the SCIPY.STATS package (Virtanen et al. 2020). A similar analysis was performed by Szymczak et al. (2014); here we repeat it with the extended dataset. Results are presented in Fig. 7. We find a statistically meaningful anticorrelation between light curves of the −2.6 and −4.7 km s^{-1} features for both periods of activity of the −4.7 km s^{-1} feature (MJD 56 057–56 347 and MJD 57 862–58 851), but only for the first period (MJD 56 057–56 347) between −2.6 and −4.1 km s^{-1}. There is also a statistically meaningful correlation between the features at −4.1 and −4.7 km s^{-1}. The relation between peak flux densities of the −4.7 and −2.6 km s^{-1} features appears to be non-linear in the second period (MJD 57 862–58 851), which suggests that the degree of saturation of one of the features varies during these periods, implying changes in the pumping efficiency. We also calculated correlation coefficients for the whole observing period; the results are presented in Table 3. The strong anticorrelation between the features at −2.6 and −4.7 km s^{-1} suggests that time-delays between variations of these features are relatively low. These time-delays likely correspond to the time it would take the light to travel between cloudlets. From Sanna et al. (2017), we can estimate the distance to 860 AU, which would take about five days for the light to travel. We decided to fit the Gaussian function to visible symmetrical peaks

Table 3. Correlation coefficients of the 6.7 GHz spectral features in Cep A HW2 for the whole monitoring period.

Feature ($km\,s^{-1}$)	−1.8	−2.6	−3.7	−4.1
−2.6	0.87			
−3.7	0.26	0.28		
−4.1	0.47	0.59	0.60	
−4.7	−0.32	−0.43	0.32	0.24

Table 4. Results of Gaussian fits shown in Fig. 8.

Profile No.	V_{lsr} ($km\,s^{-1}$)	MJD_{peak} (d)	$FWHM$ (d)
1	−2.6	56 126.6 ± 1.1	52.4 ± 3.5
	−4.7	56 118.8 ± 1.1	39.3 ± 2.3
2	−2.6	56 292.6 ± 1.3	74.2 ± 4.7
	−4.7	56 283.7 ± 1.8	78.3 ± 4.7

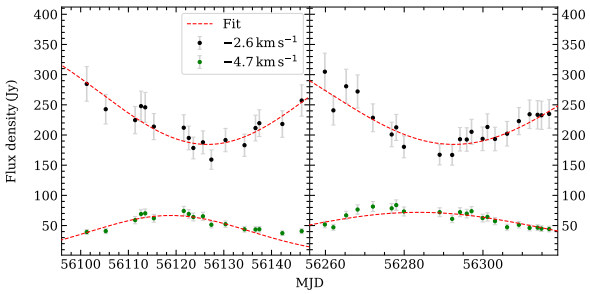

Fig. 8. Gaussian fits to light curves of the −2.6 and −4.7 $km\,s^{-1}$ features for periods MJD 56 100–56 140 and 56 260–56 300.

in −4.7 and flux minima in −2.6 $km\,s^{-1}$ light curves to estimate time-lags. Estimated time-lags between the features at −4.7 and −2.6 $km\,s^{-1}$ are 7.7 ± 1.5 and 8.9 ± 2.1 days for profiles #1 and #2, respectively. These values are well within an order of magnitude of the light-crossing time between −2.6 and −4.7 $km\,s^{-1}$ cloudlets (Table 4, Fig. 8).

Given that the features at −2.6 and −4.7 $km\,s^{-1}$ show strong anticorrelation in intervals of MJD 56 057-56 347 and MJD 57 862–58 851 (Fig. 7), it seems reasonable to examine how the peak velocities (V_{lsr}) behave over time; results are presented in Fig. 9. In addition to an apparent non-linear drift towards positive V_{lsr}, the feature at −2.6 $km\,s^{-1}$ shows rapid drifts towards positive V_{lsr} during the anticorrelation periods. The feature at −4.7 $km\,s^{-1}$ shows the opposite behaviour; in specified periods, it drifts towards more negative values of V_{lsr}.

3.5. Properties of other regions

Results of closer examination of cloudlets with Gaussian function fits are listed in Table A.3. Their general characteristics are a simple linear or slightly arched morphology and an explicit velocity gradient. The size measured as the distance of the extreme spots ranges from 0.4 to 13 AU, while the brightness temperature is between 1.1×10^7 and 5.6×10^{10} K.

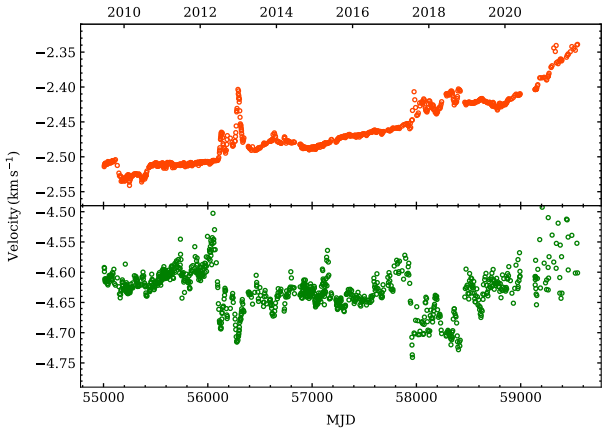

Fig. 9. Radial velocity curves for −2.6 and −4.7 $km\,s^{-1}$ features.

4. Discussion

4.1. Evidence of recurrent variability

The first report of flares in two redshifted features (−1.3 and −0.5 $km\,s^{-1}$) at the beginning of 2010 was presented by Szymczak et al. (2014). The present single-dish study indicates that the emission of these two features occurs regularly in intervals of 4.9–5.1 yr. A comparison of our VLBI maps with those published by Torstensson et al. (2011), Sugiyama et al. (2014), and Sanna et al. (2017) (Figs. 4 and B.1) provides a more detailed picture of the 6.7 GHz maser variability in cluster II. We can see that the epoch 1 (Table 1) observation was made before the flare of the redshifted cloudlets, as our ephemerid suggests, and only the blueshifted spots (−2.5 $km\,s^{-1}$) were detected. The observation in epoch 2 was conducted at the end of the flare, and faint ($F_{peak} < 3.5$ Jy $beam^{-1}$) emission of the redshifted (−0.5, −1.3 $km\,s^{-1}$) and blueshifted (−2.5 $km\,s^{-1}$) cloudlets was seen. No emission at −0.5 and −1.3 $km\,s^{-1}$ was detected in epochs 3 or 4, that is, during a quiescent state anticipated by the ephemerid, and only faint blueshifted emission (−2.5 $km\,s^{-1}$) was detected in epoch 3. In epochs 5 and 6, the EVN detected only faint blueshifted (−2.5 $km\,s^{-1}$) cloudlets, while in epoch 7, they significantly increased, and the −0.5 and −1.3 $km\,s^{-1}$ cloudlets reappeared. In epoch 8, only the redshifted emission was seen for both cloudlets. In epoch 9, the emission at −0.5 $km\,s^{-1}$ diminished, whereas the −1.3 $km\,s^{-1}$ emission disappeared. We conclude that the published VLBI data fully confirm the recurrent appearance of the −1.3 and −0.5 $km\,s^{-1}$ emission, supporting our single-dish monitoring. Furthermore, these data may suggest that slightly blueshifted emission of −2.5 $km\,s^{-1}$ also exhibits a periodic behaviour. We note that this blueshifted emission in cluster II is highly blended with cluster I, preventing us from finding its light curve.

4.2. Flare characteristics and their origin

Fast growth and a slow drop in the flux density are the main characteristics of the flare profile of the redshifted emission in Cep A HW2, and are preserved from cycle to cycle. The peak flux varies by a factor of 3, while the duty cycle ranges from 0.06 to 0.16 (Fig. 4). Here, the duty cycle is the fraction of a flare period for which the flux density is above half of the peak value. The rise-to-decay time ratio of the flare is 0.18 on average, and the relative amplitude is higher than 10. For a sample of all known periodic masers listed in Olech et al. (2019) (le A3),

we infer that the duty cyctheir Table ranges from 0.16 to 0.97, while the rise-to-decay time ratio is 0.3−2.0. The relative amplitude ranges from 0.2 to 5 in most cases, but there are five objects with lower limits of 5−120. Therefore, we find that the above-mentioned characteristics of the flared cloudlets in the target are close to the boundary values reported in known periodic masers. A period of 1828 d is the only characteristic of Cep A HW2, which stands out by an order of magnitude from the median value of 200 d (Olech et al. 2019) inferred for a sample of 25 known periodic masers.

There are three models that could explain the specific flare profile of the redshifted emission; pulsation instability due to the κ mechanism (Inayoshi et al. 2013a), a colliding wind binary (van der Walt 2011), or spiral shocks in the central gap of the accretion disc (Parfenov & Sobolev 2014). Pulsation instability due to the κ mechanism allows the stellar masses to be estimated with a power-law relation (Inayoshi et al. 2013b, their Eq. (2)). In the case of Cep A HW2, a period of ∼5 yr implies a mass of over 40 $M_{\odot}$, which is between two and four times higher than values derived from the observed bolometric luminosity (Sanna et al. 2017). We therefore argue that the observed variability cannot be explained by the κ instability mechanism.

Van der walt (2011) explains the periodic variability of the methanol masers with a colliding wind binary scenario. Briefly, periodic stellar wind interactions in the binary system generate additional free-free radiation that increases seed photon flux. Cooling of the plasma is much less abrupt, resulting in a characteristic profile with the rapid rise and slow decay. A rough check shows that both −0.5 and −1.3 km s^{-1} maser cloudlets in cluster II lie very close to the radio continuum emission knots (Curiel et al. 2006) suggesting that the maser flares might be induced by modulation of the background radiation. The position of the centroid of the −0.5 km s^{-1} maser emission measured with the EVN beam (Table 1) in epochs 8 and 9 coincides within 45 mas with the axis of radio jet (Curiel et al. 2006; Carrasco-González et al. 2021). A very similar coincidence is seen for the centroid of the −1.3 km s^{-1} emission. The width of the 22 GHz radio knot is ∼70 AU (Curiel et al. 2006; Carrasco-González et al. 2021), while the size of the maser region in cluster II is 75 AU (as estimated from epoch 7); it is therefore quite certain that the maser volume could be illuminated by the background continuum radiation. Our observations imply that the brightness temperature difference between the active and quiet states of the −0.5 and −1.3 km s^{-1} emission is more than one order of magnitude. Cyclic changes of the continuum emission could have been induced by an accretion event or outflow. The radio continuum emission at centimetre wavelengths in Cep A HW2 shows moderate (∼70%) variability on a timescale of 10 yr (Curiel et al. 2006), which could be considered as a possible explanation for the characteristics of the flares. However, if the maser flares were generated by variations of background photon flux then there would be no time-lags (Table 2), which, on the other hand, we clearly observe. We therefore conclude that changes in the background radiation are not the cause of the maser flares in cluster II.

Characteristic flare profile could also be achieved by the spiral shock model (Parfenov & Sobolev 2014). In this scenario, an OB binary on a circular orbit creates shocks that travel through the central disc gap. Shocks interact with denser matter of the disc, effectively increasing IR radiation, which boosts the pumping of the methanol masers. This model is strongly constrained by the geometry of the system (which is required to be in an almost edge-on projection) and could also generate time-lags between the peaks of flaring cloudlets. A chain of absorption and re-emission could slow down a pumping factor to subluminal velocity, but its magnitude is arguable. In Sect. 3.2 we estimate the velocity of the pumping factor to ∼1000 km s^{-1}, while the heatwave postulated by Burns et al. (2020) penetrates a disc plane much faster, with a significant fraction of the speed of light.

Comparison of the VLBI maser observations with continuum data (Patel et al. 2005) reveals that cluster II originates near the edge of a dust disc. The exposition of the masing cloudlets to the pumping IR photons from the disc could magnify the variability of the maser emission: an increase in the dust temperature boosts the flux of the pumping photons, which would increase the population-inverted abundance in cluster II, effectively raising the intensity of the masing cloudlets. Dust heats quickly (Johnstone et al. 2013), which, combined with the relaxation time of the maser, could result in the observed light curves. Previous studies (Cunningham et al. 2009) revealed that the Cep A HW2 system hosts many companion stars; thus, it is probable that an increase in dust temperature could be related to a companion star, modulating the accretion rate.

Using the NEOWISE survey (Mainzer et al. 2011), we might check whether or not the IR flux changes over time and whether or not it correlates with the 6.7 GHz maser emission; Olech et al. (2020, 2019) did this for periodic sources G107.298+5.639 and G59.533−0.192. However, Cep A HW2 is a crowded region, and WISE blends several sources. We therefore conclude that a higher angular resolution IR monitoring is required to resolve this case. This scenario also does not fully explain the observed time-lags. The resulting chain of absorption and re-emission (heatwave) should propagate with a velocity of several hundred km s^{-1} (see Sect. 3.2), which is too slow compared to the reported case (Burns et al. 2020). We note that the 2010 flare has been successfully modelled as an effect of Dicke's superradiance (Rajabi et al. 2019): in this scenario, flaring behaviour triggers when the critical inverted population column density is exceeded. This effect might impact the observed delays.

One might expect a driving pulse – induced for instance by the accretion luminosity burst – to affect all the maser cloudlets in Cep A HW2, but the response of different parts of the molecular disc is very different. One possible cause could be differences in the degree of saturation in maser cloudlets. Following Eq. (1) of Vlemmings et al. (2010), we attempt to estimate the ratio of the maser-stimulated emission rate R to the maser decay rate Γ, which is the measure of saturation level. For the beaming solid angle $\Delta\Omega \simeq 10^{-2}$, $\Gamma = 1$ s^{-1} and the maser brightness temperature from Tables A.1 and A.2, we obtain a saturation level ranging from 0.005 to 0.2 for most of the cloudlets composing the persistent features. For the −0.5 and −4.7 km s^{-1} cloudlets, R/Γ is 8×10^{-4} and 2×10^{-4}, respectively. It is therefore likely that the varying behaviour of the maser features, in response to the same driving factor, is related to the degree of saturation.

4.3. Causes of velocity drifts

The drift in the radial velocity of the redshifted emission is a particularly interesting phenomenon, showing a linear trend with the rate of 3–4 × 10^{-5} km s^{-1} d^{-1} for about 11.5 yr of our monitoring. It is striking that this rate is almost the same as that reported in the archetypal periodic source G9.62+0.20E (MacLeod et al. 2021). The profile of each of the two redshifted features is satisfactorily fitted with a single Gaussian for both the 32 m dish and EVN spectra; therefore we exclude a possibility that the observed systematic drifts are artifacts produced by variability of two or more spectral components with very close

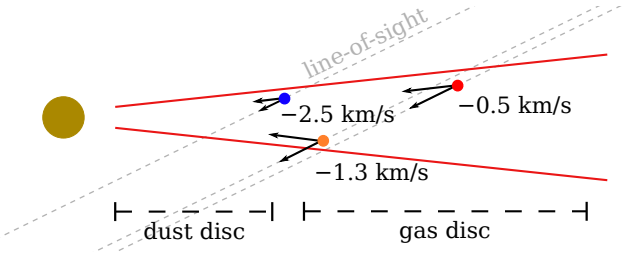

Fig. 10. Cartoon to illustrate the proposed scenario for infall motion in cluster II. The coloured circles denote the flaring cloudlets and the labels correspond to their velocities along the line of sight.

velocities. MacLeod et al. (2021) proposed two hypotheses to explain the velocity drifts; (i) precession of a Keplerian disc and (ii) infall motion. Adopting the disc model of Cep A HW2 from Sanna et al. (2017) and using the maser distribution from EVN observations (Fig. 3), in line with the approach of (MacLeod et al. 2021), we obtain a precession period of 870 yr. This value is more than an order of magnitude shorter than a putative period ($\sim 8 \times 10^4$ yr) of disc precession suggested from H_2 outflow observations (Cunningham et al. 2009), and therefore hypothesis (i) can be ruled out. There is observational evidence for infall motion of 6.7 GHz maser cloudlets with a velocity of $\sim 2\,\mathrm{km\,s^{-1}}$ in a plane of the accretion disc (Torstensson et al. 2011; Sanna et al. 2017). Our observations confirm the findings of these latter authors and suggest infall of the most redshifted cloudlets with a velocity of $4\,\mathrm{km\,s^{-1}}$ (Sect. 3.2). As circumstellar discs reach number densities higher than $10^9\mathrm{cm}^{-3}$ (Vlemmings et al. 2010), the maser emission is unlikely to originate from the densest inner part of the disc. Thus, we propose a scenario (Fig. 10) in which the maser clouds are located near the upper and lower edges of the disc and follow infall motions directed into HW2, parallel to the edges. With this scheme, the radial velocity drift (Fig. 5) is due to cloudlets accelerating towards HW2. Furthermore, this picture is entirely consistent with the measured time-lags between the onset of the flares of -0.5 and $-1.3\,\mathrm{km\,s^{-1}}$ cloudlets (Table 2).

4.4. Anticorrelated variability

The synchronous anticorrelation between the features at -1.8, -2.6, -3.7, -4.1, and $-4.7\,\mathrm{km\,s^{-1}}$ was reported for the first time by Sugiyama et al. (2008). They monitored the target over ~ 3 months and found that since MJD 54 320, the flux density of the feature at $-4.9\,\mathrm{km\,s^{-1}}$ had increased by a factor of 3 over a timescale of 2.5 weeks, while that of $-2.7\,\mathrm{km\,s^{-1}}$ decreased by a factor of 1.5. Szymczak et al. (2014) revealed that the $-4.7\,\mathrm{km\,s^{-1}}$ feature increased in intensity by a factor of 8 since MJD 56 118. Our new data show another rapid five-fold increase of its amplitude since MJD 57 960 (Fig. 2). It is striking that the event of anticorrelated and synchronous variability reported by Szymczak et al. (2014) occurred 1798 d after that noticed by Sugiyama et al. (2008) and 1842 d before that observed here. These time intervals are very well in line with a periodicity of flares of the redshifted emission.

Figure 7 displays the flux densities of the features at -2.6, -4.1, and $-4.7\,\mathrm{km\,s^{-1}}$ plotted against each other. Red points originate from the period of MJD 56 057−56 347, which is almost the same as in Szymczak et al. (2014) (their Fig. 4), and the green points come from our new observations of MJD 57 862−58 851. There is a linear anticorrelation between the features at -2.6 and $-4.7\,\mathrm{km\,s^{-1}}$ in the first time-span, while we note a significant deviation from a linear relation in a second one. This suggests that the causes of this behaviour affect the optical depth of the masing cloud, resulting in a non-linear relation. There are also visible radial velocity drifts during these periods of activity (Fig. 9). A recent study (Sanna et al. 2017) indicated that the velocity field in Cep A HW2 has a Keplerian component; it therefore becomes possible to explain the anticorrelated variability with the scenario proposed by Elmegreen & Morris (1979); Cesaroni (1990); Szymczak et al. (2014): when the pump rate drops on one side of the Keplerian disc, the opposite side of it will be affected soon after the light-crossing time, resulting in synchronous anticorrelated changes in the flux density of red- and blueshifted emission. This scenario requires a nearly edge-on oriented disc, but the inclination angle is ∼64° (Sanna et al. 2017) in Cep A HW2, and this condition is only partially fulfilled.

5. Conclusions

We report the detection of the quasi-periodic high-relative-amplitude flares of the extremely redshifted ($V_{\mathrm{lsr}} > -1.5\,\mathrm{km\,s^{-1}}$) 6.7 GHz methanol maser emission in Cep A HW2. The flares occur at ∼1800-day intervals and originate from the maser cluster closest to the presumed position of the protostar, near the edge of the dust disc. The spatial distribution of the flaring cloudlets, the radial velocity drift, and the time-lags of the flare peaks are consistent with a scenario of a molecular disc rotating with subKeplerian velocity and an infall motion component. Presumably, periodic and minor changes in the luminosity of the powering system result in significant variations of emission from unsaturated maser regions at the extreme redshifted velocities. Still, these changes do not significantly affect the most persistent maser emission regions approaching saturation state. The measured time-lags imply that changes in physical conditions that cause maser flares propagate at $\sim 1000\,\mathrm{km\,s^{-1}}$. Evidence of time-lags is against the alternative hypothesis that the flaring activity is caused by the amplification of variable background radiation from the radio jet. Synchronous anticorrelated changes in the flux densities of the -2.6 and $-4.7\,\mathrm{km\,s^{-1}}$ spectral components occur at approximately five-year intervals and suggest radiative interaction between the different parts of the molecular disc. Further long-term studies of the target are needed to confirm the maser periodicity and explain its origin.

Acknowledgements. The 32 m radio telescope is operated by the Institute Astronomy, Nicolaus Copernicus University and supported by the Polish Ministry of Science and Higher Education SpUB grant. We thank the staff and students for assistance with the observations. The research has made use of the SIMBAD data base, operated at CDS (Strasbourg, France), as well as NASA's Astrophysics Data System Bibliographic Services. This research made use of Astropy (`http://www.astropy.org`), a community-developed core Python package for Astronomy (Astropy Collaboration 2013, 2018). M.O. thanks the Ministry of Education and Science of the Republic of Poland for support and granting funds for the Polish contribution to the International LOFAR Telescope (arrangement no 2021/WK/02) and for maintenance of the LOFAR PL-612 Baldy (MSHE decision no. 59/E-383/SPUB/SP/2019.1)

References

Astropy Collaboration (Robitaille, T. P., et al.) 2013, A&A, 558, A33
Astropy Collaboration (Price-Whelan, A. M., et al.) 2018, AJ, 156, 123
Breen, S. L., Fuller, G. A., Caswell, J. L., et al. 2015, MNRAS, 450, 4109
Burns, R. A., Sugiyama, K., Hirota, T., et al. 2020, Nat. Astron., 4, 506
Carrasco-González, C., Sanna, A., Rodríguez-Kamenetzky, A., et al. 2021, ApJ, 914, L1
Cesaroni, R. 1990, A&A, 233, 513
Cragg, D. M., Sobolev, A. M., & Godfrey, P. D. 2005, MNRAS, 360, 533

Cunningham, N. J., Moeckel, N., & Bally, J. 2009, ApJ, 692, 943
Curiel, S., Ho, P. T. P., Patel, N. A., et al. 2006, ApJ, 638, 878
Durjasz, M., Szymczak, M., & Olech, M. 2019, MNRAS, 485, 777
Elmegreen, B. G., & Morris, M. 1979, ApJ, 229, 593
Fontani, F., Cesaroni, R., & Furuya, R. S. 2010, A&A, 517, A56
Fujisawa, K., Takase, G., Kimura, S., et al. 2014, PASJ, 66, 78
Gallimore, J. F., Cool, R. J., Thornley, M. D., & McMullin, J. 2003, ApJ, 586, 306
Goedhart, S., Gaylard, M. J., & van der Walt, D. J. 2003, MNRAS, 339, L33
Goedhart, S., Gaylard, M. J., & van der Walt, D. J. 2004, MNRAS, 355, 553
Goedhart, S., Langa, M. C., Gaylard, M. J., & Van Der Walt, D. J. 2009, MNRAS, 398, 995
Green, J. A., Caswell, J. L., Fuller, G. A., et al. 2010, MNRAS, 409, 913
Hu, B., Menten, K. M., Wu, Y., et al. 2016, ApJ, 833, 18
Hughes, V. A., & Wouterloot, J. G. A. 1984, ApJ, 276, 204
Hunter, T. R., Brogan, C. L., MacLeod, G. C., et al. 2018, ApJ, 854, 170
Inayoshi, K., Hosokawa, T., & Omukai, K. 2013a, MNRAS, 431, 3036
Inayoshi, K., Sugiyama, K., Hosokawa, T., Motogi, K., & Tanaka, K. E. I. 2013b, ApJ, 769, L20
Johnstone, D., Hendricks, B., Herczeg, G. J., & Bruderer, S. 2013, ApJ, 765, 133
Keimpema, A., Kettenis, M. M., Pogrebenko, S. V., et al. 2015, Exp. Astron., 39, 259
Ladeyschikov, D. A., Bayandina, O. S., & Sobolev, A. M. 2019, AJ, 158, 233
Lew, B. 2018, Exp. Astron., 45, 81
MacLeod, G. C., Chibueze, J. O., Sanna, A., et al. 2021, MNRAS, 500, 3425
Mainzer, A., Bauer, J., Grav, T., et al. 2011, ApJ, 731, 53
Maswanganye, J. P., van der Walt, D. J., Goedhart, S., & Gaylard, M. J. 2016, MNRAS, 456, 4335
Menten, K. M. 1991, ApJ, 380, L75
Moscadelli, L., Reid, M. J., Menten, K. M., et al. 2009, ApJ, 693, 406
Moscadelli, L., Sanna, A., Goddi, C., et al. 2017, A&A, 600, L8
Olech, M., Szymczak, M., Wolak, P., Sarniak, R., & Bartkiewicz, A. 2019, MNRAS, 486, 1236
Olech, M., Szymczak, M., Wolak, P., Gérard, E., & Bartkiewicz, A. 2020, A&A, 634, A41
Pandian, J. D., Goldsmith, P. F., & Deshpande, A. A. 2007, ApJ, 656, 255
Parfenov, S. Y., & Sobolev, A. M. 2014, MNRAS, 444, 620
Patel, N. A., Curiel, S., Sridharan, T. K., et al. 2005, Nature, 437, 109
Pietka, M., Fender, R. P., & Keane, E. F. 2015, MNRAS, 446, 3687
Rajabi, F., Houde, M., Bartkiewicz, A., et al. 2019, MNRAS, 484, 1590
Rodriguez, L. F., Garay, G., Curiel, S., et al. 1994, ApJ, 430, L65
Sanna, A., Moscadelli, L., Surcis, G., et al. 2017, A&A, 603, A94
Sobolev, A. M., Cragg, D. M., & Godfrey, P. D. 1997, A&A, 324, 211
Sugiyama, K., Fujisawa, K., Doi, A., et al. 2008, PASJ, 60, 1001
Sugiyama, K., Fujisawa, K., Doi, A., et al. 2014, A&A, 562, A82
Szymczak, M., Hrynek, G., & Kus, A. J. 2000, A&AS, 143, 269
Szymczak, M., Wolak, P., Bartkiewicz, A., & van Langevelde, H. J. 2011, A&A, 531, L3
Szymczak, M., Wolak, P., Bartkiewicz, A., & Borkowski, K. M. 2012, Astron. Nachr., 333, 634
Szymczak, M., Wolak, P., & Bartkiewicz, A. 2014, MNRAS, 439, 407
Szymczak, M., Olech, M., Wolak, P., Bartkiewicz, A., & Gawroński, M. 2016, MNRAS, 459, L56
Szymczak, M., Olech, M., Sarniak, R., Wolak, P., & Bartkiewicz, A. 2018, MNRAS, 474, 219
Torrelles, J. M., Gomez, J. F., Rodriguez, L. F., et al. 1996, ApJ, 457, L107
Torrelles, J. M., Patel, N. A., Gómez, J. F., et al. 2001, Nature, 411, 277
Torrelles, J. M., Patel, N. A., Curiel, S., et al. 2011, MNRAS, 410, 627
Torstensson, K. J. E., van Langevelde, H. J., Vlemmings, W. H. T., & Bourke, S. 2011, A&A, 526, A38
van der Walt, D. J. 2011, AJ, 141, 152
Virtanen, P., Gommers, R., Oliphant, T. E., et al. 2020, Nat. Methods, 17, 261
Vlemmings, W. H. T. 2008, A&A, 484, 773
Vlemmings, W. H. T., Surcis, G., Torstensson, K. J. E., & van Langevelde, H. J. 2010, MNRAS, 404, 134
Yang, K., Chen, X., Shen, Z.-Q., et al. 2017, ApJ, 846, 160

Appendix A: Spot tables

Table A.1. List of 6.7 GHz CH_3OH maser spots detected in epoch 8.

Cluster	$\Delta\alpha$ (mas)	$\Delta\delta$ (mas)	V_{lsr} (km s^{-1})	F_{peak} (Jy beam^{-1})	T_b (K)
II	−207.86 ± 0.10	−192.23 ± 0.08	−0.2	0.15	5.1×10^{7}
II	−208.36 ± 0.07	−192.01 ± 0.05	−0.2	0.28	9.2×10^{7}
II	−208.63 ± 0.06	−192.35 ± 0.05	−0.3	0.35	1.2×10^{8}
II	−208.92 ± 0.06	−192.37 ± 0.04	−0.3	0.41	1.4×10^{8}
II	−209.32 ± 0.06	−192.36 ± 0.03	−0.4	0.43	1.4×10^{8}
II	−208.91 ± 0.20	−191.45 ± 0.10	−0.4	0.37	1.2×10^{8}
II	−209.88 ± 0.07	−191.60 ± 0.04	−0.5	0.33	1.1×10^{8}
II	−209.93 ± 0.07	−191.63 ± 0.04	−0.5	0.29	9.5×10^{7}
II	−210.19 ± 0.09	−191.56 ± 0.04	−0.5	0.21	7.0×10^{7}
II	−210.73 ± 0.10	−191.34 ± 0.05	−0.6	0.15	4.8×10^{7}
II	−210.76 ± 0.12	−191.11 ± 0.06	−0.6	0.11	3.6×10^{7}
II	−211.31 ± 0.21	−191.72 ± 0.09	−0.7	0.07	2.2×10^{7}
II	−195.58 ± 0.40	−175.68 ± 0.21	−1.0	0.03	1.1×10^{7}
II	−194.95 ± 0.47	−175.16 ± 0.20	−1.0	0.04	1.2×10^{7}
II	−195.78 ± 0.36	−174.66 ± 0.21	−1.1	0.06	1.8×10^{7}
II	−210.91 ± 0.15	−169.01 ± 0.08	−1.2	0.09	3.0×10^{7}
II	−211.75 ± 0.12	−168.57 ± 0.06	−1.3	0.15	5.0×10^{7}
II	−211.05 ± 0.10	−168.60 ± 0.05	−1.3	0.19	6.1×10^{7}
II	−212.23 ± 0.12	−167.98 ± 0.06	−1.4	0.22	7.3×10^{7}
II	−214.14 ± 0.25	−166.91 ± 0.10	−1.4	0.23	7.6×10^{7}
I	−517.79 ± 0.05	−69.56 ± 0.02	−1.5	0.87	2.9×10^{8}
I	−517.89 ± 0.03	−68.99 ± 0.01	−1.5	1.41	4.7×10^{8}
I	−517.83 ± 0.02	−68.50 ± 0.01	−1.6	2.16	7.1×10^{8}
I	−518.03 ± 0.03	−66.28 ± 0.02	−1.6	5.23	1.7×10^{9}
I	−517.76 ± 0.01	−65.30 ± 0.01	−1.6	8.29	2.7×10^{9}
I	−517.80 ± 0.01	−65.81 ± 0.01	−1.7	12.30	4.1×10^{9}
I	−518.33 ± 0.02	−65.79 ± 0.01	−1.7	13.07	4.3×10^{9}
I	−518.44 ± 0.02	−65.47 ± 0.01	−1.8	15.41	5.1×10^{9}
I	−518.76 ± 0.01	−65.75 ± 0.01	−1.8	13.99	4.6×10^{9}
I	−519.00 ± 0.02	−65.84 ± 0.01	−1.9	9.05	3.0×10^{9}
I	−518.69 ± 0.02	−65.82 ± 0.01	−1.9	4.72	1.6×10^{9}
I	−518.53 ± 0.05	−65.82 ± 0.02	−1.9	1.41	4.7×10^{8}
I	−587.29 ± 0.03	−17.73 ± 0.01	−2.2	6.78	2.2×10^{9}
I	−587.76 ± 0.02	−16.95 ± 0.01	−2.2	23.42	7.8×10^{9}
I	−589.13 ± 0.02	−16.39 ± 0.01	−2.3	46.93	1.6×10^{10}
I	−590.42 ± 0.03	−15.96 ± 0.01	−2.3	71.28	2.4×10^{10}
I	−591.24 ± 0.03	−15.39 ± 0.01	−2.3	69.22	2.3×10^{10}
I	−592.50 ± 0.03	−14.46 ± 0.01	−2.4	56.08	1.9×10^{10}
I	−594.28 ± 0.04	−13.29 ± 0.02	−2.4	32.95	1.1×10^{10}
I	−596.01 ± 0.05	−12.76 ± 0.02	−2.5	24.56	8.1×10^{9}
I	−599.76 ± 0.09	−11.26 ± 0.04	−2.5	13.67	4.5×10^{9}
I	−602.11 ± 0.07	−10.22 ± 0.04	−2.6	10.24	3.4×10^{9}
I	−602.80 ± 0.07	−9.79 ± 0.04	−2.6	7.69	2.5×10^{9}
I	−603.32 ± 0.12	−10.17 ± 0.05	−2.6	3.05	1.0×10^{9}
I	−624.95 ± 0.08	−2.75 ± 0.04	−2.6	4.50	1.5×10^{9}
I	−625.86 ± 0.04	−2.14 ± 0.02	−2.7	4.01	1.3×10^{9}
I	−627.00 ± 0.05	−1.81 ± 0.02	−2.7	2.00	6.6×10^{8}
I	−628.20 ± 0.03	−1.50 ± 0.01	−2.8	2.17	7.2×10^{8}
I	−628.53 ± 0.03	−1.15 ± 0.01	−2.8	1.75	5.8×10^{8}

Table A.1. continued.

Cluster	$\Delta\alpha$ (mas)	$\Delta\delta$ (mas)	V_{lsr} (km s^{-1})	F_{peak} (Jy beam^{-1})	T_b (K)
I	−629.03 ± 0.04	−0.87 ± 0.02	−2.9	0.70	2.3×10^8
I	−629.05 ± 0.06	−0.64 ± 0.03	−2.9	0.32	1.1×10^8
I	−629.31 ± 0.11	0.03 ± 0.05	−3.0	0.15	4.9×10^7
III	−762.95 ± 0.14	77.27 ± 0.07	−3.3	0.52	1.7×10^8
III	−763.00 ± 0.14	76.80 ± 0.08	−3.4	0.83	2.8×10^8
III	−762.65 ± 0.10	76.92 ± 0.05	−3.4	0.73	2.4×10^8
III	−763.27 ± 0.32	76.71 ± 0.16	−3.4	0.24	8.0×10^7
III	−773.07 ± 0.07	80.50 ± 0.04	−3.5	0.50	1.7×10^8
III	−773.72 ± 0.09	81.15 ± 0.06	−3.5	0.36	1.2×10^8
III	−827.92 ± 0.04	123.60 ± 0.02	−3.6	1.05	3.5×10^8
III	−828.07 ± 0.06	123.20 ± 0.03	−3.6	0.71	2.4×10^8
III	−827.79 ± 0.12	123.31 ± 0.06	−3.7	0.38	1.3×10^8
IV	813.92 ± 0.21	−209.73 ± 0.08	−3.7	0.19	6.4×10^7
IV	814.37 ± 0.11	−209.60 ± 0.04	−3.7	0.38	1.3×10^8
IV	814.40 ± 0.06	−209.63 ± 0.03	−3.8	0.85	2.8×10^8
IV	814.16 ± 0.05	−209.65 ± 0.02	−3.8	1.16	3.8×10^8
IV	812.40 ± 0.19	−209.93 ± 0.08	−3.9	0.37	1.2×10^8
IV	797.92 ± 0.03	−209.07 ± 0.01	−3.8	2.19	7.2×10^8
IV	796.50 ± 0.02	−209.10 ± 0.01	−3.9	3.33	1.1×10^9
IV	795.63 ± 0.03	−209.32 ± 0.01	−3.9	3.15	1.0×10^9
IV	795.38 ± 0.05	−209.77 ± 0.02	−4.0	3.74	1.2×10^9
IV	794.32 ± 0.05	−209.80 ± 0.02	−4.0	3.63	1.2×10^9
IV	794.30 ± 0.04	−209.85 ± 0.02	−4.1	4.18	1.4×10^9
IV	793.96 ± 0.05	−209.85 ± 0.02	−4.1	4.00	1.3×10^9
IV	793.71 ± 0.05	−209.66 ± 0.02	−4.1	3.92	1.3×10^9
IV	793.80 ± 0.04	−209.36 ± 0.02	−4.2	4.12	1.4×10^9
IV	794.41 ± 0.03	−208.86 ± 0.01	−4.3	1.98	6.6×10^8
IV	794.80 ± 0.04	−208.91 ± 0.02	−4.3	1.11	3.7×10^8
IV	795.05 ± 0.09	−208.78 ± 0.04	−4.4	0.38	1.3×10^8
IV	795.13 ± 0.13	−208.83 ± 0.07	−4.4	0.13	4.3×10^7
IV	796.75 ± 0.07	−224.11 ± 0.03	−3.9	1.46	4.8×10^8
IV	796.40 ± 0.04	−224.12 ± 0.02	−4.0	5.21	1.7×10^9
IV	797.03 ± 0.03	−223.85 ± 0.01	−4.0	6.09	2.0×10^9
IV	797.08 ± 0.03	−223.59 ± 0.01	−4.1	5.84	1.9×10^9
IV	796.71 ± 0.05	−223.70 ± 0.02	−4.1	3.80	1.3×10^9
IV	796.58 ± 0.06	−223.63 ± 0.03	−4.1	3.09	1.0×10^9
IV	796.23 ± 0.10	−223.64 ± 0.04	−4.2	1.49	4.9×10^8
V	−482.68 ± 0.39	548.40 ± 0.41	−4.3	0.14	4.7×10^7
V	−437.63 ± 0.28	596.95 ± 0.17	−4.3	0.18	5.8×10^7
V	−448.15 ± 0.27	583.80 ± 0.32	−4.4	0.13	4.4×10^7
V	−482.35 ± 0.28	547.95 ± 0.32	−4.4	0.13	4.2×10^7

Notes. Numbers in the first column refer to the cluster that the spot originates from (see figure 3). Columns 2 and 3 give the relative positions and uncertainties in Right Ascension and Declination, respectively. The fourth column shows the local-standard-of-rest velocity of the spot, the fifth column its peak flux density. The last column presents the brightness temperatures of each spot.

Table A.2. List of 6.7 GHz CH_3OH maser spots detected in epoch 9.

Cluster	$\Delta\alpha$ (mas)	$\Delta\delta$ (mas)	V_{lsr} ($km\,s^{-1}$)	F_{peak} ($Jy\,beam^{-1}$)	T_b (K)
II	−208.33 ± 0.07	−191.05 ± 0.10	−0.1	0.13	6.7×10^7
II	−208.23 ± 0.16	−190.07 ± 0.24	−0.1	0.06	2.9×10^7
II	−208.39 ± 0.04	−191.97 ± 0.06	−0.2	0.23	1.1×10^8
II	−208.60 ± 0.03	−192.39 ± 0.04	−0.3	0.29	1.4×10^8
II	−209.13 ± 0.04	−192.15 ± 0.04	−0.4	0.26	1.3×10^8
II	−209.83 ± 0.04	−191.80 ± 0.05	−0.5	0.19	9.6×10^7
II	−210.57 ± 0.06	−191.27 ± 0.07	−0.6	0.12	6.1×10^7
II	−211.20 ± 0.10	−191.00 ± 0.12	−0.7	0.06	2.9×10^7
I	−517.76 ± 0.02	−68.79 ± 0.01	−1.5	1.91	9.6×10^8
I	−517.66 ± 0.02	−67.43 ± 0.01	−1.6	6.72	3.4×10^9
I	−517.65 ± 0.01	−66.06 ± 0.01	−1.6	20.20	1.0×10^{10}
I	−517.80 ± 0.01	−65.81 ± 0.01	−1.7	35.25	1.8×10^{10}
I	−518.04 ± 0.02	−65.83 ± 0.01	−1.8	29.48	1.5×10^{10}
I	−518.24 ± 0.02	−65.89 ± 0.01	−1.9	11.80	5.9×10^9
I	−518.18 ± 0.05	−65.93 ± 0.03	−2.0	2.17	1.1×10^9
I	−556.77 ± 0.04	−34.17 ± 0.04	−2.1	3.84	1.9×10^9
I	−556.63 ± 0.09	−33.47 ± 0.09	−2.2	4.44	2.2×10^9
I	−572.04 ± 0.05	−49.10 ± 0.03	−2.0	2.83	1.4×10^9
I	−573.15 ± 0.07	−47.27 ± 0.04	−2.1	3.42	1.7×10^9
I	−587.18 ± 0.03	−17.36 ± 0.02	−2.2	23.16	1.2×10^{10}
I	−589.01 ± 0.02	−16.28 ± 0.01	−2.3	76.96	3.9×10^{10}
I	−590.81 ± 0.02	−15.21 ± 0.02	−2.3	112.29	5.6×10^{10}
I	−593.35 ± 0.03	−13.92 ± 0.02	−2.4	86.62	4.4×10^{10}
I	−598.13 ± 0.05	−11.75 ± 0.02	−2.5	38.25	1.9×10^{10}
I	−602.13 ± 0.04	−9.95 ± 0.02	−2.6	14.02	7.0×10^9
I	−603.01 ± 0.09	−9.28 ± 0.06	−2.7	2.49	1.3×10^9
I	−619.39 ± 0.09	−3.87 ± 0.04	−2.6	7.15	3.6×10^9
I	−623.67 ± 0.04	−2.46 ± 0.02	−2.7	7.57	3.8×10^9
I	−626.71 ± 0.03	−1.26 ± 0.02	−2.8	5.71	2.9×10^9
I	−628.29 ± 0.02	−0.28 ± 0.02	−2.9	2.49	1.3×10^9
I	−629.04 ± 0.04	0.53 ± 0.03	−3.0	0.59	3.0×10^8
I	−629.45 ± 0.24	1.43 ± 0.12	−3.0	0.08	3.9×10^7
III	−773.27 ± 0.03	80.12 ± 0.04	−3.5	1.43	7.2×10^8
III	−773.16 ± 0.03	80.00 ± 0.03	−3.5	1.45	7.3×10^8
III	−773.27 ± 0.05	79.07 ± 0.07	−3.6	1.11	5.6×10^8
III	−768.41 ± 0.07	85.20 ± 0.08	−3.1	0.13	6.7×10^7
III	−768.00 ± 0.03	83.58 ± 0.03	−3.2	0.61	3.0×10^8
III	−767.36 ± 0.04	81.46 ± 0.04	−3.3	0.85	4.3×10^8
III	−769.70 ± 0.13	80.52 ± 0.06	−3.4	0.69	3.5×10^8
III	−761.78 ± 0.03	76.31 ± 0.04	−3.5	1.11	5.6×10^8
III	−762.37 ± 0.05	78.85 ± 0.06	−3.2	0.38	1.9×10^8
III	−762.12 ± 0.02	77.39 ± 0.02	−3.3	1.60	8.0×10^8
III	−762.10 ± 0.02	76.73 ± 0.02	−3.4	2.18	1.1×10^9
III	−761.78 ± 0.03	76.32 ± 0.04	−3.5	1.11	5.6×10^8
III	−827.10 ± 0.07	124.00 ± 0.05	−3.5	0.79	4.0×10^8
III	−827.34 ± 0.04	123.36 ± 0.02	−3.6	2.40	1.2×10^9
III	−827.50 ± 0.04	122.77 ± 0.02	−3.7	2.52	1.3×10^9

Table A.2. continued

Cluster	$\Delta\alpha$ (mas)	$\Delta\delta$ (mas)	V_{lsr} (km s^{-1})	F_{peak} (Jy beam^{-1})	T_b (K)
III	−828.75 ± 0.09	121.56 ± 0.05	−3.7	1.14	5.7×10^{8}
III	−870.97 ± 0.04	196.99 ± 0.05	−3.6	1.40	7.0×10^{8}
III	−871.86 ± 0.04	197.33 ± 0.04	−3.7	1.88	9.4×10^{8}
III	−873.28 ± 0.07	198.00 ± 0.07	−3.7	0.91	4.6×10^{8}
IV	813.92 ± 0.06	−209.04 ± 0.03	−3.7	1.34	6.7×10^{8}
IV	814.42 ± 0.08	−208.86 ± 0.04	−3.8	1.78	9.0×10^{8}
IV	799.44 ± 0.04	−209.69 ± 0.03	−3.7	1.26	6.3×10^{8}
IV	798.33 ± 0.02	−209.50 ± 0.01	−3.8	6.58	3.3×10^{9}
IV	797.07 ± 0.02	−209.48 ± 0.01	−3.9	14.58	7.3×10^{9}
IV	796.05 ± 0.02	−209.56 ± 0.01	−4.0	19.96	1.0×10^{10}
IV	795.51 ± 0.02	−209.61 ± 0.01	−4.1	19.20	9.6×10^{9}
IV	795.41 ± 0.02	−209.50 ± 0.01	−4.2	13.44	6.8×10^{9}
IV	795.44 ± 0.01	−209.32 ± 0.01	−4.3	5.98	3.0×10^{9}
IV	795.34 ± 0.02	−209.07 ± 0.02	−4.4	1.62	8.1×10^{8}
IV	795.35 ± 0.05	−208.95 ± 0.04	−4.4	0.27	1.4×10^{8}
IV	796.09 ± 0.10	−224.76 ± 0.06	−3.8	1.49	7.5×10^{8}
IV	795.66 ± 0.03	−224.71 ± 0.02	−3.9	11.12	5.6×10^{9}
IV	795.72 ± 0.03	−224.53 ± 0.01	−4.0	21.93	1.1×10^{10}
IV	795.70 ± 0.03	−224.30 ± 0.01	−4.1	18.53	9.3×10^{9}
IV	795.14 ± 0.04	−224.10 ± 0.02	−4.2	8.82	4.4×10^{9}
IV	794.21 ± 0.06	−224.01 ± 0.03	−4.3	2.23	1.1×10^{9}
V	−423.83 ± 0.10	485.40 ± 0.09	−4.6	0.11	5.6×10^{7}
V	−425.20 ± 0.09	486.14 ± 0.09	−4.7	0.12	6.3×10^{7}
V	−426.98 ± 0.19	487.12 ± 0.19	−4.8	0.06	3.0×10^{7}

Notes. Numbers in the first column refer to the cluster that the spot originates from (see figure 3). Columns 2 and 3 give the relative positions and uncertainties in Right Ascension and Declination, respectively. The fourth column shows the local-standard-of-rest velocity of the spot, and the fifth column its peak flux density. The last column presents the brightness temperatures of each spot.

Table A.3. Cloudlet parameters derived from Gaussian function fitting.

Epoch	F_p (Jy beam^{-1})	V_p (km s^{-1})	FWHM (km s^{-1})
−0.5 km s^{-1} cloudlet			
7	0.89 ± 0.02	−0.462 ± 0.003	0.33 ± 0.01
8	0.42 ± 0.02	−0.377 ± 0.005	0.34 ± 0.01
9	0.28 ± 0.01	−0.355 ± 0.004	0.40 ± 0.01
−1.3 km s^{-1} cloudlet			
7	0.24 ± 0.01	−1.177 ± 0.002	0.18 ± 0.01
8	0.23 ± 0.01	−1.405 ± 0.022	0.28 ± 0.04
−1.7 km s^{-1} cloudlet			
5	11.85 ± 0.11	−1.740 ± 0.001	0.27 ± 0.01
6	23.17 ± 0.69	−1.746 ± 0.002	0.20 ± 0.01
7	36.82 ± 1.41	−1.745 ± 0.002	0.21 ± 0.01
8	14.98 ± 0.99	−1.746 ± 0.005	0.24 ± 0.01
9	32.73 ± 2.99	−1.742 ± 0.006	0.26 ± 0.01
−2.6 km s^{-1} cloudlet			
5	19.19 ± 0.28	−2.491 ± 0.002	0.30 ± 0.01
6	45.51 ± 0.83	−2.460 ± 0.002	0.24 ± 0.01
7	116.32 ± 1.83	−2.443 ± 0.001	0.23 ± 0.01
8	67.48 ± 16.49	−2.317 ± 0.009	0.17 ± 0.01
	16.43 ± 7.98	−2.460 ± 0.097	0.25 ± 0.10
9	97.50 ± 84.55	−2.326 ± 0.055	0.22 ± 0.04
	32.34 ± 72.41	−2.460 ± 0.222	0.25 ± 0.13
−2.7 km s^{-1} cloudlet			
5	6.95 ± 0.05	−2.739 ± 0.002	0.28 ± 0.01
6	6.95 ± 0.06	−2.729 ± 0.002	0.25 ± 0.01
7	9.23 ± 0.08	−2.717 ± 0.002	0.25 ± 0.01
8	3.63 ± 0.96	−2.663 ± 0.059	0.27 ± 0.06
9	7.93 ± 0.29	−2.684 ± 0.008	0.28 ± 0.01
−3.4 km s^{-1} cloudlet			
5	1.16 ± 0.01	−3.430 ± 0.004	0.31 ± 0.01
6	1.93 ± 0.07	−3.426 ± 0.003	0.18 ± 0.01
7	2.87 ± 0.09	−3.413 ± 0.003	0.17 ± 0.01
8	0.90 ± 0.06	−3.361 ± 0.003	0.12 ± 0.01
9	2.24 ± 0.03	−3.381 ± 0.001	0.20 ± 0.00
−3.6 km s^{-1} cloudlet			
5	5.32 ± 0.07	−3.676 ± 0.002	0.27 ± 0.01
6	5.16 ± 0.27	−3.667 ± 0.004	0.19 ± 0.01
7	5.20 ± 0.18	−3.646 ± 0.003	0.20 ± 0.01
8	1.22 ± —	−3.521 ± —	0.21 ± —
9	2.79 ± 0.10	−3.625 ± 0.003	0.21 ± 0.01
−4.0 km s^{-1} cloudlet #1			
5	12.87 ± 0.09	−4.089 ± 0.001	0.36 ± 0.01
6	11.71 ± 0.48	−4.078 ± 0.004	0.33 ± 0.01
7	15.06 ± 0.47	−4.097 ± 0.002	0.28 ± 0.01
8	4.77 ± 0.48	−4.034 ± 0.011	0.37 ± 0.02
9	22.02 ± 1.01	−4.052 ± 0.003	0.32 ± 0.01
−4.0 km s^{-1} cloudlet #2			
5	8.47 ± 0.57	−4.203 ± 0.011	0.25 ± 0.01
	5.91 ± 0.54	−4.003 ± 0.012	0.22 ± 0.02
6	9.27 ± 0.06	−4.190 ± 0.001	0.17 ± 0.01
	11.06 ± 0.04	−4.022 ± 0.001	0.16 ± 0.01
7	25.80 ± 1.40	−4.060 ± 0.004	0.22 ± 0.01
8	6.23 ± 0.69	−4.040 ± 0.009	0.18 ± 0.02
9	22.55 ± 1.78	−4.051 ± 0.006	0.23 ± 0.01
−4.7 km s^{-1} cloudlet			
5	0.95 ± 0.01	−4.711 ± 0.002	0.27 ± 0.01
6	0.57 ± 0.01	−4.716 ± 0.002	0.17 ± 0.01
7	0.42 ± 0.01	−4.715 ± 0.003	0.18 ± 0.01
9	0.13 ± —	−4.680 ± —	0.22 ± —

Notes. The first column presents epochs (listed in Table 1). Columns 2 – 4 show parameters derived from fitting the peak flux density, the peak velocity relative to the local standard of rest, and the full width at half maximum. The uncertainties provided are derived from the covariance matrix.

Appendix B: Cluster II maps across 9 epochs

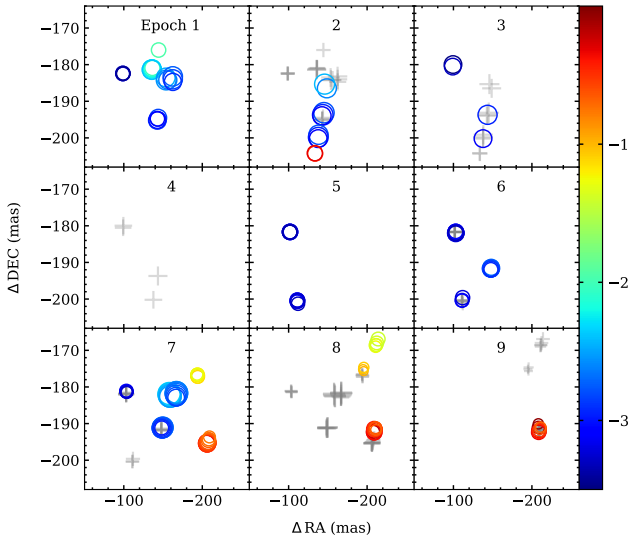

Fig. B.1. Spatial distribution of the CH_3OH maser spots in Cep A HW2 in cluster II across nine epochs. Epoch numbers presented at the top of the graphs are listed in Table 1. The sizes of the symbols are proportional to the logarithm of the spot peak flux densities. Grey crosses denote the spatial distribution of the emission in the previous epoch.

A&A 661, A114 (2022)
https://doi.org/10.1051/0004-6361/202243108
© ESO 2022

Astronomy & Astrophysics

Detection of periodic flares in 6.7 GHz methanol masers G45.804−0.356 and G49.043−1.079⋆

M. Olech[1], M. Durjasz[2], M. Szymczak[2], and A. Bartkiewicz[2]

[1] Space Radio-Diagnostic Research Center, Faculty of Geoengineering, University of Warmia and Mazury ul.Oczapowskiego 2, 10-719 Olsztyn, Poland
e-mail: mateusz.olech@uwm.edu.pl
[2] Institute of Astronomy, Faculty of Physics, Astronomy and Informatics, Nicolaus Copernicus University, Grudziadzka 5, 87-100 Torun, Poland

Received 13 January 2022 / Accepted 11 March 2022

ABSTRACT

Context. Periodicity in 6.7 GHz methanol maser sources is a rare phenomenon that was discovered during long-term monitoring programmes. Understanding the underlying processes that lead to periodic variability might provide insights into the physical processes in high-mass star-forming regions.
Aims. We aim to identify and describe new periodic methanol masers.
Methods. The observations were obtained with the Torun 32 m antenna. Time series analysis was conducted using well-proven statistical methods. Additionally, NEOWISE data were used to search for a correlation between infrared and maser fluxes.
Results. We found two new periodic sources, G45.804−0.356 and G49.043−1.079, with periods of 416.9 and 469.3 days, respectively. For G49.043−1.079, infrared variability is simultaneous with methanol flares.
Conclusions. A most likely cause of the periodicity in G49.043−1.079 is modulated accretion. For G45.804−0.356, the periodicity cannot be explained with the available data, and further research is needed.

Key words. masers – stars: formation – ISM: clouds – radio lines: ISM

1. Introduction

Emission of class II 6.7 GHz methanol maser lines is a well-known tracer of high-mass star-forming regions (Menten 1991; Breen et al. 2015; Ellingsen 2006; Pandian et al. 2007; Szymczak et al. 2012). It is radiatively pumped by mid-infrared photons emitted by dust grains in the local environment (Cragg et al. 2005; Urquhart et al. 2015). Milliarcsecond imaging of 6.7 GHz sources shows that emission arises in most cases from regions of an interface between the protostellar disc and envelope at a typical distance of ∼1000 au from a protostar with individual maser cloudlets of size ∼10 au (Goddi et al. 2011; Bartkiewicz et al. 2016). The 6.7 GHz line is sensitive to the local physical conditions, and its location makes it a perfect tool for studying processes during this early stage of high-mass star formation. Recent studies of strong methanol maser flares have shown that observations of this line can be used to detect early stages of accretion bursts in massive protostars (Moscadelli et al. 2017; Hunter et al. 2018; Burns et al. 2020).

Several long-term monitoring programmes have been conducted since the discovery of this transition (Goedhart et al. 2004; Szymczak et al. 2018). One of their most surprising results was the identification of a small group of 26 sources that show periodic behaviour (e.g. Goedhart et al. 2003; Maswanganye et al. 2015; Szymczak et al. 2011; Sugiyama et al. 2017). The periods range from 24 to 670 days, with most sources having periods between 100 and 300 days. The variety in flare profiles and periods has led to a number of competing hypotheses on the nature of this process. Some models, such as the colliding wind binary (CWB) model, consider changes in the seed photon flux to be the primary driving mechanism (van der Walt et al. 2009; van der Walt 2011). Others consider the change in the pumping efficiency to be the main mechanism responsible for flares, such as pulsating protostars due to high accretion (Inayoshi et al. 2013), a binary system with spiral shocks (Parfenov & Sobolev 2014), or modulated accretion in binaries (Araya et al. 2010). Although these models were successfully applied to some known sources, there is no clear consensus on the general mechanism of periodicity. Furthermore, Morgan et al. (2021) have shown that the orientation of the disc-outflow system in the plane of the sky might have a significant impact on observed flare profiles. The recent discovery of anti-correlated flares of 6.7 GHz methanol and 22 GHz water vapour maser lines in G107.298+5.639 and the synchronicity of infrared (IR) and methanol flares in two sources (Szymczak et al. 2015; Olech et al. 2020) is strong evidence for pumping mechanism modulation being a leading cause.

Nevertheless, testing current theories is limited by the small number of sources. Extending the list of periodic masers is crucial for facilitating this work. Therefore, monitoring programmes of methanol masers are valuable as they can lead to the identification of new periodic sources (Sugiyama et al. 2018; Szymczak et al. 2018; Olech et al. 2019).

In this paper, we report the discovery of periodicity in another two 6.7 GHz methanol maser sources: G45.804−0.356 and G49.043−1.079[1].

⋆ Data are only available at the CDS via anonymous ftp to cdsarc.u-strasbg.fr (130.79.128.5) or via http://cdsarc.u-strasbg.fr/viz-bin/cat/J/A+A/661/A114

[1] The names are the Galactic coordinates.

2. Observations and methodology

Both targets were observed with the Torun 32 m antenna as part of an ongoing long-term monitoring programme of methanol maser sources (Szymczak et al. 2018). G45.804−0.356 (RA = $19^h16^m31^s.08$, Dec = 11°16′12″.0 (J2000)) was observed from June 2009 to October 2021, with a cadence of 1.8 observations per month. For G49.043−1.079 (RA = $19^h25^m22^s.20$, Dec = 13°47′19″.5 (J2000)), monitoring started in April 2016 and ended in November 2021, with a cadence of 2.4 observations per month. Coordinates used for the observations were taken from Breen et al. (2015).

Scans at the rest frequency of 6668.519 MHz were obtained with the frequency-switching mode. The auto-correlator banks were configured with 4196 channels for the 4 MHz band per circular polarization. This yielded a spectral resolution of 0.09 km s^{-1} after Hanning smoothing. The system equivalent flux density was measured by observing the strong continuum source 3C123. Furthermore, daily sensitivity variations were calibrated by observing the maser source G32.744−0.076, which has known stable features. This scheme had been successfully used in previous studies. We estimate the error of flux calibrations to be 10%.

Before May 2015, the typical system temperature (T_{sys}) was 50 K with $3\sigma_{rms}$ of ∼1.2 Jy for observations consisting of 45 scans of 30 s duration each. In May 2015, the new 6.7 GHz receiver was installed on the antenna, and the average system temperature – lowered to 30 K with a $3\sigma_{rms}$ of ∼0.9 Jy – could be achieved after only 30 scans. During data reduction, observations with T_{sys} much higher than typical as well as observations contaminated with Radio Frequency Interference (RFI) or instrumental effects were rejected.

In this work, we also used the NEOWISE 2021 Data Release (Mainzer et al. 2011, 2014; Cutri et al. 2015). We used a cone search with a radius of 5″ around source positions. To ensure high quality, we discarded all measurements with *ph_qual* other than "A", *cc_flags* other than 0, and all *qual_frame* = 0. In total, 190 measurements for G45.804−0.356 and 176 for G49.043−1.079 were used for the analysis.

Time series analysis

A time series of individual spectral features was extracted as the velocity integrated flux. Before analysis, all non-periodic trends were removed by fitting the polynomial to the lower envelope of the time series using the least squares method and then subtracting it. The periodicity was estimated by calculating the Lomb–Scargle (L–S) periodogram (Scargle 1982) using the Astropy Python library (Astropy Collaboration 2013, 2018) and with a simple analysis of variance (AoV) implementation (Schwarzenberg-Czerny 1989). The period value was calculated by fitting the Gaussian function to the L–S and AoV maxima, and the error was estimated as its full width at half maximum (FWHM). With the acquired period, the time series was then phased and binned. An asymmetric periodic power function given by the equation

$$S(t) = D * \exp(s(t)) + C,$$
$$\text{where } s(t) = -b\cos(\omega t + \phi)/(1 - f\sin(\omega t + \phi)) + a,$$

was fitted to these data. Here, a, b, C, and D are constants and $\omega = 2\pi/P$, where P is the period, ϕ is the phase, and f is the asymmetry parameter (Szymczak et al. 2011). For phased data, we assumed $P = 1$.

Average characteristics of the flare, such as the relative amplitude, the flare FWHM, and the rise-to-decay ratio, were estimated from this fitted function. The time lag between the features was calculated using the discrete correlation function (DCF; Edelson & Krolik 1988). Lag estimation was done by fitting the quadratic function to the maximum of the DCF. Error estimation of all values was done using the Monte Carlo method.

3. Results

Results of the analysis are summarized in Fig. 1 and Table 1.

G45.804−0.356. The spectrum of this source consists of one strong feature at 59.94 km s^{-1} and several weak ones in a velocity range from 55 to 71 km s^{-1} (Fig. 2). From those weak features, only one, at 69.29 km s^{-1}, was strong enough to be included in the analysis. Both this and the strong feature show periodic flares with an average L-S period of 416.9 days, an AoV period of 419.8 days, and a FWHM of 203.6 days. The flare profiles are asymmetric, with rise-to-decay time ratios, R_{rd}, of 0.69 and 0.66, respectively, a small relative amplitude of <0.37, and no obvious quiescence period. No time lag measurements were carried out because the feature at 69.26 km s^{-1} is faint and flares with a small amplitude. During the monitoring period, no visible changes in the spectral distribution or flare amplitude were visible. We found no significant variations in flux in the IR data (Fig. 3).

G49.043−1.079. The entire spectral structure of the source with emission in velocities from 35 to 41 km s^{-1} shows periodic variations (Fig. 4). Due to the complex structure and velocity drifts of the blended features in velocities between 36 and 38 km s^{-1}, the entire range was integrated as a single feature and omitted in further statistics. The periodic analysis resulted in an average L-S period of 469.3 days and an AoV period of 466.9 days. Features at 35.60 km s^{-1} and 37.01 km s^{-1} show asymmetric flare profiles, with R_{rd} of 0.53 and 0.20. The remaining features have symmetric flares within the margin of errors. The average length of the FWHM of the flares is 153.7 days, and relative amplitudes are as high as 6.16 in the 40.83 km s^{-1} feature. Measured time lags with respect to the 38.41 km s^{-1} feature range from 2.8 to 67.7 days. A visual inspection of the time series revealed variations in the shape and amplitudes between the individual flares. There is a visible quiescence period between flares in all features except that at 37.01 km s^{-1}. A phased light curve from NEOWISE data (Fig. 3) shows an IR flare simultaneous to the 6.7 GHz variability.

4. Discussion

Most of the 26 previously known periodic maser sources have periods that vary between 100 and 300 days. Only four objects showed periods longer than 400 days (Olech et al. 2019, Table A3). The two sources presented in this paper, with periods 416.9 and 469.3 days, extend this small group and increase the total number to 28 sources.

In both cases, the quality of the flare profile analysis and the precision of the period estimation are limited by a relatively short observation period. For G45.804−0.356, the limiting factors are low flare amplitude and a high scatter of data before ∼57 300 MJD. In G49.043−1.079, the observation period covers only four obvious flares, with the first being much weaker than the last three. On the other hand, the flare asymmetry

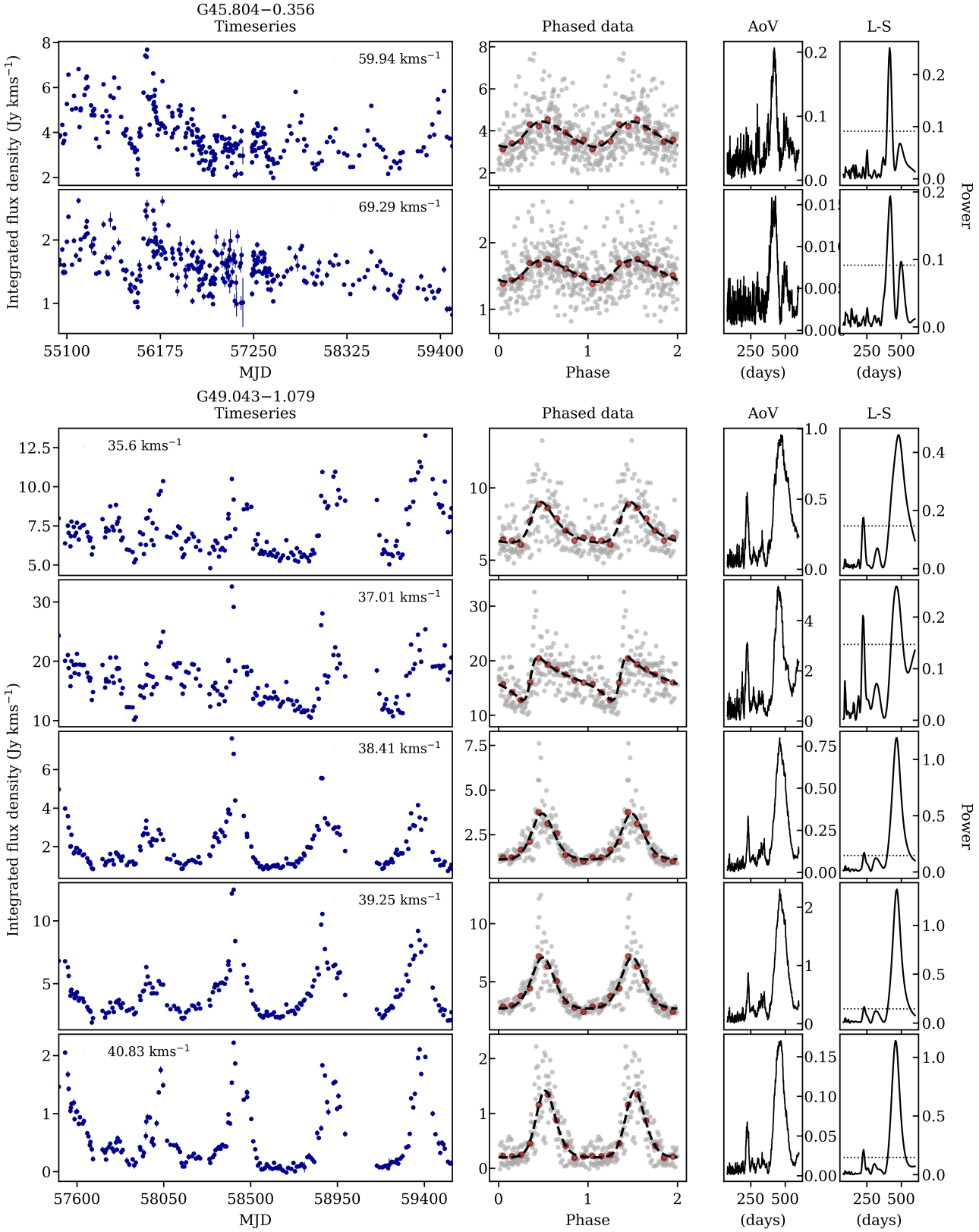

Fig. 1. Periodic behaviour of both 6.7 GHz sources. Panels in the leftmost column show the time series of spectral features. In the second column, grey points represent time series phased to the calculated period, red points show data binned with 0.1 phase intervals, and dashed black lines show the fitted asymmetric periodic power function. The third and fourth columns respectively show AoV and L–S periodograms. The dotted line in the last column represents the 1% false alarm probability level.

of the 35.6 km s^{-1} feature could result from less pronounced variability at the beginning of the observation period and the influence of blended emission. The 37.01 km s^{-1} feature shows an asymmetrical profile with flares that last much longer. Strong

Table 1. Parameters obtained from periodic analysis.

V (km s^{-1})	$\overline{S}$ (Jy)	R	$P_{\rm LS}$ (days)	$P_{\rm AoV}$ (days)	FWHM (days)	$R_{\rm rd}$	τ (days)
G45.804−0.356							
59.94	13.47	0.37 (0.07)	416.76 (14.70)	418.80 (23.38)	199.00 (18.56)	0.69 (0.19)	–
69.29	2.25	0.23 (0.04)	416.95 (22.41)	420.70 (32.62)	208.28 (18.05)	0.66 (0.22)	–
G49.043−1.079							
35.60	14.34	0.45 (0.06)	480.64 (48.70)	474.30 (53.45)	148.20 (17.81)	0.53 (0.13)	67.7 (1.1)
37.01	14.08	0.61 (0.10)	467.96 (39.23)	459.41 (36.50)	233.76 (21.47)	0.20 (0.05)	16.7 (15.0)
38.41	4.42	2.31 (0.15)	468.18 (36.07)	468.72 (41.84)	133.78 (7.88)	0.87 (0.13)	0
39.25	6.26	1.63 (0.13)	468.53 (31.67)	470.45 (42.14)	137.82 (7.73)	0.97 (0.13)	2.8 (1.1)
40.83	1.14	6.16 (0.38)	461.02 (30.80)	461.37 (37.59)	115.75 (6.58)	0.81 (0.13)	14.0 (1.7)

Notes. V stands for the velocity of the spectral feature, $\overline{S}$ the average flux density during the observation period, R the relative flare amplitude calculated as $(S_{\rm max} - S_{\rm min})/(S_{\rm min})$, $P_{\rm LS}$ the period estimation using an L–S periodogram, $P_{\rm AoV}$ the period estimation using AoV, FWHM the timescale of the flare, $R_{\rm rd}$ the rise-to-decay ratio of the flare, and τ the time delay calculated with the DCF.

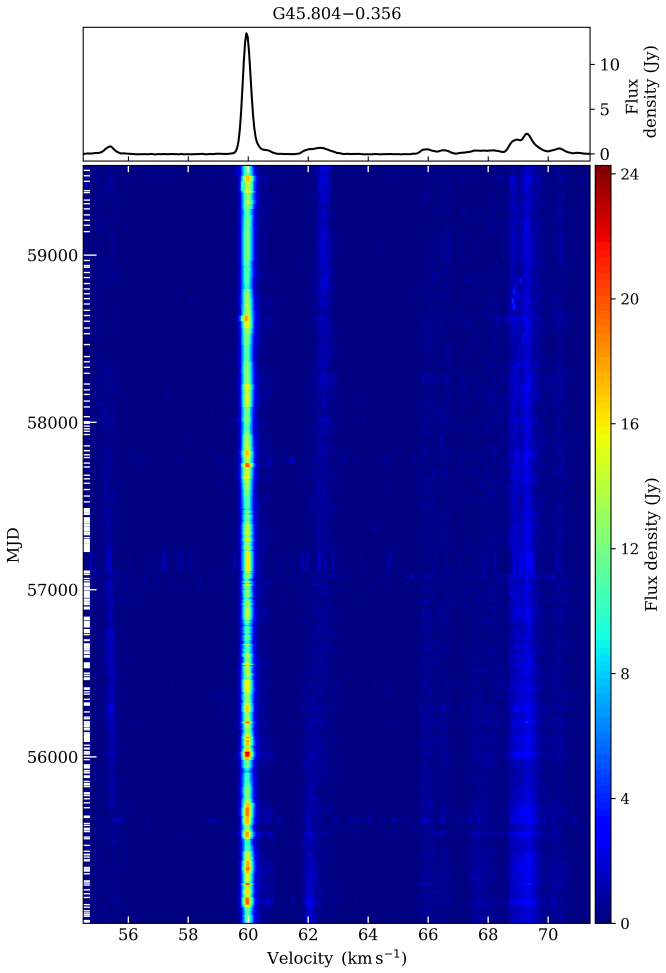

Fig. 2. Dynamic spectrum of G45.804−0.356. The velocity scale is relative to the local standard of rest. The horizontal bars in the left coordinate correspond to the dates of the observed spectra. The *top panel* shows the average spectrum from the whole observation period.

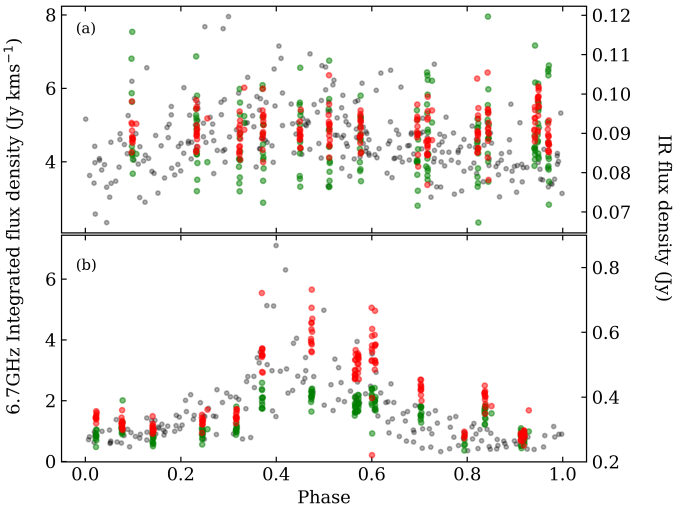

Fig. 3. Comparison between the phased 6.7 GHz line brightness and NEOWISE photometric data. Grey points show the methanol line for one of the chosen spectral features, green points represent 3.4 µm (W1), and red points 4.6 µm (W2). The W1 flux was scaled up by a factor of 6. *Panel a* shows the G45.804−0.356 flux at 59.94 km s^{-1}, and *panel b* the source G49.043−1.0.79 feature 38.41 km s^{-1}.

velocity drifts visible during the monitoring suggest that multiple maser cloudlets make up this emission. The resulting cumulative flare profile could be significantly different if the cloudlets flared with a slight time lag due to the line of sight effect. This possibility, combined with a small flare amplitude at the beginning of observations, is the most likely cause of this unusual profile. Continued monitoring will help better characterize the behaviour of both sources.

4.1. Source morphology

The 6.7 GHz emission of both sources was imaged by Hu et al. (2016) with the Very Large Array (VLA) in C configuration (maps from their work are presented in Fig. A.1). Although due to a short on-source time of 20 s and low resolution (beam size of 3″ × 6″) the position of individual maser cloudlets has a high error, these maps can provide us insights into the nature of these sources. The map of G45.804−0.356 includes only a part of the emission seen in single-dish spectra, with only the 59.94 km s^{-1} feature visible. A weak blue-shifted emission seen

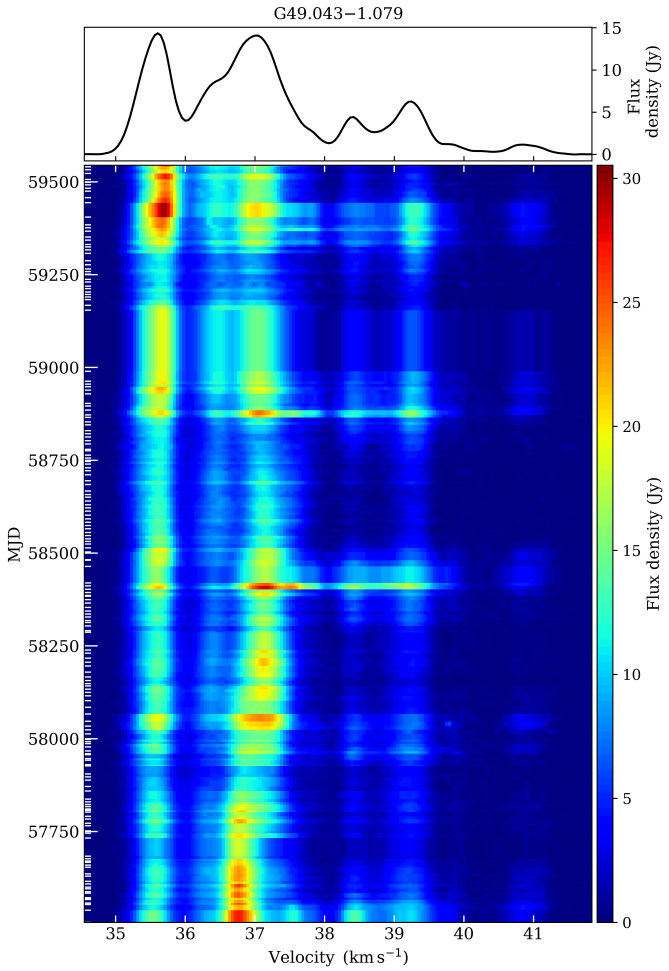

Fig. 4. Same as Fig. 2 but for G49.043−1.079.

at a distance of ∼ 1.3″ (i.e. >9000 au at a distance of $7.3^{+1.5}_{-1.0}$ kpc; Reid et al. 2019) most likely belongs to a different source. With this incomplete structure, it is impossible to analyse its morphology. Additionally, no continuum emission was detected with a limit of 45 μJy beam^{-1}. For source G49.043−1.079, all single-dish features were mapped, and a linear structure with a velocity gradient is visible. With a parallax distance of $6.1^{+0.9}_{-0.7}$ kpc (Reid et al. 2019) and an angular size of <0.3″, the emission has a linear size of ∼1800 au, which is consistent with typical 6.7 GHz maser source sizes. The structure of emission hints at edge-on disc morphology. A weak continuum emission of 0.23 mJy was detected in this source.

4.2. Periodicity causes

A number of hypotheses have been proposed to explain periodic behaviour in masers. Here we discuss them in the context of the presented sources.

The CWB model was proposed and successfully applied to a few sources by van der Walt (2011) and van der Walt et al. (2016). It considers a periodic wind interaction in binary systems that generates additional ionizing radiation waves. Consequently, this leads to a change in seed photon flux and, in turn, observed 6.7 GHz brightness. This model produces an asymmetric flare profile with a rapid brightness increase and a longer decrease phase. Nevertheless, it requires the existence of an ultra-compact HII region. In the case of both sources presented in the paper, CWB is not the likely cause. G45.804−0.356 shows no continuum emission typical to HII regions. Although G49.043−1.079 has weak continuum emission, the flare profiles show mostly symmetrical Gaussian profiles, which this model does not readily produce.

Numerical simulations of massive protostars undergoing substantial accretion have revealed that they could become pulsationally unstable (Inayoshi et al. 2013). The star's luminosity varies periodically, increasing the local dust temperature and leading to a rise in the pumping efficiency of the maser and its brightness. The relation between the pulsation period and the protostellar luminosity is given by the relation $\log(L) = 4.62 + 0.98\log(P/100 \text{ days})$, where L is luminosity in $L_\odot$ and P is the period. Since G45.804−0.356 shows no detectable variability in IR, we can rule out this process. In the case of G49.043−1.079, observed IR flares might suggest periodic pulsations. For a period of 469 days, the predicted luminosity should be $\sim 2 \times 10^5\ L_\odot$, but the luminosity estimated from observations is $\sim 2 \times 10^3\ L_\odot$ (Urquhart et al. 2018). The difference of two orders of magnitude suggests that a periodic pulsation scenario is unlikely.

According to the rotating spiral shock model proposed by Parfenov & Sobolev (2014), matter accreting onto the binary system does so through hot, shocked, spiral structures, which are seen in many simulations (Artymowicz & Lubow 1996; Muñoz & Lai 2016). As an effect of the rotation, these shocks would periodically heat up portions of the accretion disc, increasing the pumping efficiency. The geometry of the system strongly constrains this model as it requires an edge-on configuration. Additionally, the model requires neither the presence of detectable continuum emission nor strong variability in IR brightness. It appears as the most probable cause for G45.804−0.356. However, the lack of a complete, high angular resolution map of maser emission prevents us from verifying this hypothesis. In the case of G49.043−1.079, the edge-on morphology could allow this mechanism, but it is unclear if the spiral shocks could produce an observed IR flare.

Interaction between a binary system and accreting matter does not only lead to the creation of spiral structures in the circumbinary disc: in some cases, it can also strongly modulate accretion (Muñoz & Lai 2016). We have argued that this process is responsible for the periodic variability of G107.298+5.639 and G59.633−0.192 (Szymczak et al. 2016; Olech et al. 2019). Well-separated features of G49.043−1.079 show methanol and IR flare profiles very similar to those of G59.633−0.192 mentioned above; the two sources most likely share the same driving mechanism.

A recent study of three periodic masers, G9.62+0.19E, G22.357+0.066, and G25.411+0.105, suggests that source geometry and orientation in the plane of the sky might also be an important factor influencing observed flare profiles (Morgan et al. 2021), but more research is needed. High-quality data limited to single-dish observations are presented for the sources analysed in this paper. However, interferometric spectral and continuum observations with milliarcsecond resolution are needed to fully understand these objects.

4.3. Other characteristics

The line of sight effect cannot easily explain the large time lags between features of G49.043−1.079. A time lag of 67.7 days would require a distance of 12 000 au, which is an order of magnitude higher than the linear size of the emission in the sky plane and a typical size for methanol maser sources. A similar

phenomenon was observed in three other periodic sources, G25.411+0.105 (Szymczak et al. 2015), G30.400−0.296 (Olech et al. 2019), and G331.13−0.24 (Goedhart et al. 2014), and is not yet understood. Large inhomogeneities in the local environment and differences in dust and gas heating times might be the causes. Other noteworthy phenomena visible in the source are rapid jumps in the intensity (shorter than 2 weeks), which are most pronounced during flare maxima at 38.41 and 39.25 km s^{-1}. A similar phenomenon was first detected in the quasi-periodic source G33.641−0.228 (Fujisawa et al. 2014), but more frequent observations are needed to verify its nature.

5. Summary

We have presented the analysis of two previously unidentified periodic 6.7 GHz methanol masers, G45.804−0.356 and G49.043−1.079, which respectively have periods of 416.9 and 469.3 days. Infrared variability in source G49.043−1.079 shows a periodic flare that is simultaneous with methanol maser changes. Measured phase lags between features in this source are as high as 68 days, which cannot be attributed to line of sight effects. No clear explanation can be inferred for the cyclical variability in G45.804−0.356 with the available data. For G49.043−1.079, periodicity is most likely caused by a modulated accretion leading to an increased pumping efficiency of methanol masers. Both sources should be targeted in future Very Long Baseline Interferometry observations in order to examine and verify our conclusions.

Acknowledgements. M.O. thanks the Ministry of Education and Science of the Republic of Poland for support and granting funds for the Polish contribution to the International LOFAR Telescope (arrangement no. 2021/WK/02) and for maintenance of the LOFAR PL-612 Baldy (MSHE decision no. 59/E-383/SPUB/SP/2019.1). The 32 m radio telescope is operated by the Institute Astronomy, Nicolaus Copernicus University and supported by the Polish Ministry of Science and Higher Education SpUB grant. We thank the staff and students for assistance with the observations. This research made use of Astropy (`http://www.astropy.org`), a community-developed core Python package for Astronomy. This publication makes use of data products from the Near-Earth Object Wide-field Infrared Survey Explorer (NEOWISE), which is a joint project of the Jet Propulsion Laboratory/California Institute of Technology and the University of Arizona. NEOWISE is funded by the National Aeronautics and Space Administration. This research has made use of NASA's Astrophysics Data System Bibliographic Services.

References

Araya, E. D., Hofner, P., Goss, W. M., et al. 2010, ApJ, 717, L133
Artymowicz, P., & Lubow, S. H. 1996, ApJ, 467, L77
Astropy Collaboration (Robitaille, T. P., et al.) 2013, A&A, 558, A33
Astropy Collaboration (Price-Whelan, A. M., et al.) 2018, AJ, 156, 123
Bartkiewicz, A., Szymczak, M., & van Langevelde, H. J. 2016, A&A, 587, A104
Breen, S. L., Fuller, G. A., Caswell, J. L., et al. 2015, MNRAS, 450, 4109
Burns, R. A., Sugiyama, K., Hirota, T., et al. 2020, Nat. Astron., 4, 506
Cragg, D. M., Sobolev, A. M., & Godfrey, P. D. 2005, MNRAS, 360, 533
Cutri, R. M., Mainzer, A., Conrow, T., et al. 2015, Explanatory Supplement to the NEOWISE Data Release Products, Tech. rep.
Edelson, R. A., & Krolik, J. H. 1988, ApJ, 333, 646
Ellingsen, S. P. 2006, ApJ, 638, 241
Fujisawa, K., Aoki, N., Nagadomi, Y., et al. 2014, PASJ, 66, 109
Goddi, C., Moscadelli, L., & Sanna, A. 2011, A&A, 535, A8
Goedhart, S., Gaylard, M. J., & van der Walt, D. J. 2003, MNRAS, 339, L33
Goedhart, S., Gaylard, M. J., & van der Walt, D. J. 2004, MNRAS, 355, 553
Goedhart, S., Maswanganye, J. P., Gaylard, M. J., & van der Walt, D. J. 2014, MNRAS, 437, 1808
Hu, B., Menten, K. M., Wu, Y., et al. 2016, ApJ, 833, 18
Hunter, T. R., Brogan, C. L., MacLeod, G. C., et al. 2018, ApJ, 854, 170
Inayoshi, K., Sugiyama, K., Hosokawa, T., Motogi, K., & Tanaka, K. E. I. 2013, ApJ, 769, L20
Mainzer, A., Bauer, J., Grav, T., et al. 2011, ApJ, 731, 53
Mainzer, A., Bauer, J., Cutri, R. M., et al. 2014, ApJ, 792, 30
Maswanganye, J. P., Gaylard, M. J., Goedhart, S., van der Walt, D. J., & Booth, R. S. 2015, MNRAS, 446, 2730
Menten, K. M. 1991, ApJ, 380, L75
Morgan, J., van der Walt, D. J., Chibueze, J. O., & Zhang, Q. 2021, MNRAS, 507, 1138
Moscadelli, L., Sanna, A., Goddi, C., et al. 2017, A&A, 600, A8
Muñoz, D. J., & Lai, D. 2016, ApJ, 827, 43
Olech, M., Szymczak, M., Wolak, P., Sarniak, R., & Bartkiewicz, A. 2019, MNRAS, 486, 1236
Olech, M., Szymczak, M., Wolak, P., Gérard, E., & Bartkiewicz, A. 2020, A&A, 634, A41
Pandian, J. D., Goldsmith, P. F., & Deshpande, A. A. 2007, ApJ, 656, 255
Parfenov, S. Y., & Sobolev, A. M. 2014, MNRAS, 444, 620
Reid, M. J., Menten, K. M., Brunthaler, A., et al. 2019, ApJ, 885, 131
Scargle, J. D. 1982, ApJ, 263, 835
Schwarzenberg-Czerny, A. 1989, MNRAS, 241, 153
Sugiyama, K., Nagase, K., Yonekura, Y., et al. 2017, PASJ, 69, 59
Sugiyama, K., Yonekura, Y., Motogi, K., et al. 2018, in Astrophysical Masers: Unlocking the Mysteries of the Universe, 336, eds. A. Tarchi, M. J. Reid, & P. Castangia, 45
Szymczak, M., Wolak, P., Bartkiewicz, A., & van Langevelde, H. J. 2011, A&A, 531, A3
Szymczak, M., Wolak, P., Bartkiewicz, A., & Borkowski, K. M. 2012, Astron. Nachr., 333, 634
Szymczak, M., Wolak, P., & Bartkiewicz, A. 2015, MNRAS, 448, 2284
Szymczak, M., Olech, M., Wolak, P., Bartkiewicz, A., & Gawroński, M. 2016, MNRAS, 459, L56
Szymczak, M., Olech, M., Sarniak, R., Wolak, P., & Bartkiewicz, A. 2018, MNRAS, 474, 219
Urquhart, J. S., Moore, T. J. T., Menten, K. M., et al. 2015, MNRAS, 446, 3461
Urquhart, J. S., König, C., Giannetti, A., et al. 2018, MNRAS, 473, 1059
van der Walt, D. J. 2011, AJ, 141, 152
van der Walt, D. J., Goedhart, S., & Gaylard, M. J. 2009, MNRAS, 398, 961
van der Walt, D. J., Maswanganye, J. P., Etoka, S., Goedhart, S., & van den Heever, S. P. 2016, A&A, 588, A47

Appendix A: Supplementary figures

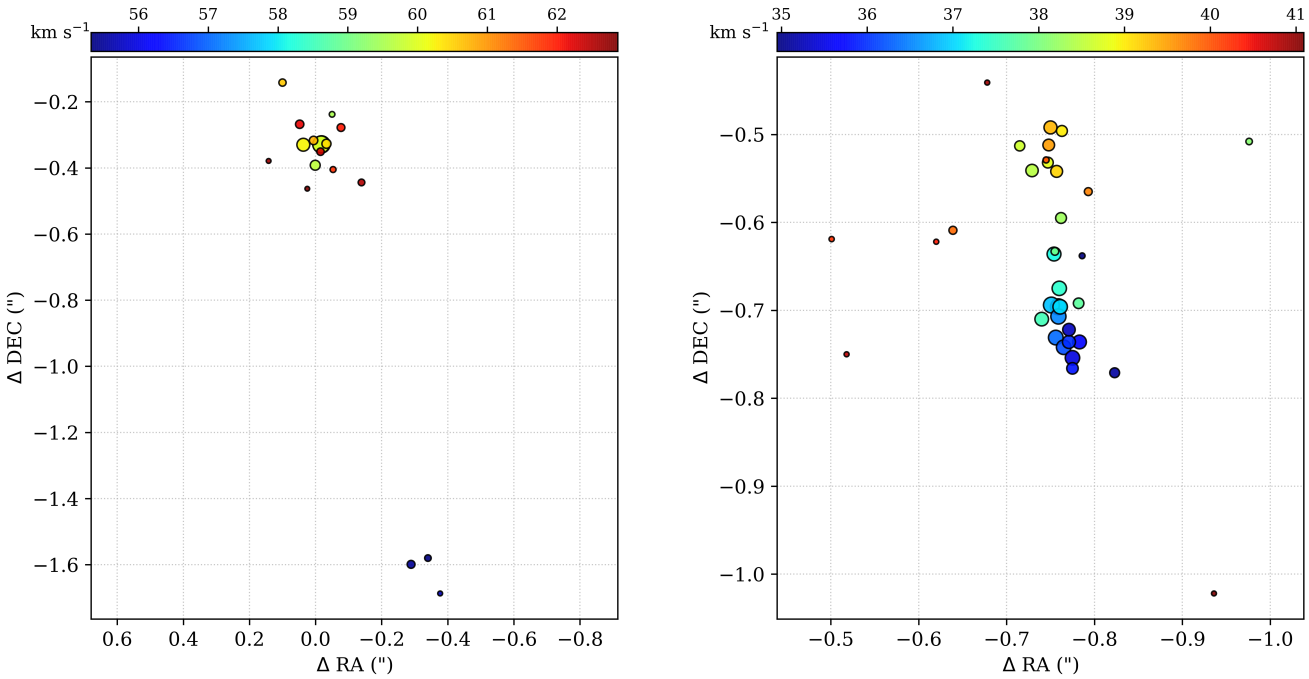

Fig. A.1. VLA map of 6.7 GHz methanol maser emission in the sources G45.804−0.356 (left) and G49.043−1.079 (right) taken from Hu et al. (2016). The size of the circles is scaled logarithmically with measured brightness, and their colours represent velocity.